Simulation & Calibration of the ALICE TPC including innovative Space Charge Calculations

Stefan Rossegger

CERN-THESIS-2009-124
30/10/2009

“There is no use trying,” said Alice;
“one can’t believe impossible things.”
“I dare say you haven’t had much practice,”
said the Queen. “When I was your age,
I always did it for half an hour a day.
Why, sometimes I’ve believed as many as six
impossible things before breakfast.”

(Lewis Carroll, Alice’s Adventures in Wonderland)

DISSERTATION

Simulation and Calibration of the ALICE Time-Projection Chamber including innovative Space Charge Calculations

to attain the academic degree of
Doctor rerum naturalium

Graz University of Technology
Institute of Theoretical and
Computational Physics,
A-8010 Graz, Austria

Conseil Européen pour la
Recherche Nucléaire
CH-1211 Genéve, Switzerland

submitted by

Stefan Rossegger

(September 2009)

Advisor: Em.Univ.-Prof. Dr.phil. Bernhard Schnizer (TU Graz / ITP)
Co-Advisors: Dr. Werner Riegler (CERN / PH-AIO)
Dr. Latchezar Betev (CERN / PH-AIP)

DISSERTATION

Simulation und Kalibration der ALICE Zeit-Projektions-Kammer inklusive neuartiger Raumladungs-Berechnungen

zur Erlangung des akademischen Grades
Doktor der Naturwissenschaften

Technische Universität Graz
Institut für Theoretische Physik -
Computational Physics
A-8010 Graz, Österreich

Europäische Organisation
für Kernforschung
CH-1211 Genf, Schweiz

vorgelegt von

Stefan Rossegger

(September 2009)

Betreuer: Em.Univ.-Prof. Dr.phil. Bernhard Schnizer (TU Graz / ITP)
Betreuer vor Ort: Dr. Werner Riegler (CERN / PH-AIO)
Dr. Latchezar Betev (CERN / PH-AIP)

Diese Arbeit wurde unterstützt vom
Österreichischen Bundesministerium für Wissenschaft und Forschung
und ist in englischer Sprache verfasst

Abstract

ALICE is one of the four main particle detectors located around the *LHC* accelerator at *CERN*. It is particularly designed to study the physics of the quark-gluon plasma by means of nucleus–nucleus collisions at center-of-mass energies up to 5.5 TeV per nucleon pair. A *Time-Projection Chamber* (TPC) was chosen to be its central-sub-detector due to its low mass properties and its capabilities to provide a robust and accurate Particle Identification even within ultra-high multiplicity environments (up to 8000 tracks per unit of η). To achieve the required physics performance, the space point resolution of the TPC must be in the order of 200 μm. Due to its gigantic size of 5 m in diameter and 5 m in length, corrections for static as well as dynamic effects are indispensable in order to accomplish the design goal.

The research presented covers all major issues relevant for the final calibration and therefore the enhancement of the *TPC performance* in terms of *resolution*. The main focus was to distinguish between the different effects which disturb the electron trajectory within the drift volume by means of quantifying the magnitude of their influences. The effects were parametrized in terms of physical parameters, as opposed to a multivariate fit, in order to minimize the residuals of the cluster positions. The different chapters of the present research work cover *static imperfections*, like magnetic and electric field inhomogeneities due to mechanical imperfections, as well as *dynamic variations* of the drift properties due to pressure, temperature and gas composition variations which manifest themselves as gas density fluctuations. Furthermore, additional challenges were treated which will occur in future *high multiplicity* nucleus-nucleus collisions. These are the improvement of the two-track resolution as well as the quantification of additional *dynamic field deviations* due to space charges.

Various simulation techniques were used to qualify and quantify the field imperfections due to mechanical deficiencies. Besides the localization and calibration of the field imperfections, the simulations led to optimized voltage settings which minimize the residuals. The different drift velocity (v_d) dependencies were parametrized to allow a quick estimation of the dynamic v_d variations as a function of the measured ambient conditions. Besides that, the programmable signal shaping algorithm within the Front-End electronics was revised. This is expected to improve the two-track resolution in high multiplicity events.

Moreover, novel *analytical solutions* were derived to allow a fast and precise prediction of additional *dynamic field deviations* due to ionic-charge pile up within the TPC gas volume. This analytic approach finally permits accurate simulations of additional systematic shifts along the electron trajectory due to any *three dimensional space charge distribution* within the TPC. This innovative method is an essential part of the calibration algorithms which are being developed for the future Pb-Pb collisions at LHC.

Kurzfassung

ALICE ist einer der vier großen Teilchendetektoren in *CERN*, welche am LHC Beschleuniger situiert sind. ALICE wurde entwickelt um, anhand von Schwerionenkollisionen mit einer Energie von bis zu 5.5 TeV, die Physik des Quark-Gluon Plasmas zu untersuchen. Als zentraler Detektor fungiert eine *Zeit-Projektions-Kammer* (eng. TPC), welche präzise und zugleich robuste Teilchen-Identifikation innerhalb von Umgebungen mit extrem hohen Spurendichten ermöglicht. Um die geforderte Auflösung von besser als 200 μm zu erzielen, ist die Berücksichtigung von statischen als auch dynamischen Effekten und Verzerrungen zwingend nötig. Wegen der noch nie da gewesenen Ausmaße der TPC (5 m Durchmesser und 5 m Länge) ist die Implementierung der daraus resultierenden Korrekturen unabdingbar.

Die vorliegende Arbeit berücksichtigt alle Haupteinflussfaktoren und Effekte, welche für die finale Kalibration und somit für die Verbesserung der *TPC Ortsauflösung* relevant sind. Der Fokus richtet sich auf die Unterscheidung und Quantifizierung der verschiedenen Effekte, welche die Elektronenbahn und -drift innerhalb der TPC beeinflussen. Um die Abweichungen zu minimieren wurden Parametrisierungen entwickelt, welche die Effekte, im Gegensatz zu Multivariation Fits, gesondert und mit möglichst physikalischen Parametern beschreiben. Die verschiedenen Kapitel behandeln *statische Unvollkommenheiten*, wie z.B. magnetische und elektrische Feldinhomogenitäten aufgrund mechanischer Beschränkungen, sowie *dynamische Variationen* der Drifteigenschaften aufgrund von Druck- Temperatur- und Gaskompositionsschwankungen, welche sich als Gasdichtefluktuationen manifestieren. Weiters wurden die durch Nukleus-Nukleus Kollisionen entstehenden zusätzlichen Herausforderungen, an die Zwei-Spur Auflösung als auch an die Korrektur von zusätzlichen dynamischen Feldfluktuationen aufgrund summierter positiver Raumladungen, in Angriff genommen.

Um die Feldinhomogenitäten aufgrund mechanischer Unzulänglichkeiten zu lokalisieren und zu quantifizieren wurden unterschiedlichste Simulationstechniken verwendet und erprobt. Dies führte zu optimierten Spannungeinstellungen, welche systematische Fehler aufgrund statischer Unvollkommenheiten minimieren. Zudem wurde eine Parametrisierung entwickelt, welche die Driftgeschwindigkeit in Abängigkeit ihrer einflussnehmenden Größen beschreibt. Dies erlaubt eine schnelle Abschätzung der Driftgeschwindigkeitsänderungen mittels gemessener Umgebungsparameter. Zur Verbesserung der Zwei-Spur Unterscheidung wurde der programmierbare Algorithmus der Signalformung innerhalb der Ausleseelektronik überarbeitet.

Darüber hinaus wurden *neuartige analytische Lösungen* hergeleitet, welche eine schnelle und präzise Berechnung von *dynamischen Feldvariationen*, aufgrund angehäufter ionischer Raumladungen, ermöglichen. Dieser analytische Ansatz erlaubt erstmals die präzise Simulation von zusätzlichen systematischen Abweichungen der Elektronenbahn aufgrund beliebiger *3D-Raumladungsverteilungen* innerhalb des Driftvolumes einer TPC. Diese innovative Methode ist essentiell und richtungsweisend für die Erweiterung der Kalibrationsalgorithmen, welche für zukünftige Schwerionenkollisionen entwickelt werden müssen.

Acknowledgments

First of all I want to thank my advisor, Prof. Bernhard Schnizer, for his fundamental suggestions, ideas and his incitement for the beauty of analytical methods. The research presented especially in the last chapter could not have been performed without his encyclopedic knowledge of Green's functions and his infinite enthusiasm when following rather unconventional ideas. Much obliged!

Thanks to my advisor at CERN, Werner Riegler, for suggesting the topic, directing my attention to the field of detector physics and for giving me the opportunity to perform my research at CERN. Many thanks for your guidance, your support and your advices along the way.

My gratitude to all the people in the TPC as well as the Offline group. It was a pleasure to work with you. Special thanks to Latchezar Betev, Luciano Musa and Federico Carminati for giving me the opportunity to work in such a highly motivating environment, not to forget their instant support in every kind of issue. Moreover, thanks to Yiota Foka for the helpful and critical proofreading of the manuscript.

Special thanks to my friends and companions, situated in the region of Geneva, in Austria or scattered to the four winds. To name you all would simply go beyond the scope. I am grateful for these friendships!

Thanks above all to Sabine! No words could describe on how much you supported me. We both suffered our geographical disunion and looked forward to the little time we could spend together during this last years. You simply complete me!

Besonderer Dank gilt meinen Eltern, Franz und Ottilie Rossegger, für ihren ständigen Beistand als auch für ihre sofortige Hilfe in jeglicher Hinsicht. Ohne eure Unterstützung wäre mein Studium sowie die Entscheidung, ein Doktorat anzustreben, wohl niemals möglich gewesen und wahr geworden. Wieviel ich euch schulde, kann wohl nicht mit Worten beschrieben werden.

Diese Arbeit sei EUCH gewidmet!

Stefan Rossegger
Graz, Austria, September 2009

Contents

Abstract **vii**

Kurzfassung **ix**

Acknowledgments **xi**

1 Introduction **1**

1.1 Quantum Chromodynamics and the Quark-Gluon Plasma 2
1.2 ALICE - A Large Ion Collider Experiment 4
1.2.1 Detectors 4
1.2.2 Performance 6
1.3 The ALICE Time-Projection Chamber 6
1.3.1 Working principle 7
1.3.2 Performance requirements and technical design 9
1.3.3 Calibration issues 12
1.4 Methodology of basic calibrations techniques 12
1.4.1 Laser calibration 13
1.4.2 Krypton calibration 13

2 Distortions by static imperfections **15**

2.1 Gas density fluctuations 16
2.1.1 Gas properties of a (Ne-CO_2-N_2) mixture 17
2.1.2 Variations due to impurities 19
2.1.3 Temperature sensitivity 21
2.2 B field uniformity 22
2.2.1 Lorenz angle calculations 23
2.2.2 E×B effect 25
2.3 E field uniformity 26
2.3.1 Field cage strips and read-out chambers 27
2.3.2 Optimized voltage settings 29
2.3.3 Simulation of misalignment and distortions 30

3 Signal shape and read-out optimization 37
3.1 Ion-tail characterization and shape variations 39
3.2 Signal shape simulations 40
3.2.1 Signal shape dependencies 42
3.2.2 Determination of the avalanche spread 44
3.3 ALTRO chip - raw data optimization 45
3.3.1 Tail-Cancellation Filter 46
3.3.2 Analysis and quality assurance 52

4 Dynamic effects and distortions 59
4.1 Parametrized drift velocity dependencies 59
4.2 Simulated temperature distribution within the gas volume 61
4.2.1 CFD model description 63
4.2.2 Simulated case studies 64
4.3 Temperature and pressure variations 70
4.3.1 Drift-velocity: matching ITS-TPC tracks 73
4.4 High multiplicity environments 77

5 Analytical approach to space charge effects 79
5.1 Point charge in a coaxial cavity 80
5.1.1 Green's function represented by ordinary Bessel functions 81
5.1.2 Green's function represented through modified Bessel functions . . . 84
5.1.3 Green's function represented through modified Bessel functions of imaginary order and real argument 85
5.1.4 Convergence improvement close to the point charge 89
5.1.5 Results and comparison 91
5.2 Electrical field due to an arbitrary space charge distribution 94
5.2.1 Electric field due to a point charge 94
5.2.2 Electric field due to a constant charge within a POC volume 96
5.2.3 Fast evaluation: discretization of the space charge distribution . . . 98
5.3 Expected deviations in high multiplicity events 100
5.3.1 Simulated space charge distributions 100
5.3.2 Expected distortions 103

6 Comprehensive summary 107

A Green's functions for bisected coaxial cavity 111

Bibliography 123

Chapter 1

Introduction

The European Organization for Nuclear Research (CERN - Conseil Européen pour la Recherche Nucléaire) has recently finished the installation of the Large Hadron Collider (LHC). This circular collider with a beam line of 27 km circumference is scheduled to be operational in the fall of 2009. Ultimately, it will collide proton beams at a center-of-mass energy of $\sqrt{s} = 14$ TeV. One of the aims among precision measurements of Standard Model (SM) parameters, the discovery of the Higgs bosons and the general search of new physics is, to obtain a deeper understanding of strongly interacting matter and the Quark-Gluon Plasma (QGP) (see section 1.1).

ALICE (A Large Ion Collider Experiment) is one of the four main particle detectors located around the LHC accelerator (see section 1.2). It is a general-purpose heavy-ion detector designed to study the physics of quark-gluon plasma by means of nucleus–nucleus collisions at center-of-mass energies up to 5.5 TeV per nucleon pair. Due to the high multiplicity in Pb–Pb collisions an instant and accurate Particle Identification, by means of dE/dx and momentum measurements, is only possible by using a gaseous tracking device, namely a Time-Projection Chamber (TPC), as the central sub-detector (see section 1.3).

The ALICE TPC will be used to track 20.000 charged particles produced in a single Pb–Pb collision. In order to achieve the required position resolution of 200 μm, corrections for static and dynamic variations of the drift properties as well as the drift corrections for field imperfections must be applied.

The aim of the present doctoral thesis is to disentangle the different effects, which disturb the drift of the electrons, and to quantify the magnitude of their influence in terms of space point distortions. The following sections give a short introduction on the scientific goals of ALICE as well as a summary on the construction and working principles of its main tracking device, the TPC.

Chapter 2 contains basic considerations regarding static imperfections of the TPC and how they influence the basic performance. Basic properties of the used drift gas are discussed as are the influences of gas composition variations and impurities in terms of drift velocity and diffusion coefficients. Furthermore, static imperfections due to the applied fields are reviewed. Resulting space point distortions due to magnetic field impurities and electric field (drift field) imperfections due to mechanical restrictions are discussed and quantified.

Chapter 3 deals especially with the signal shapes within the TPC read-out system. It describes how their shape can be simulated and based on that, how the signal can be reshaped in order to improve the performance for high multiplicity events such as heavy-ion collisions.

Dynamic (short and long term) variations of the ambient conditions around the TPC and how they influence mainly the drift velocity and therefore the z resolution are discussed in chapter 4.

In order to improve simulation and calibration capabilities of TPC detectors for heavy-ion collisions, an analytical approach for space charge calculations is introduced in chapter 5. In there, a completely novel method to calculate drift field variations due to non-negligible space charge accumulations within the TPC drift volume is presented. Furthermore, space point distortions due to expected space charge configurations are discussed and compared to the reviewed distortions due to magnetic field imperfections.

Final conclusions are presented in the last chapter of the present thesis. It contains a summary of the most important effects and the magnitude of their influence on the space point resolution and therefore the performance capability of the TPC detector. Furthermore, a brief outlook on future calibration and commissioning projects is given in order to improve the tracking capabilities of the TPC for high multiplicity events in Pb–Pb collisions.

In summary, this thesis covers all major issues relevant to the intended improvement of the space point resolution as well as the minimization of systematic errors as caused by imperfections of the ALICE TPC.

1.1 Quantum Chromodynamics and the Quark-Gluon Plasma

This section provides a brief overview on today's open questions regarding the origin of the universe. No attempt was made to give a detailed insight into the frontier of modern physics research, or Quantum Chromodynamics (QCD) respectively. However, excellent books were written to which I have the honor to refer. For the non-expert, a basic overview on the general motive to study High Energy Physics (HEP) can be found in [1]. The reader who wants to deepen his understanding in Quantum Field Theory (QFT) as well as QCD may be referred to [2] and [3].

HEP has established and validated a detailed, though still incomplete, theory of elementary particles and their fundamental interactions, called the Standard Model (SM). Quantum Chromo-Dynamics (QCD) deals with one of the four fundamental forces in nature, the strong interaction. It describes the interactions between quarks and their force carriers, the gluons. This theory, which was developed in the 1970s, describes how quarks and gluons (or partons) bind together to form the class of particles called hadrons, of which the proton and neutron are the most familiar examples.

It is believed that in the early universe, about 10 μs after the bing-bang, today's ordinary hadronic matter existed under extreme conditions of energy density and temperature in the form of a deconfined state of quarks and gluons, namely a Quark-Gluon Plasma (QGP) [5]. The main objectives of heavy-ion physics is to study the properties of the QGP and to explore the QCD phase transition within the phase diagram of strongly interacting matter. Figure 1.1 holds a systematic overview of the basic understanding of

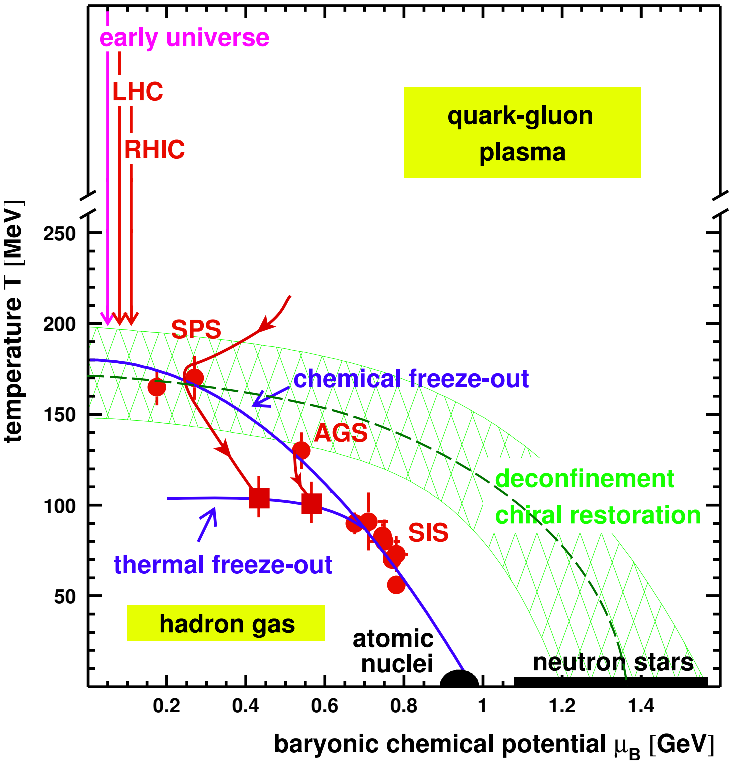

Figure 1.1: Sketch of the QCD phase diagram. Temperature T versus the baryon chemical potential μ_{B} associated with net baryon density ρ_{B}. The cross-hatched region indicates the expected phase transition and its theoretical uncertainty, with the dashed line representing its most likely location [4].

the QCD phase diagram as well as previous experimental results.

The interest in ultra relativistic high-energy collisions is driven by their capability to produce these states of compressed baryonic matter at densities several times higher than the ground state density by colliding the heaviest nuclei available (lead or gold). By colliding heavy ions at very high energies one would expect to reach and exceed the critical energy density (T_c ∼170 MeV), where the system is predicted (by Lattice QCD) to undergo it's phase transition to form the QGP similar to the state shortly after the big bang.

The Alternating Gradient Synchrotron (AGS) at Brookhaven National Laboratory as well as the Super Proton Synchrotron (SPS) at CERN were the pioneering experimental facilities in the field of ultra-relativistic heavy-ion collisions. The center-of-mass energies covered by these fixed target experiments was 2 GeV to 17 GeV per nucleon pair. The first colliding heavy-ion beams (gold nuclei) were made by the Relativistic Heavy-Ion Collider (RHIC) in Brookhaven which delivered center-of-mass energies up to 200 GeV.

It is scheduled that in the fall of 2010, the LHC at CERN will deliver the first heavy-ion collisions with an energy almost 30 times higher than anything seen so far. Global features of our universe, like baryon asymmetry or the large scale structure (galaxy distribution), are believed to be better understood if characteristic properties of these phase transitions within the QCD theory are explored and the structure of the QCD phase diagram is further exploited.

1.2 ALICE - A Large Ion Collider Experiment

This section contains a basic overview of the ALICE experiment, the physics motivation, the physics performance as well as a short description of the sub-detector system. Further details and additional informations can be found in [6] and [7].

ALICE is designed to study heavy-ion (Pb–Pb) collisions, therefore, it is optimised to provide an accurate Particle IDentification (PID) together with a full phase-space coverage. In addition, due to the accurate secoundary vertex reconstruction it poses a multi-purpose system. ALICE has been built by a collaboration including currently over 1000 physicists and engineers from 105 institutes distributed over 30 countries. Its overall dimensions are 16×16×26 m^3 with a total weight of approximately 10.000t. In contrast to the other experiments at the LHC (ATLAS [8], CMS [9] and LHCb [10]) its focus lies on revealing the role of chiral symmetry in the generation of mass in composite particles (hadrons). An additional aim is to gain insight into the physics of parton densities close to phase-space saturation, and their collective dynamic evolution towards hadronization (confinement) in a dense nuclear environment. Furthermore, the ALICE Collaboration will study collisions of lower-mass ions, as a means of varying the energy density, and protons, which primarily provide reference data for the nucleus–nucleus collisions.

As the energy of the colliding protons or nuclei is increasing. one of the most fundamental observables, the particle multiplicity, is also increasing. At LHC, a multiplicity of 1.500 to 8.000 charged particles per unit of rapidity were predicted for Pb–Pb collisions at 5.5 TeV [11]. As this quantity will only be known after inspection of the first events, the detectors have to be built according to the highest predicted multiplicity. The large uncertainties in the multiplicity are due to the fact that basic parameters of QCD are not known. Therefore, the many models (with different theoretical bases) deviate in their predicted multiplicities [6, 12].

The complete ALICE detector system was designed to handle the maximum predicted particle multiplicity of $dN/d\eta \approx$8.000 (for Pb–Pb collisions at a center-of-mass energy of 5.5 TeV). The compilation of sub-detectors has been specifically designed to maximize the momentum coverage from $\approx$ 100 MeV/c, the lowest values relevant for thermodynamical studies, up to $\approx$ 100 GeV/c, the transverse momentum of the leading particles of jets with transverse energy well over 100 GeV. The measurement of numerous precision points over a long measured track length in a moderate magnetic field and with minimal material allows to satisfy both requirements.

The event rate of Pb–Pb collisions, given the maximum luminosity of $1.0 \times 10^{27} \mathrm{cm}^{-2}\mathrm{s}^{-1}$ and an inelastic cross-section of 8 b, will be 8.000 minimum-bias collisions per second. Only some 5 % of these events are expected to correspond to the most central collisions. This low interaction rate allows the use of slow but high-granularity detectors, like the Time-Projection Chamber and the Silicon-Drift Detectors. The ALICE rapidity acceptance has been chosen to be large enough to allow the study of particle production and chemical composition at mid-rapidity via particle ratios.

1.2.1 Detectors

A schematic layout of the ALICE detector setup is given in figure 1.2. A systematic description of its detectors can be found in [13]. Besides that, the different detector systems

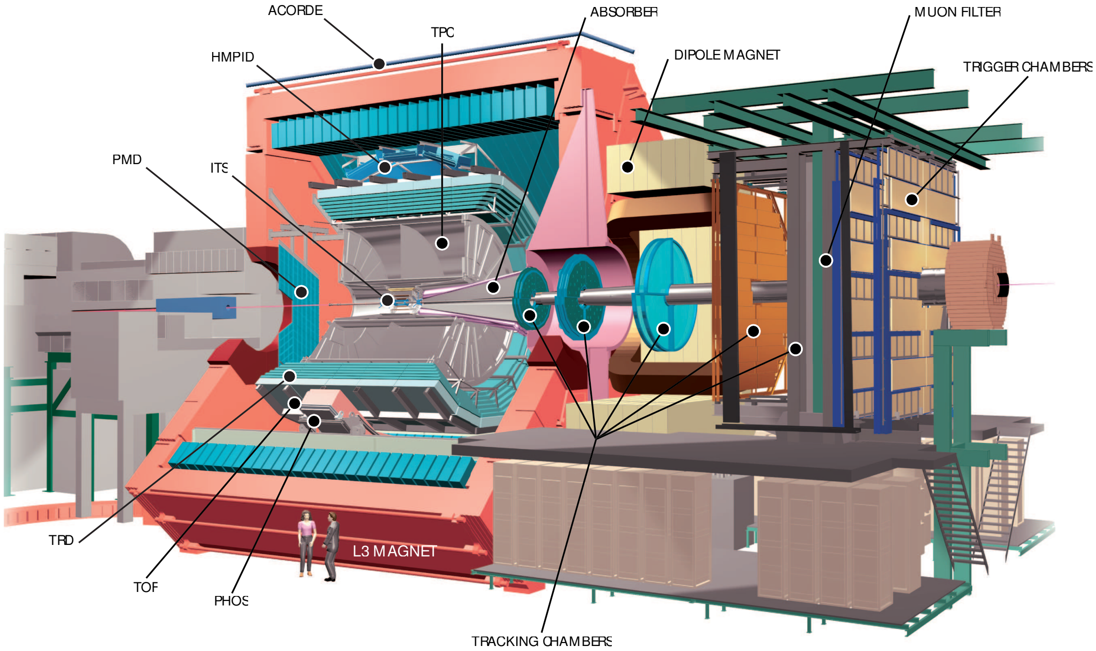

Figure 1.2: Layout of the ALICE detector. The HMPID detector is shown in the 12 o'clock position (instead of the actual 2 o'clock position) for the sake of visibility [6].

are described in great detail in a number of Technical Design Reports (see bibliography in [13]). The following paragraphs represent a brief overview of the reference just mentioned.

The experiment consists of a central detector system, covering a mid-rapidity range of $|\eta| \leq 0.9$ over the full azimuth, and several forward systems for extension of the experiment to large rapidity.

The central system is installed inside a large solenoidal magnet (L3) which generates a magnetic field of ~ 0.5 T. The central barrel contains an Inner-Tracking System (ITS) of six planes of high-resolution silicon pixel (SPD), drift (SDD) and strip (SSD) detectors and a cylindrical Time-Projection Chamber (TPC). Tracking is performed by means of combining the information from the TPC, the main tracking detector, with the information coming from the ITS, which provides high-resolution tracking and precise vertex reconstruction.

Three particle identification arrays consisting of Time Of Flight (TOF), Ring-Imaging Cerenkov (HMPID) and a Transition-Radiation Detector (TRD) are situated within the L3 magnet. The TOF barrel provides the identification for the bulk of the intermediate-momentum particles. The HMPID (High Momentum Particle Identification Detector), extends the particle identification to higher momenta. Additional particle identification is provided by the central tracking detectors (TPC and ITS) through the measurement of the specific energy loss which provides separation of low momenta and some identification capability in the relativistic rise region. This means, short-lived particles are identified by exploiting the tracking and vertex measurements of the experiment. Electrons are identified using the TRD information. Moreover, two electromagnetic calorimeters are installed. Photons are measured in the very-high-granularity crystal calorimeter (PHOton Spectrometer — PHOS) whereas the EMCal is used to improve the jet energy resolution. All detectors except HMPID, PHOS and EMCal cover the full azimuth.

The forward muon spectrometer was built for enlarging the region of rapidity measurements. It consists of a complex arrangement of absorbers, a large dipole magnet and fourteen planes of tracking and triggering chambers. Several smaller detectors (ZDC, PMD, FMD, T0, V0) for global event characterization and triggering are located at small angles.

1.2.2 Performance

A comprehensive review of the expected physics performance can be found in [6] and [7]. Anyhow, one of the most challenging tasks for ALICE is that of track finding in an unprecedented particle multiplicity density environment. The primary vertex determination is performed by the SPD and depends on the track multiplicity. For heavy-ion collisions a vertex-position resolution on the level of 10 μm is expected. For the average pp event we expect 150 μm. The track reconstruction is performed by the Kalman filter [14]. For very high densities ($\mathrm{d}N_{ch}/\mathrm{d}\eta = 6000$, well above the current theoretical predictions), the efficiency for tracks with a transverse momentum within 200-300 MeV/c is about 90 %, and increases to values above 95 % at higher momenta. At the same time, the fake-track probability is below 10 % for lower momenta and decreases below 1 % for high momenta [13, p.202].

Several detectors participate in the particle identification, each with a different momentum dependent performance. The particle identification, and therefore the track separation power, depends heavily on the dE/dx resolution of e.g. the TPC which is in the range of 5.5 % for pp events and 6.5 % for central Pb–Pb collisions. In the lower momentum range we have exellent separations in the $1/\beta^2$ range (below the particle masses). Increasing the momentum to the values where the Bethe-Bloch curves for two particles cross, naturally minimizes the chances of correct particle identification. At still higher momenta, the particle separation efficiency increases again thanks to the relativistic rise of the dE/dx in the TPC gas. Momentum dependent separation powers can be found in [13, p.209].

Muons are detected in the forward spectrometer in the pseudo-rapidity range of $-4.0 < \eta < -2.5$. A tracking efficiency above 95 % is obtained, even at a level of background twice than that expected in central Pb–Pb collisions.

Each single sub-detector was especially designed to fulfill its specific part of the above mentioned global performance requirements. Besides the sophisticated planning and construction of each sub-detector, their calibration is an essential part and an additional challenge in order to reach the required performance.

1.3 The ALICE Time-Projection Chamber

A Time-Projection Chamber (TPC) provides a 3D picture of the ionization process due to high energy particles traversing its gas volume. It is built with a fast and purely electronic read-out. This 3D-imaging capability defines the usefulness as a tracking device within a high track-density environment as it is the case for heavy-ion experiments. It provides tracking capability of charged particles over a large volume without a big amount of material. Furthermore, the particles produced in a collision can be identified through their ionization energy loss (dE/dx) which is one of the major observables of a TPC. For that reason, it was chosen to be the main tracking device of the ALICE experiment.

Historically, the usage of a large acceptance tracking and particle-identification detector in heavy-ion experiments started with NA49 [15] at the SPS (Super Proton Synchrotron) and STAR (Solenoidal Tracker At RHIC) [16] at the RHIC (Relativistic Heavy-Ion Collider).

A comprehensive review covering the working principle of drift chambers and its particle detection capabilities can be found in [17]. The following subsections represent a short compendium of statements and formulas, which are the most important ones for topics treated in the subsequent chapters.

1.3.1 Working principle

A TPC consists mainly of four parts, the drift chamber volume itself, the Read-Out Chambers (ROCs), the Field Cage (FC) and the high-voltage Central Electrode (CE). The FC together with the ROCs and the CE provide a homogeneous electrical field to transport the ionization electrons.

A charged particle traversing the drift chamber leaves a trace of ionization along its path through the drift volume (see figure 1.3). The curvature of its trajectory in a known magnetic field can be used to measure the momentum of the particle. The electrons and ions produced in the ionization process are accelerated in the external electric field and drift towards the ROCs or the CE respectively. The drifting electrons reaching the read-out chambers produce an electron avalanche in the high fields close to the anode wires providing an amplification of the electric signal (see chapter 3 for further details). The read-out signals are then shaped, digitized, processed and stored by means of the data acquisition system.

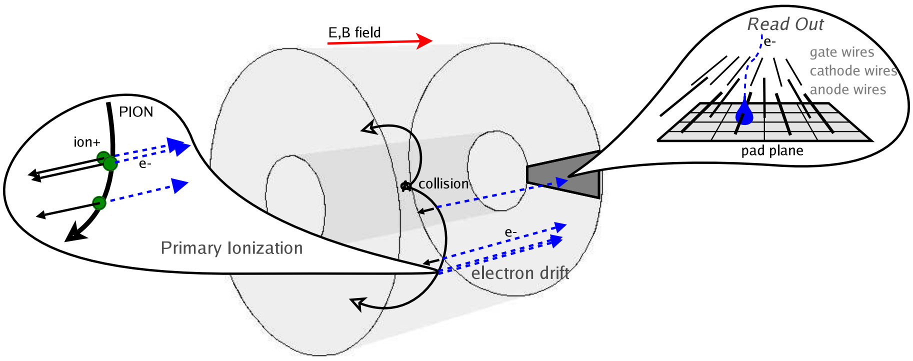

Figure 1.3: Working principle of a drift chamber. Charged particles traversing the volume ionize the gas. The created electrons follow the drift field (E) and are collected in the wire chambers, where they are read out. An overview of the ALICE TPC is shown in figure 1.4.

Gas ionization

The Bethe–Bloch formula (1.1) describes the energy loss per unit of path-length of a charged particle due to Coulomb interactions with the traversed medium [17, p32]. In this formula mc^2 is the rest energy of the electron, N is the density number of electrons in the traversed matter, m and e are the electron mass and charge. I is the mean excitation energy, whereas z and β stand for the charge and the velocity of the traveling charged particle with $\gamma^2 = 1/(1-\beta^2)$ respectively. $\delta(\beta)$ is a correction term to account for density effects, which was calculated by Fermi. It shields the field of the traveling particle.

$$\frac{dE}{dx} = \frac{4\pi N e^4}{mc^2}\frac{1}{\beta^2}z^2\left[\ln\left(\frac{2mc^2}{I}\beta^2\gamma^2\right) - \beta^2 - \frac{\delta(\beta)}{2}\right]. \tag{1.1}$$

Equation (1.1) shows that the energy loss is independent of the mass of the particle, but depends on its velocity β. A graph of dE/dx versus the measured particle momentum is usually used for particle identification within drift chambers. This method becomes problematic as soon as the curves of the different particles start to overlap (e.g. muons and electrons at a momentum of $\approx$ 0.105 GeV/c, see [18, fig 3.4]). In these regions complementary methods have to be used, e.g. the TOF detector information.

Gas ionization by laser rays is described in a different way (see [17, p38]). It is essentially a two photon process of UV laser rays (normally used for calibration purposes) in the drift gas. Since the used gas components (e.g. Neon or Carbon dioxide) usually have a much larger ionization potential than the energy of the UV laser, ionization processes happen with the organic impurities present in the drift gas.

Drift of electrons and ions

The macroscopic picture of the drift of charged particles under the influence of electric and magnetic fields ($\mathbf{E}$,$\mathbf{B}$) can be understood in terms of an equation of motion, for drifting electrons and ions usually named, the Langevin equation [17, 19]:

$$m\frac{d\mathbf{u}}{dt} = e\mathbf{E} + e[\mathbf{u}\times\mathbf{B}]) - K\mathbf{u}. \tag{1.2}$$

In here, m and e represent the mass and the electric charge of the particle whereas $\mathbf{u}$ is its velocity vector. K describes a frictional force proportional to the velocity that is caused by the interaction of the particle with the gas. A steady-state solution can be derived as is shown in [17, p.50]:

$$\mathbf{u} = \frac{e}{m}\tau|\mathbf{E}|\frac{1}{1+\omega^2\tau^2}\left(\hat{\mathbf{E}} + \omega\tau[\hat{\mathbf{E}}\times\hat{\mathbf{B}}] + \omega^2\tau^2(\hat{\mathbf{E}}\cdot\hat{\mathbf{B}})\hat{\mathbf{B}}\right). \tag{1.3}$$

Here $\hat{\mathbf{E}}$ and $\hat{\mathbf{B}}$ denote the unit vectors in the directions of the fields. The drift direction is governed by the dimensionless parameter $\omega\tau$, were ω is defined as $(e/m)|\mathbf{B}|$, carrying the sign of the charge of the moving particle, and $\tau = m/K$ accounting for the frictional force in the steady-state solution for $t >> \tau$. In the absence of the magnetic field, the equation (1.3) simplifies to $\mathbf{u} = \frac{e}{m}\tau\mathbf{E} = \mu\mathbf{E}$, with μ defined as the scalar mobility.

In case of non-parallel electric and magnetic fields, sizable differences between the macroscopic approximation and the microscopic motion can occur. Differences in each velocity component lead to sizable deviations in the angle of motion with respect to the E field. Further discussion regarding this topic can be found in section 2.2.1.

The behavior of ions significantly differs from that of electrons because of their much larger mass and their chemical reaction, besides the fact that they drift in opposite direction due to their opposite charge. In general, their drift velocity is about 1.000 times smaller, as is their diffusion. Further details can be found in [17].

Amplification

Electrons which drift towards a read-out chamber, commonly built as Multi Proportional Wire Chambers (MPWC), are subject to amplification when entering the increasing electric field towards the anode wires. In the vicinity of a wire of radius r, they experience the field

$$E = \frac{\lambda}{2\pi\epsilon_0}\frac{1}{r}, \tag{1.4}$$

wherein λ is the linear charge density on the wire. Once the electric field is strong enough the electron can pick up sufficient energy to ionize another gas molecule and the avalanche starts. The physical processes inside the avalanche are quite complicated, as they involve single and multiple ionization, optical and metastable excitations and energy transfer by collisions between atoms. A proportional wire-read-out operates in a mode where the signal is proportional to the number of collected electrons. This is true as long as the avalanche induced changes of the electric field (space charges) remains negligible as compared to the amplification field of the wire [17, p126]. Further details on signal creation and shapes as well as the influence of ions, produced in the avalanche, are given in chapter 3.

The amplification factor (gain) is described by the first Townsend coefficient α. If multiplication occurs, the increase of the number of electrons per path ds is given by:

$$dN = N\alpha\, ds. \tag{1.5}$$

The Townsend coefficient depends primarily on the excitation and ionization cross sections of the electrons with the gas molecules which do increase with increasing collision energy. Therefore, α heavily depends on the gas composition and density as well as the applied electric field. Thus α is geometry, temperature and pressure dependent.

1.3.2 Performance requirements and technical design

The forseen ALICE physics program [6] determined the performance requirements as well as the design details and the technical construction of the ALICE TPC. To improve the knowledge of hadron physics the following challenges had to be engaged:

- The dE/dx resolution should be at least 8 % or better to properly identify particles.
- The two track resolution has to be sufficient to allow measurements with a resolution in relative momentum of a few (≤ 5) MeV.
- For fast decaying particles a proper (85 % – 95 %) matching capability of the TPC to ITS or/and TOF is needed.
- A tracking efficiency of at least 90 % for tracks of higher momentum (≥ 1 GeV) should be achieved.

- To get a good mass resolution ($\leq$ 100 MeV) for heavy mesons, the momentum resolution for electrons of about 4 GeV should be at least 2.5 %.
- Due to the high luminosity of heavy-ion collisions, the TPC has to operate at 1 kHz or more.

These demands lead to a design of a conventional TPC, but with many new features and novel solutions. The major improvements are [20, 21]:

- *Material budget*: In order to minimize the effect of multiple scattering and secondary particle production, the amount of material between the inner TPC cylinder and the ITS detector was minimized. This determined the light field cage material and influenced the gas choice.
- *Rate capability*: The dead time (between read out) of the TPC had to be optimized. This influenced again, the gas choice, the drift field configuration and therefore the field cage.
- *Acceptance*: For event-by-event studies as well as for all rare observables a reasonably big acceptance was necessary to collect enough statistics. This lead, in combination with the reused L3 magnet, to the biggest TPC ever built.
- *Read-out*: The concept of signal handling was significantly improved by the novel development of a specially designed read-out chip (ALTRO chip, see section 3.3).

Technical design

A comprehensive description of every aspect of the technical design as well as the underlying performance requirements can be found in [20]. A well arranged overview is given in [21] and [18]. Connected calibration issues regarding static and dynamic fluctuations of the field configurations as well as corrections for the non constant drift velocity are given in the dedicated chapters within this thesis as well as in notes quoted later on.

The ALICE TPC is placed inside a solenoid magnet with a nominal field of 0.5 T (L3 magnet) parallel to the drift field in z direction. It has an inner radius of 80 cm, defined by the maximum acceptable hit density of 0.1 cm^{-2} and the outer diameter of the ITS detector. The outer radius of 250 cm is given by the length required for the desired dE/dx resolution as well as the required momentum resolution in the frame of the available magnetic field. To fulfill the desired position resolution ($\sigma_{r\phi} \approx 150\ \mu$m and $\sigma_z \approx 200\ \mu$m) special precautions had to be taken when planning the field cage as well as the inner and outer containment vessels.

The total length of the TPC is 500 cm. In combination with the chosen diameters, it provides charged particle momentum measurement with sufficient momentum resolution, particle identification by dE/dx and by decay topology analysis and vertex determination in the region $\text{p}_t \leq 10$ GeV/c and pseudorapidities $|\eta| \leq 0.9$.

One basic design philosophy of a TPC field cage is to provide a highly uniform electrostatic field in a cylindrical high-purity gas volume to transport primary charges over long distances towards the read-out end-plates while minimizing the distortions (for details, see section 2.3). For reasons of symmetry in colliding beam arrangements, two such field

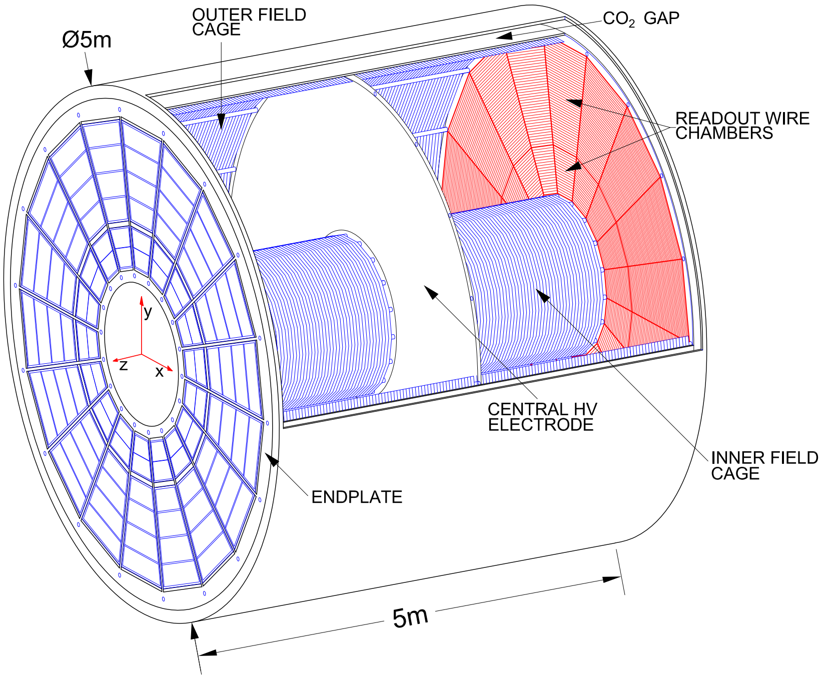

Figure 1.4: Overview of the ALICE Time-Projection Chamber. [22]

configurations are chosen, which are situated back-to-back to each other. The strips of the inner and outer field cage (see figure 1.4) for configuring a uniform field along the axis of the cylinder are made of aluminized Mylar. These are 25 μm thick and 13 mm wide. 166 strips are needed over the 2.5 m length from the central electrode to the end plates on either side (compare [20, sec.3.1]).

The actual field cage volume is surrounded by an insulating gas envelope (*containment*). Containment of the drift volume is essential for minimizing the amount of material traversed by particles. The construction of the field cage and consequently the choice of material are driven by the constraints of high structural integrity against gravitational and thermal loads and very low permeability to atmospheric gas components considered harmful to the drift gas (O_2, N_2 and H_2O). Further details regarding the influence of impurities on the drift gas are given in section 2.1.

The drift gas of Ne-CO_2-N_2 (90/10/5) is optimized for drift speed, low diffusion, low radiation length and multiple scattering and aging properties [23]. The drawback of this mixture is that it has an unusually high dependence of drift velocity on temperature. Thus, the ALICE TPC is aiming for a thermal stability of $\Delta T \leq 0.1$ K (compare section 4.2). The drift gas requires a high drift field (400 V/cm) to secure an acceptable drift time of 96 μs which defines the dead-time of the detector and therefore the rate capability. To reach this high drift field the central electrode must be at 100 kV.

The read-out chambers are situated at the two end caps of the field cage and are built as conventional Multi Wire Proportional Chamber (MWPC). They mainly consist of three layers of wires (anode, cathode, gate) and of about 570.000 read-out pads. Design considerations regarding mechanical structures, wire calculations for signal optimization as well as tests and prototype performances can be found in [20, chap.4]. Details of the MWPC and its signal production are discussed in chapter 3 where special emphasis is laid on the Ion-Tail-Cancellation.

1.3.3 Calibration issues

After careful construction and installation, the TPC is subject to its final calibration. A short description of the installed calibration methods is given in the section 1.4. How static and dynamic imperfections as well as deviations influence the track and space point resolution can be summarized as stated below:

- *Drift velocity*: Due to variations of pressure and temperature within the TPC gas volume, the drift velocity is not constant. Since only the time information is available, this influences the z resolution and therefore the matching capability of the TPC. Further details regarding the temperature and pressure influence on the stability of the drift velocity are given in chapter 2 and 4.

- *ExB effects*: The non-parallelism of the magnetic field with respect to the electric drift field leads to non-linear space point distortions within the drift volume. Measurements of the magnetic and calculations of the electric field imperfections provide a detailed model of the necessary corrections in (x,y,z) (see section 2.2).

- *Field cage inhomogeneities*: electric field inhomogeneities due to mechanical and structural imperfections influence the electron drift direction and therefore the space point resolution in x,y and z. Calculations and simulations regarding their magnitude are discussed in section 2.3.

- *Signal and gain fluctuations*: The desired dE/dx resolution requires a calibration of gain fluctuations within the read-out chambers. Additionally, signal shaping options like moving-average-filters and tail-cancellation have to be performed in order to optimize the signal for high occupancy environments (see chapter 3).

- *Space charges*: In addition to the static field cage imperfections, dynamic variations of the electric field are expected in high occupancy environments like Pb–Pb collision. Necessary corrections will be introduced according to the measured track density (described in chapter 5).

For space point calibration issues (x,y,z deviations) it is foreseen to make use of the built-in laser calibration system. Regarding signal variations as for example timing, shape and gain, the built-in pulser as well as the krypton calibration will be a useful tool. These built-in calibration techniques are shortly described in the following section.

1.4 Methodology of basic calibrations techniques

There are several levels of calibration phases which have to be carried out in a detector like a TPC. Different subsystems and their interactions have to be validated and improved. The focus of the following subsections is laid on the introduction of basic calibration techniques which are used to improve the overall physics performance of the detector. Necessary calibrations of the electronic read-out, e.g. noise, pedestal, gain and time calibration, are discussed in [18]. These calibrations are performed by means of the electronic pulser system which is not discussed in here.

1.4.1 Laser calibration

The laser calibration system provides pulsed UV laser beams with a wavelength of 266 nm [24]. In total 336 such laser beams are reflected into the TPC drift volume (168 on each side). Six laser rods carry four fixed bundles at different z position, wherein each bundle hosts seven micro mirrors which extract the laser beams in order to shoot them into the drift volume. Figure 1.5 displays a sketch of the system.

Since the laser beams provide straight tracks even in the presence of a magnetic field, it makes it the perfect choice to study residual distortions due to mechanical misalignments of the read-out chambers as well as E×B effects, which influence the drifting electrons. Furthermore, it allows to correct for dynamic variations of the drift velocity due to temperature and pressure variations through-out the TPC volume.

Details regarding the design of the pulsed UV laser and the optical system are documented in [25].

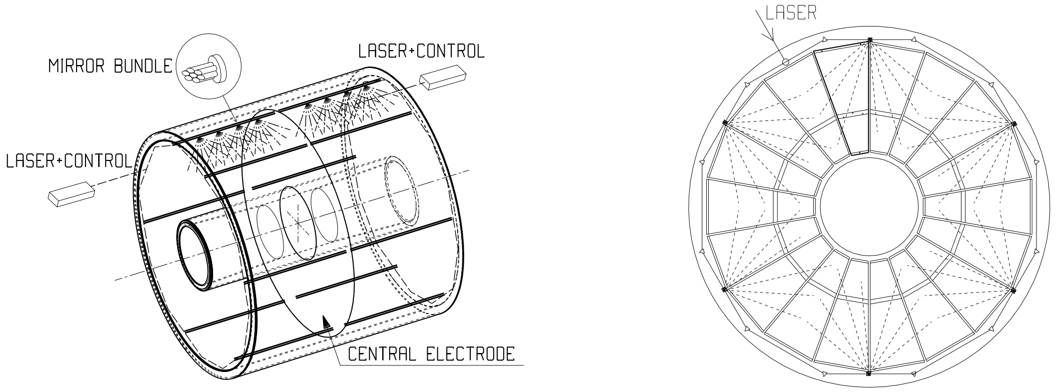

(a) Overall layout **(b)** (x,y)-distribution

Figure 1.5: Laser Calibration system. Figure (a) shows the general layout of the laser system. The laser beams follow the perimeters of the end-plates. For clarity, only tracks originating from one rod are indicated. Figure (b) shows the pattern of the laser tracks at one of the four z-positions at which the mirror bundles are mounted [20].

1.4.2 Krypton calibration

^{83}Rb decays into an isomeric state of the stable isotope ^{83}Kr with a half-life of 124 days. From there on, there are several different but fast decays (max 1.8 h) with a large spread of electron energies (9.4–41.6 keV). This decay chain is well suited for the calibration of energy deposits within a heavy-ion experiment like a TPC [20]. This calibration technique was succesfully used in the NA49 [15] and in the STAR [16] experiments.

The krypton method is well suited to study gas gain variations within the read-out due to mechanical imperfections (wire sag, deformations), gas composition deviations as well as long-term changes in the gas amplification, in particular aging effects. The krypton can be added in an straightforward way to the gas contribution system, thus it is homogeneously distributed over the full drift volume allowing a direct comparison of each individual position of the read-out.

The outcome of the calibration is a gain map which is used to calibrate the energy deposit within the drift gas and to improve the dE/dx resolution of the detector.

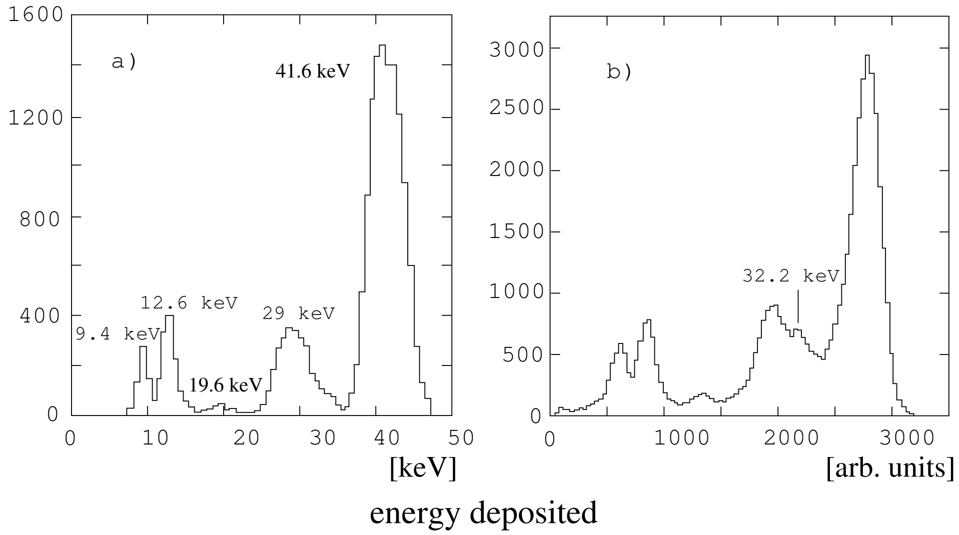

Figure 1.6: Charge spectrum from ^{83}Kr decays in the NA49 TPC. *Left*: Monte Carlo simulation. *Right*: measured spectrum [20].

Chapter 2

Distortions by static imperfections

As discussed in the first chapter, the planning and the construction of a TPC has to take into account several aspects which influence its resolution and therefore its physics performance. Possible distortions, which can not be influenced once the construction of the TPC is finished, have to be considered during the commissioning and calibration phase. Distortions of the drifting electrons, which were liberated in the ionization process within the gas volume, can occur as systematic offsets in the x and y as well as in the time (z) coordinate. These are systematic errors which influence the space point resolution of tracks significantly. Such errors have to be minimized during the design of the detector or/and quantified and corrected with the help of calibration procedures.

One major concern to reach the design goal of 200 μm (or due to diffusion, 600 μm for the full drift length) for the resolution in the z direction is the drift velocity and the diffusion of the electrons, which are detected at the read-out plates. In general the drift velocity as well as the longitudinal and transversal diffusion have a strong dependency on the field configuration and the gas density, whereas the gas density is in turn a function of the gas composition, the temperature and the pressure of the gas. Calculations regarding how their dynamic variations influence the drift velocity are discussed in chapter 4.

This chapter presents the influence of static imperfections. Impurities of the chosen gas mixture and their influence on the drift velocity as well and on the diffusion of the electrons are discussed in section 2.1. Field inhomogeneities due to field cage imperfections, which influence the electric drift field of the electrons, are discussed in section 2.3. Static imperfections of the magnetic field were measured beforehand. Its consequent distortions can be found in section 2.2. Details regarding the motion of electrons, which are necessary to understand the essence of the above mentioned distortions, are given in the following paragraphs:

Motion of electrons

Electrons in vacuum, when subject to an electric field **E** and a magnetic field **B**, are driven by the Lorentz force. Their motion can be described by

$$m\dot{\mathbf{v}} = q\left(\mathbf{E} + \mathbf{v} \times \mathbf{B}\right), \tag{2.1}$$

where e is their charge and m is their mass. This results in tracks which have the form of a helix. When traveling through a gas, they do not follow such orbits, at least not on a scale much larger than the mean free path which is typically a few microns in detector gases at standard temperature and pressure. They move along straight lines instead, which is a consequence of the frequent collisions with gas molecules which continuously randomize the electron velocity. A steady-state solution for the different drift velocity components is given by the Langevin equation (1.3). In there, τ stands for the transient time needed to reach the steady-state drift velocity. It is worth to mention that the mobility $\mu = e\tau/m$ depends on the electric and magnetic fields.

Besides the calculation of the drift velocity by means of the Langevin equation, one can use Magboltz [26], which computes the drift velocity using Monte Carlo techniques, tracing electrons at the microscopic level through numerous collisions with gas molecules. As can be seen in subsection 2.2.1, there can be sizable differences between the Magboltz and Langevin velocity components and therefore, between the real and the ideal motion of the electron when traversing a gas-filled volume. These differences occur because the τ variations, and therefore the mobility variations due to different cross sections in dependence of gas density and field variations are not taken into account when using the steady-state solution (Langevin equation).

Diffusion

Charged particles move on average along an applied electric field. On the way, their drift velocity deviates from the average due to scattering on the atoms of the gas. Scattering leads to variations of the drift velocity in terms of magnitude as well as direction, creating longitudinal and transverse diffusion. In constant electric and magnetic fields the diffusion is, in general, of Gaussian form [17, p.68].

In general, the diffusion is determined by the energy of the drifting electron. In drift chambers we therefore require small electron energies at high fields in order to minimize the diffusion as well as the dead time of the detector. For example, Argon is considered to be a “hot gas” due to the fact that even at low drift fields of 1 V/cm, the electron energies are larger than thermal. Applying a magnetic field generally decreases the diffusion.

2.1 Gas density fluctuations

The choice of the drift gas is of major concern due to its influence on diffusion and drift velocity and therefore, on the detector resolution. A general overview on drift-chamber gases is given in [17, chap.12]. Details regarding the considerations undertaken while choosing the ALICE TPC mixtures can be found in [27]. It was found that a Neon-based mixture is the best choice for high multiplicity environments.

Gas density is, besides field variations, the main contributor to variations in terms of drift velocity and gain. How environmental variations, like pressure and temperature fluctuations, influence the gas density and therefore the drift velocity, is discussed in chapter 4. In this section, mainly impurities in terms of the gas mixture itself are discussed, since they can be considered as long-term and therefore static imperfections.

By reviewing the design parameters, like low diffusion and low sensitivity to external parameters, or high ionization rates including rapid ion evacuation, a neon based mixture was found to be the best choice for high luminosity environments. As a quencher for neon-based mixtures, carbon-dioxide is a natural choice. How the addition of nitrogen as a third component influences the gain stability and therefore the stable operation of the ALICE TPC is discussed in [23].

The drift volume of the ALICE TPC is therefore filled with a mixture of Neon (Ne), Carbon-Dioxide (CO_2) and Nitrogen (N_2). Their different quotas are 85.72 %, 9.52 % and 4.76 % respectively. The thermal isolating buffer volume surrounding the TPC is filled with pure CO_2 and some leakage from the buffer volume into the main TPC volume can not be excluded. Due to atmospheric leakage, contaminations by N_2 or oxygen impurities can not be excluded. The standard drift field of the ALICE TPC is set to 400 V/cm within an over-pressure environment (0.4 mbar above atmospheric pressure).

2.1.1 Gas properties of a (Ne-CO_2-N_2) mixture

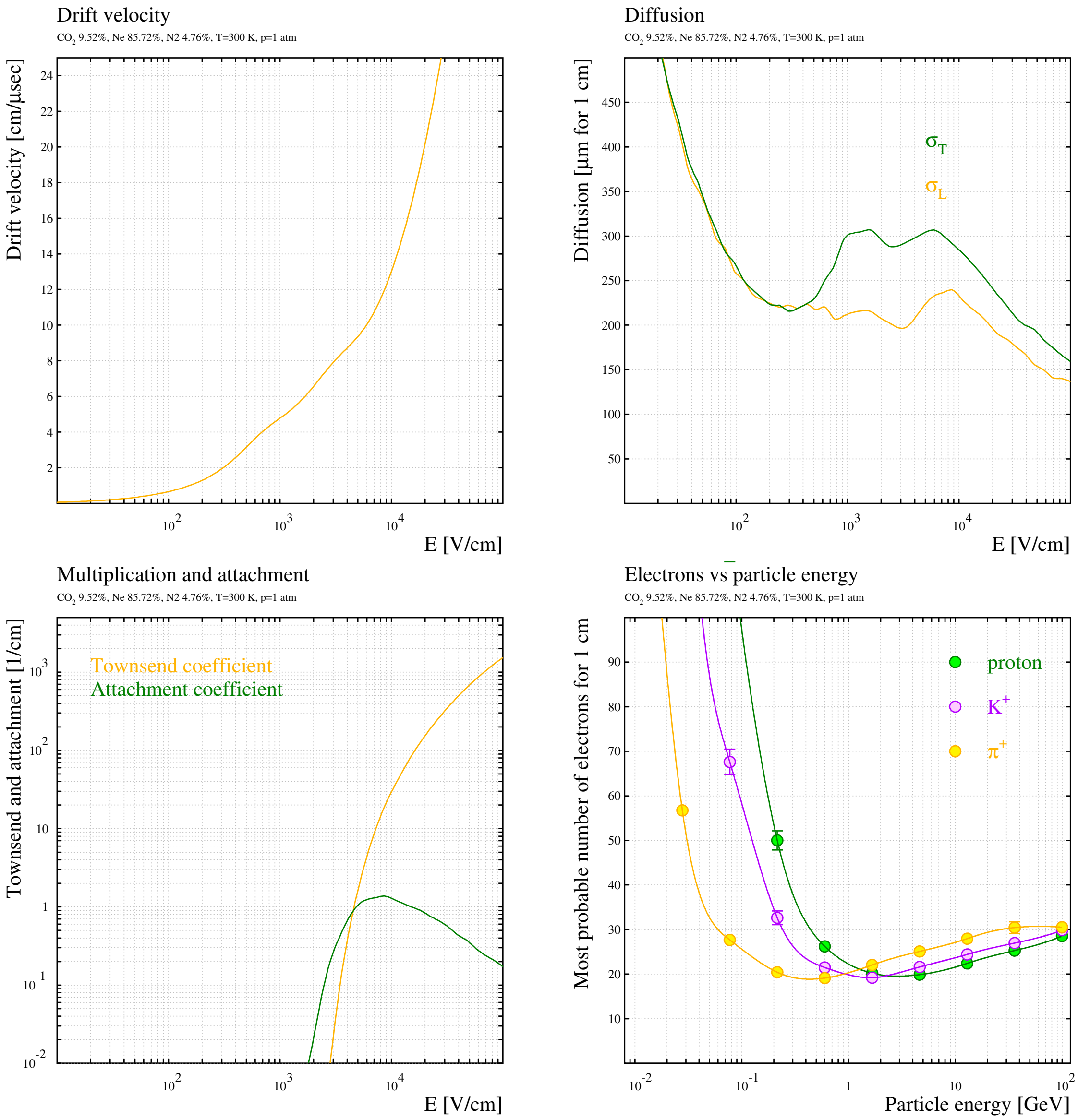

Figure 2.1: Electron transport and ionization in Ne-CO_2-N_2 (at 300 K and 1 atm). The standard drift field E of the ALICE TPC is 400 V/cm.

The main gas properties for a gas mixture of Ne-CO_2-N_2 (90/10/5) are reviewed in a similar way as was done for Ne-CO_2 in [28]. The transport parameters of the gas mixtures have been computed with Magboltz [26]. This program uses Monte Carlo integration techniques as well as gas properties with varying cross sections. The fluctuations in the graphs reflect the statistical accuracy. High-precision measurements of the drift velocity in Ne-CO_2 (90/10) in dependence of various parameters were performed in [29], which showed good agreement to the simulations in Magboltz.

Transport properties at low E/p for varying CO_2 fractions

In general, adding CO_2 to Ne produces very slow gas mixtures but is the ideal choice in terms of a needed quencher. Unfortunately, the drift velocity is highly sensitive to the fraction of CO_2 when there is less than 20 % CO2 in the mixture. In order to minimize the dead-time, a high drift velocity is needed. Therefore the fraction of CO_2 should not exceed 10 %. Already in this region, the drift velocity changes by approximately 6 % when varying the CO_2 fraction between 9 % and 10 %, as can be seen in figure 2.2.

The addition of CO_2 leads to low diffusion coefficients. Like for the drift velocity, the diffusion coefficients tend to vary strongly when the CO_2 fraction in pure Ne is less than 10 %. In combination with N_2, these variations can be kept small. In contrast to the longitudinal diffusion ($\sigma_l \approx 220\ \mu$m/cm), the transversal diffusion still contains a slight dependency at higher fields with increasing CO_2 fraction.

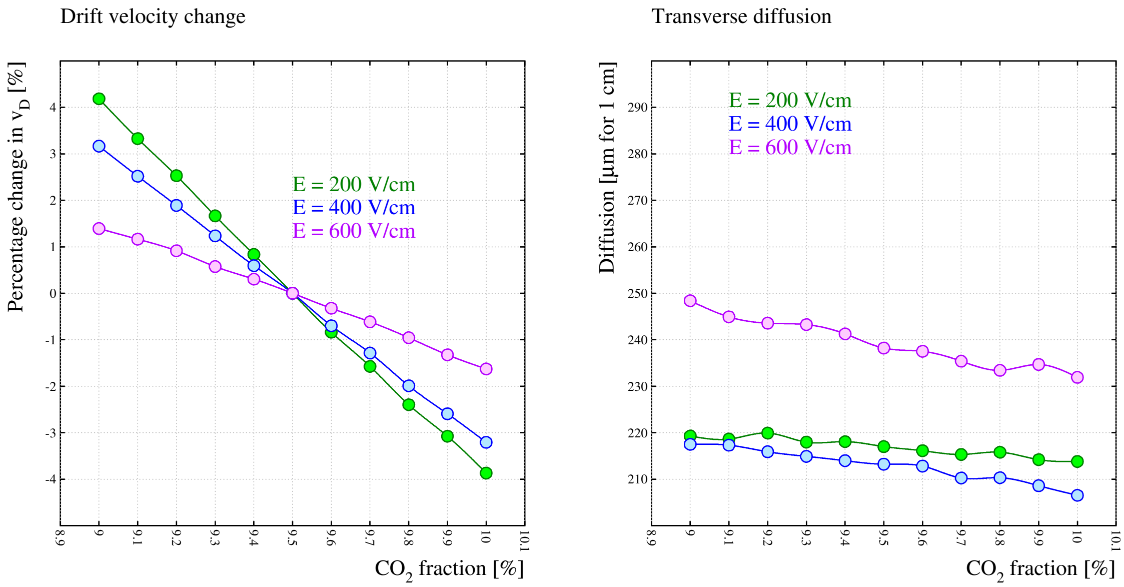

Figure 2.2: Transport properties at low E/p for varying CO_2 fractions in Ne-CO_2-N_2 (at 300 K and 1 atm).

Transport properties at low E/p for varying N_2 fractions

Adding small amounts of N_2 to a Ne-CO_2 gas mixture leads to a reduction of the drift velocity (approximately 2 % per percent of N_2). Already a 100 ppm contamination, due to atmospheric leakage, would lead to a bias in the drift direction of the TPC up to 250 μm. This negative effect can be reduced by adding a higher percentange of N_2 to the

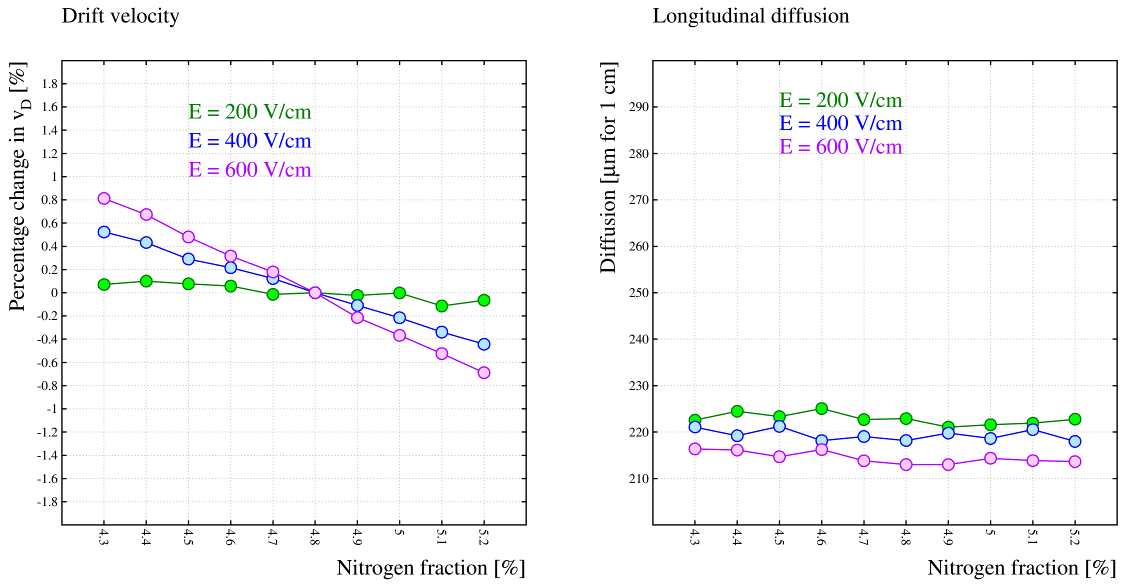

Figure 2.3: Transport properties at low E/p for varying N2 fractions in Ne-CO_2-N_2 (at 300 K and 1 atm).

drift gas mixture. Additional positive effects like more effective Penning transfers onto ionisation and therefore an operation at lower gain at no penalty for the charge transport and amplification properties are discussed in [23].

As is sshown in figure 2.3, the N_2 admixture has little effect on the longitudinal diffusion. The same applies for the transverse diffusion coefficients ($\sigma_l \approx 220$ μm/cm for a 400 V/cm field). The remaining drift velocity dependence is in the range of 1 % per percent of N_2 variations at nominal environmental conditions and nominal drift field of 400V/cm.

2.1.2 Variations due to impurities

The planning and the construction of a gas system is evidently driven by the attempt to hold the fraction of the different gas components as constant as possible while minimizing leakages from surrounding gas vessels and systems (CO_2, SF_6) and atmospheric contaminations (N_2,O_2, H_2O). While fractional variations (imperfections) of CO_2 and N_2, which were discussed in the previous section, lead mainly to changes of the drift velocity and diffusion, the impurities as discussed in this section can cause sizeable attachment losses [28].

In order to fulfil the requirements on high gas stability and purity, the gas system was built and tested for minimal leakage rates and hosts additional monitoring and control systems like gas chromatography and the GOOFIE system [30].

Effect of adding oxygen (O_2) or SF_6 to a Ne-CO_2-N_2 mixture.

Due to atmospheric leakage, O_2 contaminations can not be excluded. Due to the usage in other detector components, the presence of some level of SF_6 contamination can not be excluded either. The major effect of such impurities is a loss of ionization electrons due to the electronegative properties of SF_6 and O_2. Especially for that reason, SF_6 is particularly interesting for RPC detectors which are operated at very high fields and lead to large Townsend coefficients and therefore to excellent time resolutions. However, even small amounts of contaminations can lead to serious loss of ionization electrons in detectors with low field but long drift distances such as TPCs.

Small O_2 fractions have little effect on the transverse and the longitudinal diffusion coefficients and essentially no effect on the drift velocity. In contrary, SF_6 admixtures slightly decrease both the transverse and the longitudinal diffusion coefficient but unfortunately, the drift velocity as well.

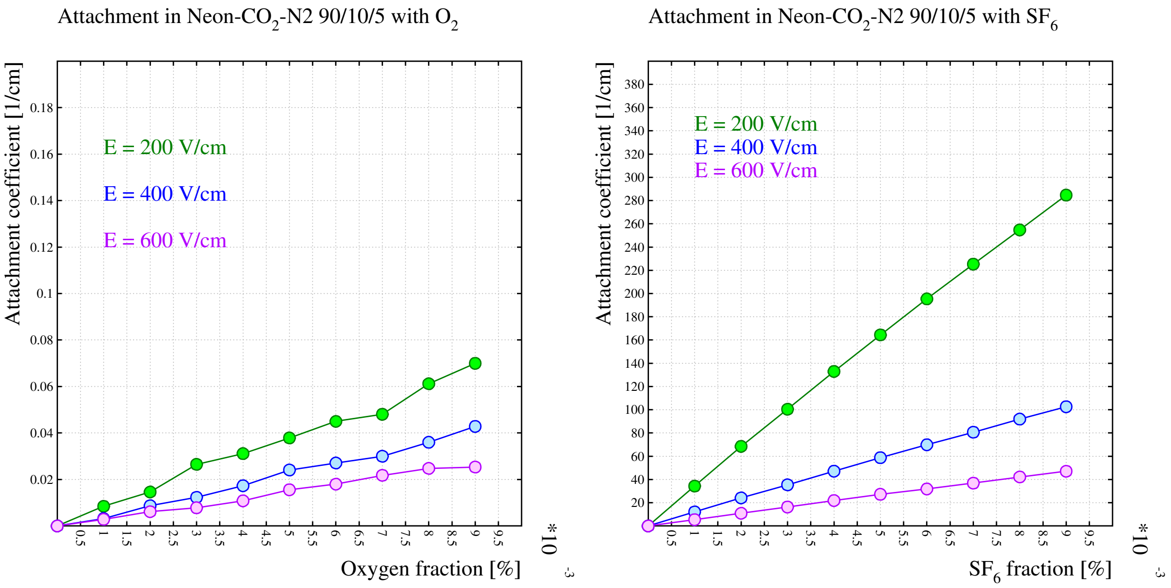

Figure 2.4: Effect of adding O_2 or SF_6.

The attachment coefficient and therefore the electron losses rise approximately linearly with the percentage of O_2 but increase faster than linearly with the electric drift field. The losses due to a SF_6 contamination rise faster than linearly with the percentage of SF_6 as well as with the electric drift field.

However, in comparison to O_2, SF_6 has a much higher electro-negativity which explains the magnitude of the difference in the attachment coefficient in figure 2.4. At the nominal drift field of 400 V/cm, the attachment coefficient is of the order of 15000/cm per % of SF_6 and about 3.5/cm per % of O_2 (for the gas of Ne-CO_2).

However, for a required 50 % probability of the electrons to survive 2.5 m drift, the O_2 level should not exceed 8 ppm. The demands on SF_6 absence are even higher; the SF_6 level should not exceed 2 ppb.

Effect of adding water to a Ne-CO_2-N_2 mixture.

Similarly as with O_2, small fractions of water contaminations due to atmospheric leakage can not be prevented. Their effect would be, that they reduce the transverse and the longitudinal diffusion coefficient.

At a drift field of 400 V/cm, 1 % of water reduces the drift velocity by 35 % (see figure 2.5) whereas with increasing water contamination, the diffusion coefficients would

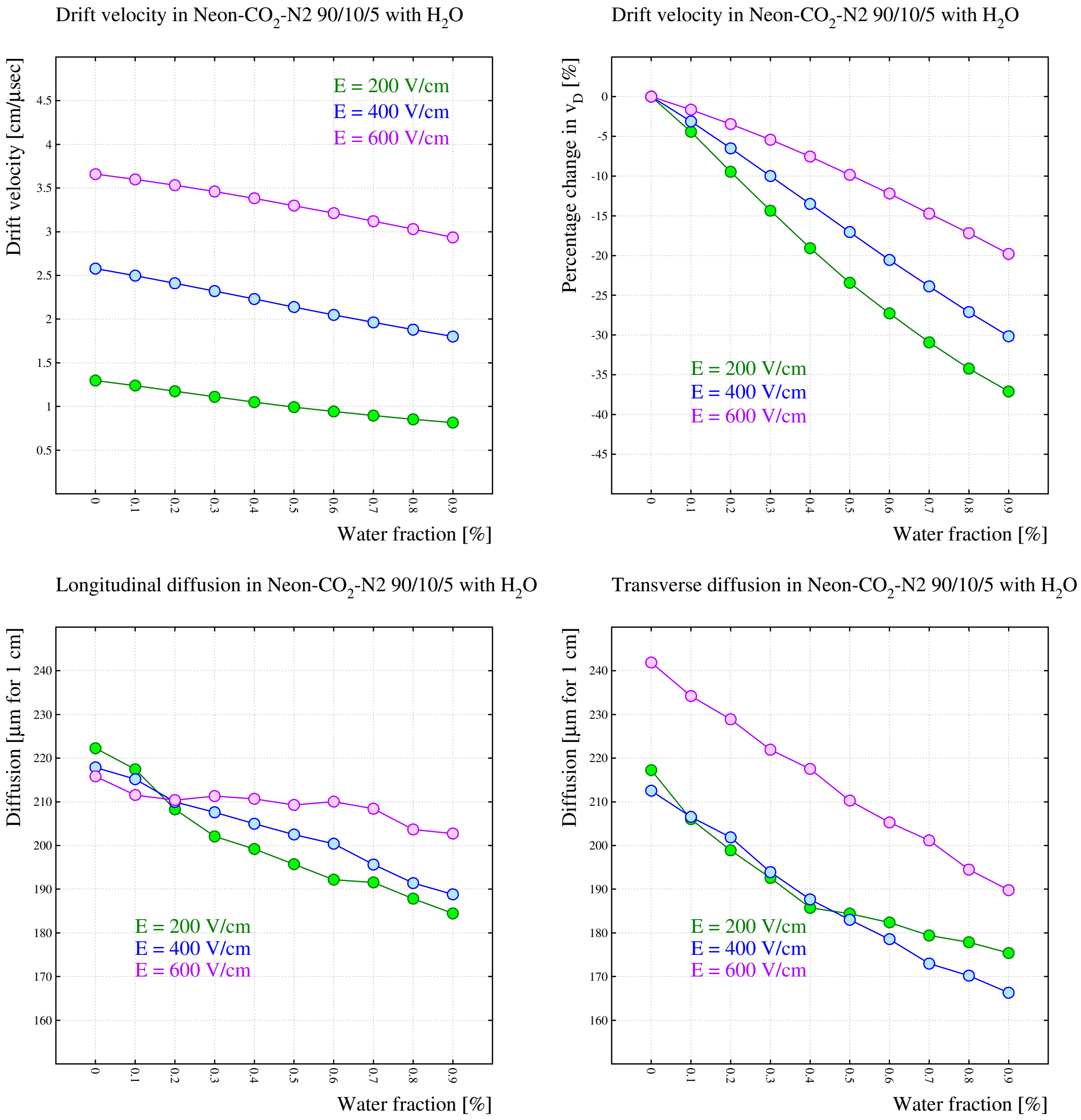

Figure 2.5: Effect of adding water to a Ne-CO_2-N_2 mixture.

decrease. However, the water contamination has to be kept as small as possible to minimize the effect on the drift velocity. Contaminations at the 10 ppm level as given in [20] are expected to lead to about 0.05−0.07 % change in the drift velocity. To comply with the resolution requirements, the contaminations have to be kept below 1.5 ppm.

According to Magboltz calculations, losses of electrons are negligible up to drift fields of 600 V/cm. However, they would become significant at higher electric fields. Since the nominal drift field of the ALICE TPC is 400 V/cm, this effect can be be neglected.

2.1.3 Temperature sensitivity

The drift velocity depends strongly on the energy of the electrons, not only induced by the electric field but also due to thermal motion. Therefore, changes in drift velocity induced by temperature variations have to be considered.

The main dependency on temperature variations was simulated with Magboltz and is shown in figure 2.6. The same dependency was reproduced in measurements [29]. For electric fields in the range 100−1000 V/cm the temperature sensitivity near 300 K is of the order of 0.1−0.35 %/K.

More details and refined simulations can be found in chapter 4.

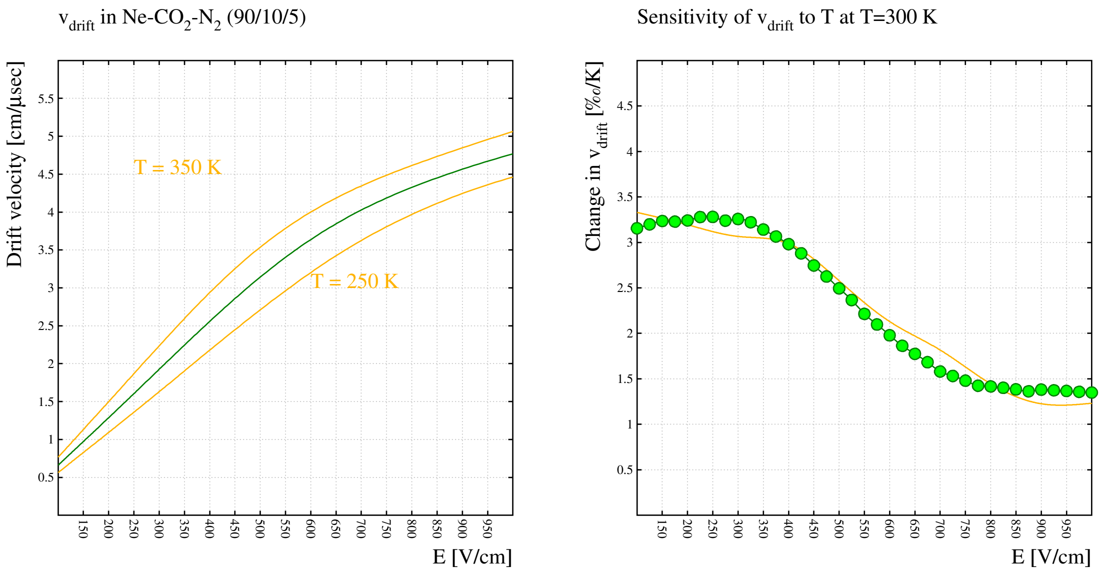

Figure 2.6: Sensitivity to temperature variations. *Left*: drift velocity versus electric field for different temperatures; *Right*: change of drift velocity per Kelvin versus electric field at a temperature of T=300 K.

2.2 B field uniformity

The central detectors are placed within the so-called L3 magnet, which provides a magnetic field in z direction (beam direction) which can be varied in the range of ±0.5 T. The magnetic field vector is parallel to the electric field vector within the TPC drift volume (see figure 1.2). An additional dipole magnet is alligned in the direction of the muon arm spectrometer.

If the magnetic field is perfectly parallel to the electric field (E||B), the drifting electrons trajectories are not distorted at all. However, due to mechanical imperfections of the L3 magnet, this is not the case. Even small inhomogeneities, which lead to a non-parallelism of the E and B field, have an influence on the electrons given by the so-called Lorentz force. In such a case, the E×B term in equation (1.3) is not zero. This effect scales with the drift length and leads to a systematic error of the cluster position and therefore, the curvature of the track. The result is a systematic error in the momentum determination and resolution.

Especially for the ALICE TPC, with its long drift length of 2.5 m, the field imperfections have to be known to the level of 10 Gauss. Thus, both magnetic fields (solenoid and dipole) were measured in advance to provide a detailed knowledge of its imperfections. The measurements were performed with 3D Hall probes before the detectors were in place. The measured points were then corrected according to the detector occupancy (new boundary conditions) and parametrized with Chebyshev polynomials. Details regarding the measurements and the parameterizations can be found in [31] and [32].

The CPU efficient parametrization with Chebyshev polynomials is implemented in the class *AliMagFMaps* within the ALICE Off-line framework for simulation, reconstruction and analysis [33]. Figure 2.7 represents a general overview of the magnetic field imperfections which are in the range of 2 %.

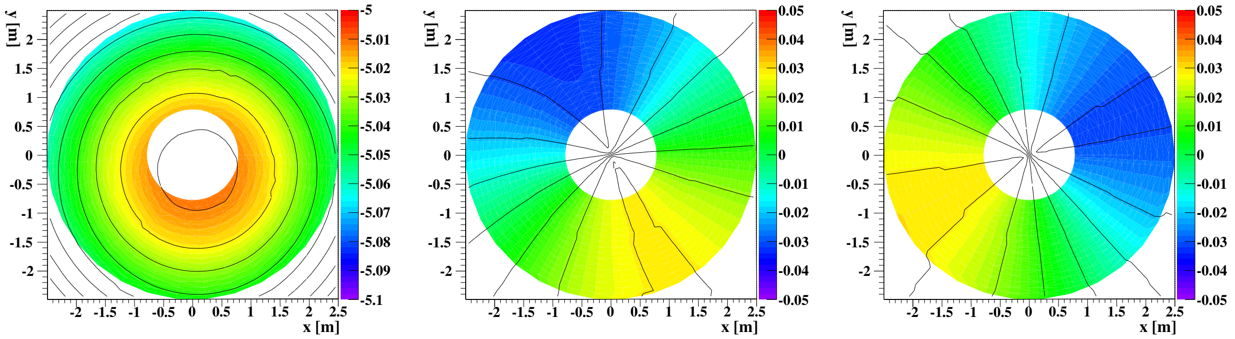

(a) B_z **(b)** B_r **(c)** B_ϕ

Figure 2.7: MAGNETIC FIELD WITHIN THE TPC in kGauss at z=0 m. Visible are the inhomogeneities which reach 2 % in the volume.

In order to calculate the resulting distortions, the Langevin equation (1.3) has to be solved. This can be done in two ways. Either assuming a constant mobility within the numerical solver (e.g. see [34]) or including possible variations of the mobility which manifest themself in form of different Lorenz angles. Different magnitudes of the velocity components in the (r,ϕ,z)-directions are the result. A Monte Carlo based method like Magboltz can be used to simulate the influence of different gas compositions on the Lorenz angle. Both methods are compared in the following subsection.

2.2.1 Lorenz angle calculations

The Lorenz angle depends on the gas composition and the angle between the E and B field. It can be calculated by means of MC techniques (see Magboltz [26]) or by solving the Langevin equation for a constant electron mobility μ. Sizable differences between the Magboltz and Langevin velocity components are possible, whereas the Magboltz method, being based on the atomic cross sections, is more accurate. In general, Magboltz values have shown good agreement with pertinant measurements, as for example for Ne-CO_2 mixtures [35, 36].

Angles between the resulting velocity components are compared for two different gas compositions at different operating conditions (drift fields and gas densities) and are shown in figure 2.8 and 2.9. The mobility used for the Langevin equation has been chosen in such a way that the curves overlap for parallel E and B fields ($\mu = v/E$ with velocity v at $\angle(E, B) = 0$).

As discussed in the introduction of this chapter, a gas mixture of Ne-CO_2-N_2 (90/10/5) is used for the ALICE TPC. The Magboltz calculations were performed for a temperature of 300 K at an ambient pressure of 1 atm, whereas the nominal drift field of 400 V/cm within a magnetic field of 0.5 T was used.

Another commonly used drift gas is P10, namely Ar-CH_3 (90/10). The field configurations were chosen according to the setting which are used in the STAR TPC [16]. At nominal ambient conditions as above, the drift field was set to 135 V/cm with a magnetic field of 0.5 T.

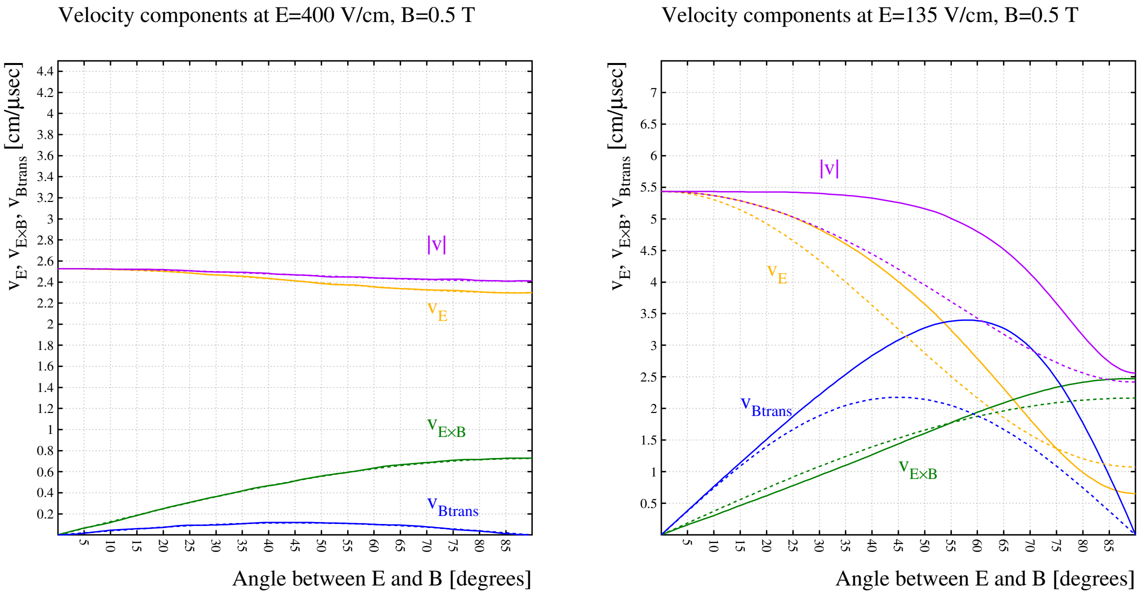

Figure 2.8: VELOCITY-COMPONENTS OF DRIFTING ELECTRON IN DIFFERENT GASES calculated with Magboltz (dotted lines) and the Langevin method (solid lines); *Left*: Ne-CO_2-N_2 (90/10/5); *Right*: Ar-CH_3 (90/10).

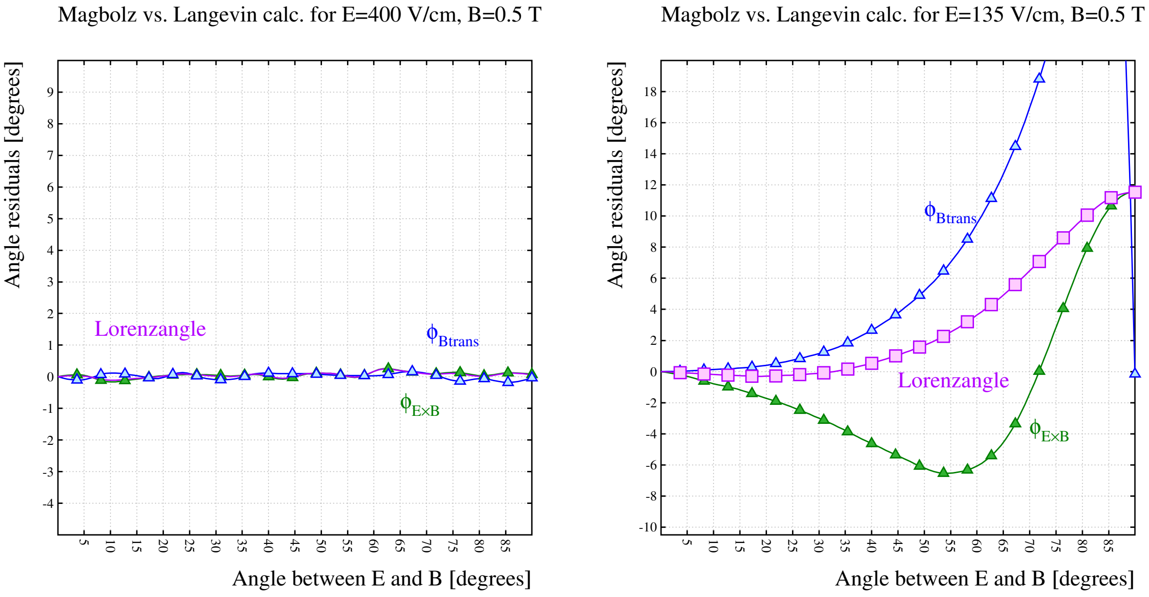

Figure 2.9: DIFFERENCES OF THE VELOCITY-COMPONENT-ANGLES between the Magboltz and the Langevin method; *Left*: Ne-CO_2-N_2 (90/10/5); *Right*: Ar-CH_3 (90/10).

As shown in figure 2.8, for Ne-CO_2-N_2, the Langevin method displays excellent agreement over the full range of (E,B) angles in comparison to the velocity components, which were calculated via Magboltz. In contrast, P10 displays good agreement at small angles between E and B, but considerably larger differences at larger angles. In terms of Lorenz angle, this means that the neon gas mixture shows an agreement of $\Delta\phi_{max}$~$0.1°$ over the full range, whereas P10 leads to errors smaller the $\Delta\phi$~$1°$ at angles $\angle(E,B)$~$10°$ (see figure 2.9).

The term $\omega\tau$, as used in equation 1.3, is directly proportional to the mobility μ and the Lorentz angle ϕ via the relations $\omega\tau = \mu B = \tan\phi$ and is therefore a common factor which is to be considered when choosing the drift gas and the drift conditions. For the ALICE TPC gas composition, $\omega\tau$ is approximately 0.31, whereas for the gas P10 as it is used in the STAR TPC, $\omega\tau$ is 2.01. A higher $\omega\tau$, which implies a higher B field, has the advantage of good momentum measurements with high accuracy even for small track lengths; but one must account for the higher sensibility to E×B effects.

As long as the imperfections of the parallelism of E to B can be kept as small as possible, one certainly prefers larger factors of $\omega\tau$. But, since the ALICE TPC is dedicated to heavy-ion physics, the magnitude of expected space charges and therefore E field deviations are rather large. For that reason, a gas composition with small $\omega\tau$ was preferred. More about space charge effects and their influence on cluster positions is given in chapter 4.

However, thanks to the chosen gas composition and the negligibly small errors of the Langevin approximation, one can use efficient numerical algorithms to calculate the distortions due to E×B effects.

2.2.2 E×B effect

The Langevin equation mentioned in section 1.3 is used to track charged particles along their drift path. If the applied electric field is perfectly parallel to the applied magnetic field, the electrons within the TPC would have straight paths along the drift in z direction.

Anyway, assuming an E field perfectly homogeneous in the z direction, the electrons still experience distortions along their drift path due to B field imperfections as delivered by the L3 magnet. Within the ALICE TPC, these distortions are throughout nonlinear. This so called E×B effect is considered in the calibration algorithm within the AliRoot framework [33]. Previous calculations of this effect, which can be found in [20] and [34], are heavily dependent on the assumptions on the underlying B field imperfections. These imperfections are finally available in form of Chebychev parameterizations within the AliRoot framework.

The magnitude of these distortions varies with the non-constant drift velocity within the gas volume. However, to give an idea of the systematic offsets of the cluster position in dependence of their drift length and their initial positions, corresponding graphs are plotted in figure 2.10. Distortions in time (z) direction are found to be negligible ($\leq$ 30 μm) when assuming an ideal electrical field. The maximum distortions in the r direction are in the range of 3 mm, whereas in the rϕ direction, they reach values up to 7 mm.

The current implementation of the E×B correction uses a pre-calculated look-up table, where the corresponding distortions are listed in dependence on the measured cluster

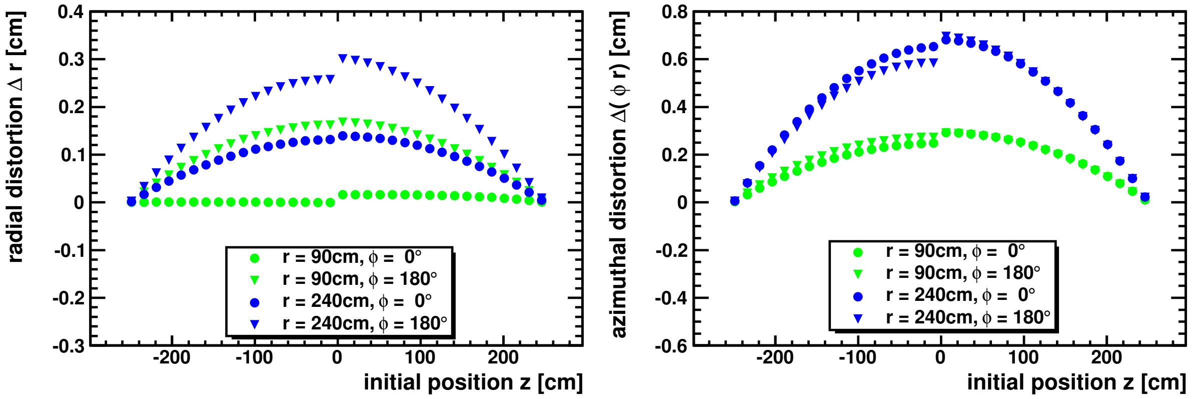

Figure 2.10: SIMULATED DISTORTIONS DUE TO E×B EFFECTS for selected cluster positions. The non-continuity at z=0 is due to the non-symmetric B field on the positive and negative z side.

position. The original (undistorted) position is simply found by subtraction (see class *AliTPCExB* in [33]).

E×B effects due to E field inhomogeneities close to the field cage are negligible. However, when including E field variations due to space charges, this effect becomes important again. Further considerations regarding this topic are given in chapter 4. Static E field imperfections and how they influence the electron drift are discussed in the following section.

2.3 E field uniformity

One of the most challenging tasks in planning and building a TPC is to provide a highly accurate and uniform electric field for the drift volume. Besides that, the field cage structure must provide a gas-tight envelope while having a minimal material budget. Details regarding the composite materials, the support rods as well as the (high)-voltage system are given in [20, chap.3].

Deviations from the ideally linear drift field of 400 V/cm appear close to the field strips, at the crossing to the central electrode, at the crossing to the read-out chambers as well as at the transit of the inner to the outer read-out chamber geometry. Global field misalignments can occur when the mechanical structure is compromised. Read-out chamber misalignments as well as the mechanical field cage support have to be close to perfect. Any imperfection has to be understood in order to provide a global understanding of the electron deviations throughout the drift volume. Certain analytical as well as numerical methods allow the detailed calculation of such systematic errors in the electrical field. Analytical methods, like solving the Laplace equation in cylindrical coordinates with varying boundary conditions lead to a global understanding of possible distortions [37]. But this method can not be used to include effects due to certain structural details like strips, skirt or covers as they are used in the ALICE TPC field cage (see subsection 2.3.1).

On the other hand, Finite Element programs like ANSYS [38] allow the detailed simulation of such structures at the expense of long computing times. Anyhow, semi-analytical methods are implemented in Garfield [39] which do have the advantage of combining the field calculations with algorithms to drift the electrons. Therefore, Garfield allows a direct evaluation of the distortions which are expected due to E field imperfections.

2.3.1 Field cage strips and read-out chambers

During the planning phase of the ALICE TPC detailed simulations were performed [28]. The following paragraphs provide a brief overview on the parameters, which are important for the understanding of the subsequent sections. Details regarding composite materials, dimensions and schematic overviews, which were the base for the following models and simulations, can be found in [22] and [18].

Strip structure

The TPC Field Cage (FC) consists of the high-voltage Central Electrode (CE), the FC-strips with descending potential and the read-out chambers, defining the zero potential.

The strips, which provide the drift field boundaries in radial direction, are connected to each other by a potential degrader system with 7.5 MΩ between each strip. For the sake of security and stability, this is realized via two 15 MΩ resistors in parallel. How possible resistor imperfections influence the drift field is discussed in [37]. Each strip has a width of 1.3 cm with a gap of 0.2 cm between each pair of strips, thus making up 165 strips over the full drift length of 2.5 m. Technical reasons did not allow the installation of the last strip close to the CE, thus introducing additional imperfections in this region.

The drift field of 400 V/cm is obtained by applying a voltage of 100 kV to the CE. See paragraph 2.3.2 for further details. Due to this structural design, variations of the

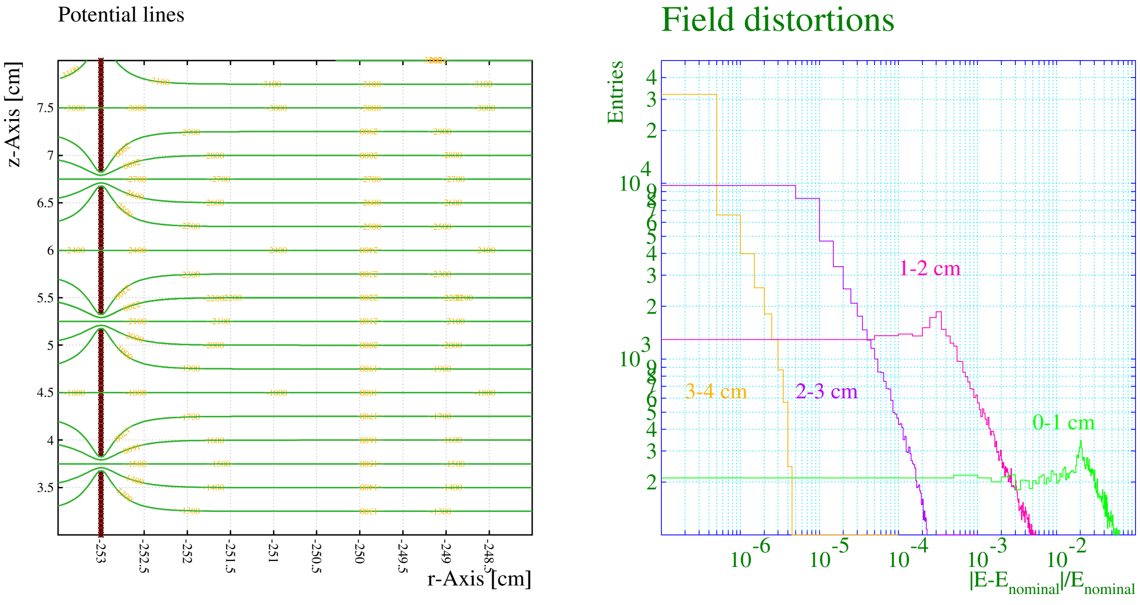

Figure 2.11: FIELD DISTORTIONS AT THE FIELD CAGE STRIPS. *Left*: Strip structure of the outer field cage including potential lines. *Right*: Magnitude of field distortions at different distances to the field cage [28].

electric field along the field cage can be kept smaller than 10^{-4} with a minimum distance of a few centimeter, as can be seen in figure 2.11.

Field distortion due to possible broken resistors within the degrader system as well as shortened strips introduce major field deviations in comparison to the nominal drift field. The laser calibration system can be used to identify their positions by means of pinpointing to the largest drift deviations. If such cases occur during the operations of the TPC, they have to be corrected mechanically. More details are given in subsection 2.3.3

Read-out chamber design

The TPC Read-Out Chambers (ROCs) are multi-wire proportional chambers with a cathode (pad) plane. Details regarding thickness of and distances between the wires is given in chapter 3, where the resulting signal shape is discussed. All wire potentials are adjustable in order to maximize their read-out efficiency and minimize the ion feedback. Since the ROCs have to act as the zero potential line for the field cage geometry, the potential setting has to be conform with the ROC position in respect to the field.

In here, the mechanical structure and size of the aluminium body with respect to the position of the field cage strips are discussed. Due to the distances between inner and outer read-out chambers (I-ROC, O-ROC) additional field imperfections are introduced within this region. To minimize these effects, additional covers (edge strips) with adjustable voltages were introduced at the edges of the chambers. Furthermore, a so called “skirt” strip between the O-ROC and the outer FC was necessary due to their rather large distance of ≈6 cm. The skirt strip homogenizes the field in this region.

Figure 2.12 contains the resulting drift lines of electrons within the dangerous regions. Drift distortions in dependence of the original cluster position and due to the different

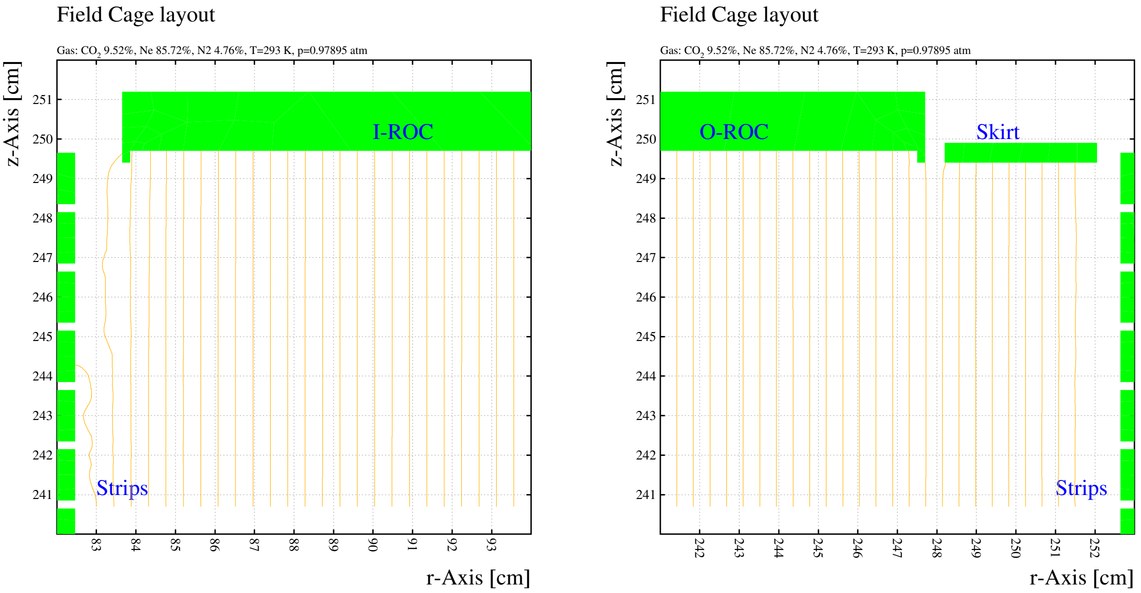

Figure 2.12: ELECTRON DRIFT LINES IN THE IMPERFECT FIELD CAGE REGIONS. *Left*: close to the inner read-out chamber. *Right*: close to the outer read-out chamber including the skirt strip.

effects are discussed in subsection 2.3.3.

Since the I-ROCs are very close to the inner field cage strips ($\approx$ 1 cm), they already see electron distortions due to the non-uniformity of the strip structure of the field cage (compare figure 2.11). However, thanks to the larger distance ($\approx$ 5 cm) and the additional skirt strip at the edge of the O-ROCs, this effect is negligible there (compare subsection 2.3.3).

2.3.2 Optimized voltage settings

As discussed before, the voltage applied to the central electrode is U_{CE}=-100 kV. This setting forces a certain voltage drop per strip along the field cage in z direction (voltage degrader system). The positions of the last strip, the ROCs as well as the skirt bar define their individual voltage settings in order to avoid field perturbations and to stay in conformity with the potential lines.

The voltage degrader system consists of a resistor chain of 166×2 parallel resistors, each having a resitance R_p=15 MΩ plus a last set of parallel resistors of two times R_p plus R_l=10 MΩ (see [18, p27]). The total resistance of one resistor chain is therefore

$$R_{tot} = 166 \cdot \frac{R_p R_p}{R_p + R_p} + \frac{2 R_p R_l}{2 R_p + R_l} = 1249.29\ M\Omega.$$

The measured current is then -80.05 μA. A broken resistor could be identified by measuring a lower current (e.g. -79.57 μA for one broken R_p) due to the higher total resistance. The voltage applied at the n-th strip can be calculated via

$$U_n = \left(\frac{R_p R_l}{R_p + R_l/2} + (n-1) \cdot \frac{R_p R_p}{R_p + R_p} \right) \cdot \frac{U_{CE}}{R_{tot}},$$

where n=1 is the strip closest to the read-out chamber. For the voltage of the first strip we therefore get U_1=-343.05 V, whereas (U_2, U_3, U_4,...) have the values (-943.4 V, -1.543.7 V, -2144.1 V) respectively. The voltage drop per 1.5 cm, which is the distance between each strip, is therefore 600.34 V which leads to a nominal drift field of E_z=400.23 V/cm.

According to the newest survey data [22], the gate wire position as well as the skirt and cover bar positions with respect to the middle position of the last strip have changed. Their change in position implied a recalculation of the necessary voltage settings in order to minimize the field distortions.

Table 2.1 contains their new positions (distance d_z) with respect to the center of the last strip as well as their newly calculated voltage settings for both sides of the TPC (A and C side). The voltage settings were calculated via linear regression by the simple formula $U_i = U_1 - E_z \cdot d_z$.

The ROC wire geometry, especially the non-zero distance between the gate wires, can not perfectly screen the high voltage applied to the multiplication wires. This effect was taken into account by simulating the ROC wires and adjusting the gate wire voltage accordingly. Within this simulation it was found, that changes due to high or medium gain (voltage) settings do not affect the global drift field homogeneity. The final results are given in table 2.1.

Table 2.1: OPTIMIZED GATE, SKIRT AND COVER VOLTAGE SETTINGS.

	A side		C side	
	gate wires	skirt & cover	gate wires	skirt & cover
distance d_z [cm]	0.725	0.425	0.698	0.398
Voltage setting U_i [V]	-52.9	-173.0	-63.7	-183.8
Optimized Volt. sett. $U_{opt,i}$ [V]	-61.8	-173.0	-73.6	-183.8

2.3.3 Simulation of misalignment and distortions

First considerations regarding possible chamber misalignments and their influence in terms of radial distortions were performed in [37]. In there, an analytical approach was used to calculate the resulting drift field imperfections. However, this method does not allow to calculate other field imperfections due to ROC geometry, skirt structure or the skipped last strip close to the CE. Thus, a more detailed Finite Element approach is presented in the following paragraphs.

ANSYS model description

The TPC FC was modeled with the Finite Element software package ANSYS [38]. Details regarding FC strip structure, read-out chambers, covers and skirt planes are included. Geometrical as well as material details were taken from [18] and [22]. The potential degrader system along the FC strips is implemented according to the formulas given in the previous section.

Other parameters like adjustable voltages for the cover and skirt potential as well as the gating grid potential at the ROCs are free parameters, as are possible translations and rotational misalignments of every element. Rotational symmetry along the z-axis was used in order to minimize the computational time. The element used is *Plane121*, which is a two-dimensional, eight-node electrostatic element. The element has one degree of freedom, the voltage, at each node. These 8-node elements have compatible voltage shapes and are well suited for two-dimensional electrostatic field analysis.

Figure 2.13 displays the rotational symmetric model with its “smart” mesh. A close-up at the outer FC is also shown together with the corresponding solution for a TPC ideally designed in every aspect.

Garfield [39] provides the input functionality of solved electric field configurations in form of field maps. These can be used as background fields within the drift section of Garfield. The accuracy of the field calculations is highly dependent on the mesh size used within the ANSYS model. A smart meshing of “*smrt-3*” was found to be reasonable in terms of computing time and needed precision. The achieved accuracy is better than 5×10^{-2} V/cm, as is shown in figure 2.14, which is more than sufficient for our studies.

Electron trajectory distortions due to electric field imperfections can be simulated by means of calculating the corresponding offsets of drifting electrons. Furthermore, the study includes an E field dependent drift velocity which allows us to make accurate predictions even for the z (time) coordinate. The following paragraphs provide further details and different case studies. The validation of the model was done by cross checking the results of a simple case study presented in [37]. The results showed excellent agreement

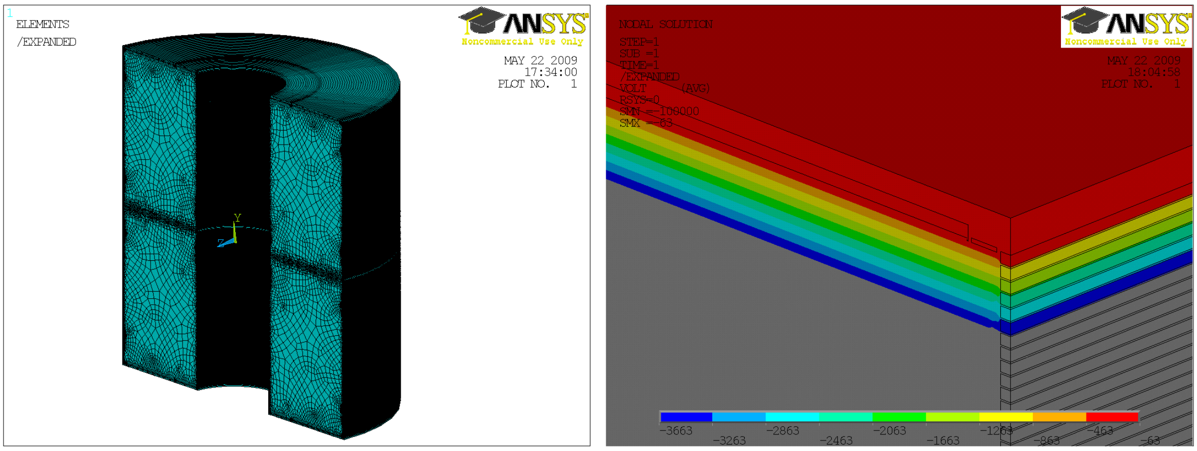
ELEMENTS
/EXPANDED
ANSYS
Noncommercial Use Only
MAY 22 2009
17:34:00
PLOT NO. 1
NODAL SOLUTION
STEP=1
SUB =1
TIME=1
/EXPANDED
VOLT (AVG)
RSYS=0
SMN =-106000
SMX =-63
ANSYS
Noncommercial Use Only
MAY 22 2009
18:04:56
PLOT NO. 1
-3663
-3263
-2863
-2463
-2063
-1663
-1263
-863
-463
-63

Figure 2.13: ANSYS MODEL PLOTS. *Left*: Meshed rotational symmetric model of the TPC field cage. *Right*: Solution with detailed view close to the outer field cage.

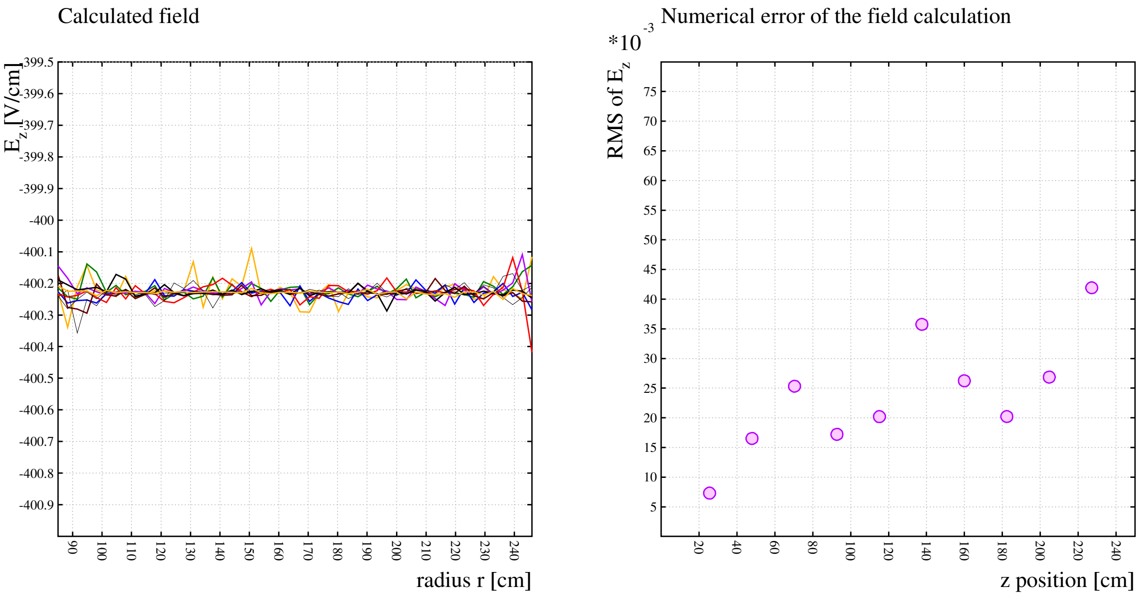

Figure 2.14: ANSYS MODEL ACCURACY. *Left*: Field samples at different (r, z) positions for an ideal field cage configuration with a standard drift field of E_z=-400.23 V/cm. *Right*: RMS values of the field samples along r for different z positions.

for the study of radial distortions due to a voltage offset on the read-out chambers.

Distortions due to the field cage design

An ideal field cage design would consist of infinitely small strips with an anode and cathode directly attached without any space in between. In reality, the finite size of the strips introduces field distortions as discussed in section 2.3. The consequences on the offsets of the drifting electrons are rather small, thanks to the careful design.

Close to the outer field cage, essentially no distortions are visible within the sensitive area of the read-out chambers. This was achieved firstly, due to the distance of about

6 cm from the ROC edge to the outer field and secondly due to the additional skirt strip in the opening between these elements (see figure 2.12).

On the other hand, close to the inner field cage, minimal radial distortions up to a magnitude of 300 μm are visible within the first pads of the read-out chambers. However, these radial distortions are just visible for long drift lengths close to 250 cm and are going to be superimposed with the cluster-edge-effect. Therefore, these edge pads will not be used for the reconstruction of a cluster.

An even smaller effect in terms of radial distortions can be attributed to the missing last strips close to the central electrode, which were not inserted because of technical reasons.

According to the simulations however, the discussed field cage imperfections resulting from the design are negligible due to the fact, that the location of radial and longitudinal (time-bin) distortions is so close to the dead regions of the TPC. In contrast, distortions due to field cage misalignments have an influence on the whole drift field. Therefore these are not to be ignored, as discussed in the subsequent paragraphs.

Distortions due to misaligned ROCs

Due to special considerations in the construction phase of the field cage, the field cage strips are positioned with a precision of ≤ 50 μm. In addition, the alignment of the central electrode and the read-out chambers must be better than 100 μm. This was considered to be one of the most challenging parts in the TPC commissioning phase on the surface in 2006. However, in winter 2006, the completely assembled TPC was lowered into the cavern (P2). Resulting mechanical deformations due to the installation procedure could not be excluded.

The laser calibration system will be the major tool to measure the global alignment parameters of the central electrode and the read-out chambers. But at first, the influence of different misalignment scenarios had to be understood in terms of radial and longitudinal distortions. Therefore, field maps with various misalignment studies were created with the ANSYS model described previously. After importing them into Garfield, distortions of the electron paths could be simulated.

Shift of the read-out chambers A shift of the read-out chambers in the z direction would lead to the same result, as if the voltage setting would have a mismatch with the potential lines due to the field cage strips (40 V correspond to 1 mm shift). Radial distortions in dependence of the drift length of the electrons are shown for two different shift distances in figure 2.15. For a 0.5 mm shift, the electric field is distorted up to approximately 100 cm into the drift volume. The drifting electrons experience radial distortions up to 1 mm when close to the inner or outer field cage. When the shift is towards the drift volume, the electron trajectories are distorted in direction of the field cage. Equivalent results as shown in figure 2.15 were presented in [37], which proves the validity of the method.

In figure 2.16, the radial as well as the longitudinal (time-bin) distortions are plotted for a full drift length of 250 cm, which corresponds to central electrode data. Compared to an ideally homogeneous electric field, a shift of 0.5 mm into the drift volume would cause a systematic error in the z coordinate of electrons close to the interaction point. The

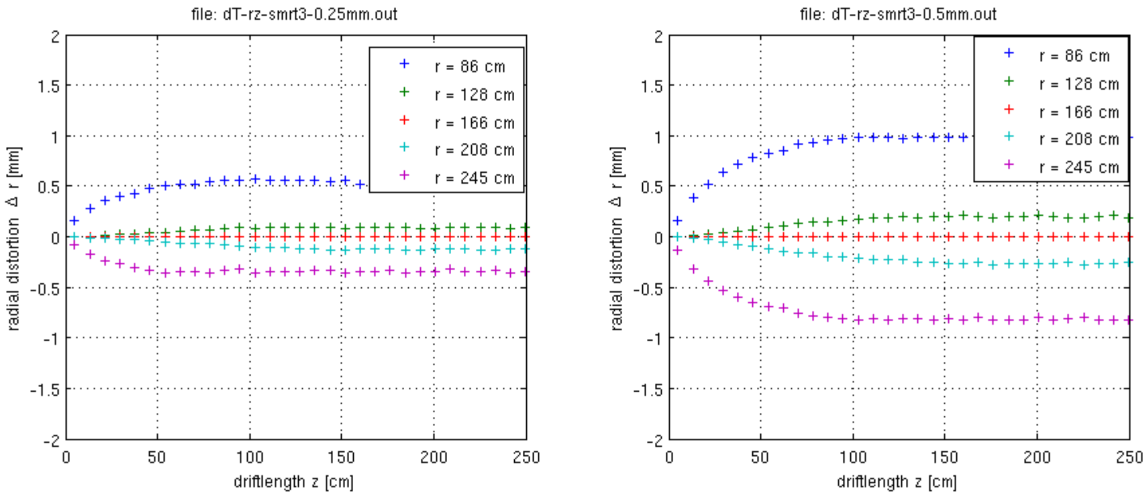

Figure 2.15: Radial distortion versus drift length of the electrons due to mispositioned read-out chambers. *Left*: ROC shift of 0.25 mm into the drift area. *Right*: ROC shift of 0.5 mm into the drift area.

magnitude of these systematic longitudinal distortions is in the range of 0.35 time-bins, or ≈0.9 mm respectively. This is the combined effect of the earlier arrival of the electrons in z (due to the shift) plus the slightly increased drift velocity due the squeezed electric field in the last 100 cm close to the read-out chamber.

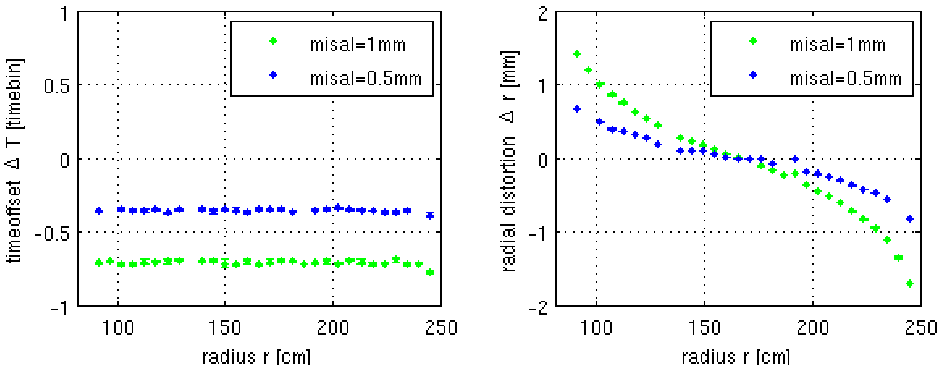

Figure 2.16: Distortions versus radial position of electrons due to mispositioned read-out chambers for a drift length of 250 cm. *Left*: time offsets, where 1 time-bin equals 0.1 μs. *Right*: radial distortions.

Angular misalignment of the read-out chambers The read-out chambers may not only be shifted, but also rotated. An angular misalignment could occur as, for example, a shift of the central barrel in the z direction or by an angular mismatch between the inner and outer ROCs. In figure 2.17, the resulting distortions due to an angular mismatch are plotted, again for electrons which drift through one full TPC half (drift length of 250 cm). For these calculations, the passage between inner and outer ROCs was shifted towards the drift volume. The systematic longitudinal (z) distortions reveal the nature of the angular misalignment, whereas the maximum, for the case of 1.0 mm shift, is found to be 0.7 time-bins, or ≈1.8 mm respectively.

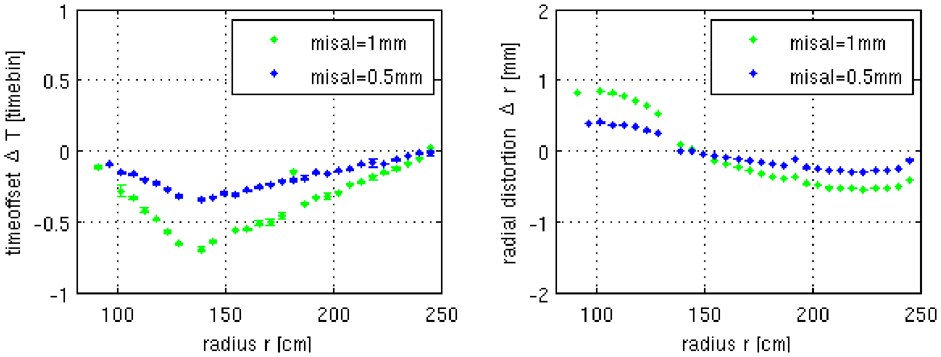

Figure 2.17: DISTORTIONS VERSUS RADIAL POSITION OF ELECTRONS DUE TO ROTATED READ-OUT CHAMBERS for a drift length of 250 cm. “misal” indicates the shift of the passage between the inner and outer ROCs into the drift volume, which results in a para-angular-misalignment. *Left*: time offsets, where 1 time-bin equals 0.1 μs. *Right*: radial distortions.

General distortion picture Various additional case studies revealed the following general behavior. Tracks, perpendicular to the z axis (such as laser tracks or photo electrons from the central electrode) are a reasonable indicator for angular misalignment studies of the read-out chambers. An important fact is, that one has to include the drift velocity change due to the squeezed electrical field in the region close to the ROCs. That's why misalignment factors can not directly be calculated from the measured time offset. Given the current geometry and the chosen operating conditions, a factor of 1.5 (instead of the usually used drift velocity of 2.5 cm/μs) is a reasonable choice when translating time-bin offsets into misalignment constants.

In case of linear shifts or mismatched voltage settings, perpendicular tracks close to the central electrode will show a systematic time-bin offset, which is linear in r (see figure 2.16). Therefore, the time offset can not be used for a voltage scan due to the lack of information regarding the absolute values of the drift velocity as well as a detailed trigger information. For such studies, either radial distortions of laser tracks for long drift lengths (lasers close to the CE) or time-bin offsets of tracks very close to the read-out chambers are usable.

Shorted strips or broken resistor

A catastrophic case scenario would be a broken 15 MΩ resistor within the voltage degrader system or equally bad, but with the opposite effect, two shorted strips along the field cage walls. These errors would lead to a change of the total resistance along the voltage degrader system (compare equations in subsection 2.3.2) and a nonlinear potential drop at the location of the failure.

Distortions due to a broken resistor at the outer field cage at position z=150 cm are shown in figure 2.18. Longitudinal distortions reach values up to two time-bins, which corresponds to a systematic error of the cluster position in z of ≈5 mm before and after the fault. On the other hand, up to 8 mm of radial distortions close to the broken resistor can be expected.

Such a failure can easily be identified due to the magnitude of the resulting distor-

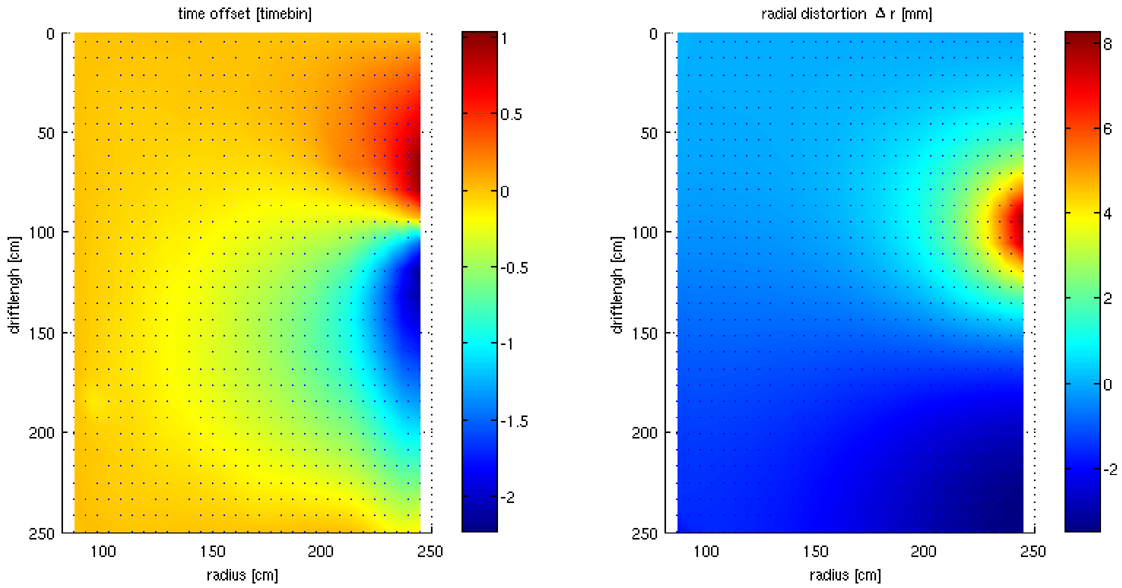

Figure 2.18: Distortion due to a broken resistor at the outer field cage close to position z=150 cm (or 100 cm of drift length) *Left*: time offset map in time-bins, where 1 time-bin equals 0.1 μs. *Right*: radial distortion map in mm.

tions. If such a fault should occur during the life time of the TPC, it must be repaired mechanically. Otherwise, even if corresponding corrections are in place, the design goal of the position resolution will, most likely, not be reached.

Laser measurements

The previously presented considerations and calculations were the base of the development of the laser calibration algorithms. Currently, the global alignment of every single read-out chamber is ongoing by means of matching the partial information of single laser track measurements per read-out chamber. According to preliminary results, the mechanical alignment of the sector quadrants to each other is as good as 150 μm, whereas the angular misalignment of the read-out chamber is on average 0.5 to 1.0 mrad per sector [40].

Furthermore, it is planned to make a voltage scan (gate and skirt voltages) during the commissioning phase in August 2009. This will help to verify the optimal voltage settings as calculated in subsection 2.3.2 by means of minimizing the resulting electron drift distortions.

The results of the laser measurement, as well as of the cosmic-tracks-matching procedure will be summarized in a dedicated chapter in [41].

Chapter 3

Signal shape and read-out optimization

This chapter gives an overview on the creation and the shape of the signals within the ALICE TPC read-out. Furthermore, it contains a shape characterization with special emphasis on the ion-tail typical for Multi Wire Proportional read-out Chambers (MWPC) as used in the ALICE TPC (section 3.1). Various simulations were performed in order to understand the signal shape and the underlying physical and geometric dependencies (section 3.2). The last section in this chapter presents details regarding the digital read-out optimization by means of the ALTRO chip. Furthermore, it hosts the description on how the signal can be shaped and optimized in order to maximize its efficiency for high multiplicity environments.

A detailed description of the ALICE TPC read-out can be found in [20] and [42]. The TPC end plates host the MWPCs with cathode pad read-out. The gas composition used is Ne-CO_2-N_2 (90/10/5) [23]. Two MWPC geometries are present with different distances between the cathode-wire-grid to the anode-wire-grid and to the pad plane, as shown in figure 3.1. The anode wires are made of Au plated W and have a diameter of 20 μm, whereas the cathode and gate wires are made of Cu/Be with a diameter of 75 μm.

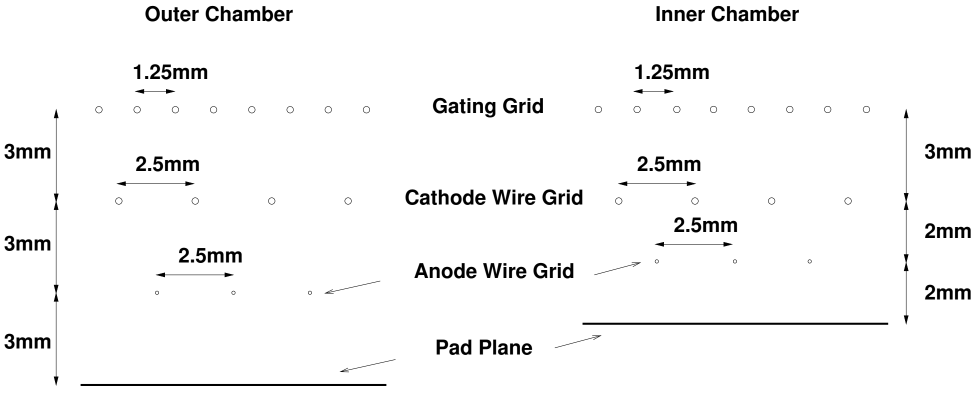

Figure 3.1: Wire geometry of the so called outer (left) and inner (right) read-out chambers, called O-ROC and I-ROC respectively [20].

In general, primary electrons are produced along the path of a charged particle traversing the TPC drift volume. These primary electrons drift towards the MWPC which are situated at the end caps of the TPC cylinder. When reaching the MWPC, an electron multiplication process takes place close to the anode wires. These wires are at a high voltage producing a strong electrical field gradient in their vicinity. This is the place, where the avalanche process amplifies the number of electrons by a few orders of magnitude (gain) by means of producing new electron-ion pairs.

Tracks, their ionization potential in a given gas, the electron drift in the direction of the read-out chambers and the induced signal (on pads or wires) can be simulated using Garfield [39]. An example of electron and ion paths within an I-ROC geometry is plotted in figure 3.2.

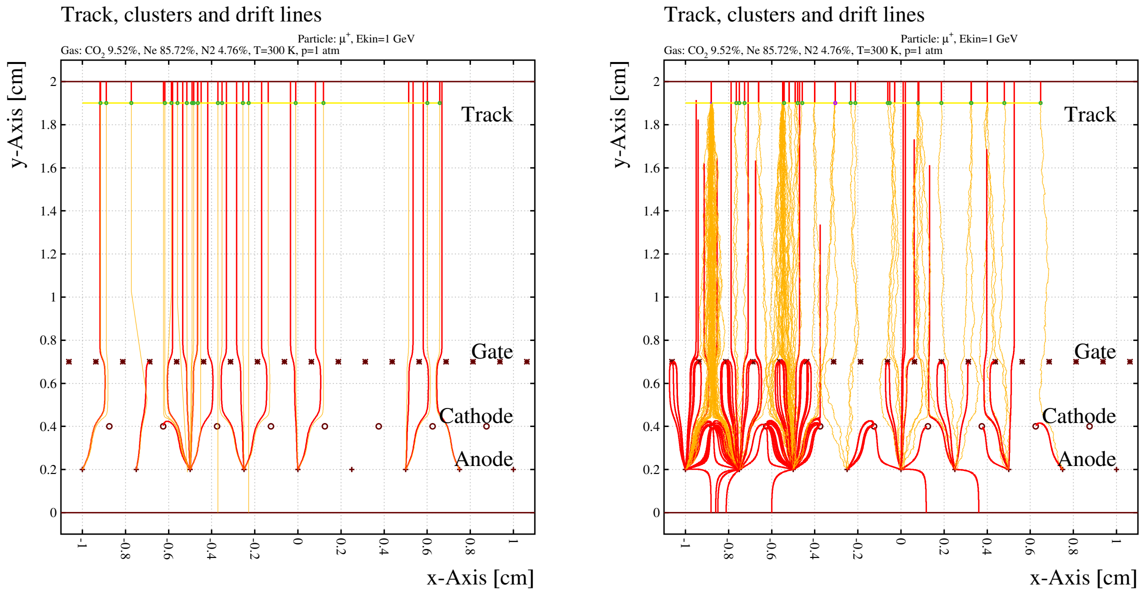

Figure 3.2: Tracks, clusters and electron drift as simulated with Garfield for a TPC I-ROC geometry. Electrons (yellow) drift towards the anode wire, ions (red) drift outwards. *Left:* electrons drift without diffusion. *Right:* electron drift with diffusion (via MC).

The electrons are immediately collected by the anode wire, whereas the positive ions drift in opposite direction. Depending on their angular starting position, they drift towards the pad plane, the cathode wire or even the gate wires. Since the ion mobility is several orders of magnitude smaller than the mobility of the electrons, the signal induced in the pads is characterized by a fast rise in the order of a few *ps* (due to the electrons) and a slow decay in the order of a few μs (due to the slow ions). The so called ion-tail is manifest in form of later peaks (≥ 20 μs) which are usually smaller than 1 % in comparison with the immediate pulse due to electrons. A typical signal as detected on the ALICE TPC read-out is shown in figure 3.3.

The ion-tail of the ALICE TPC read-out was characterized and detailed simulations were performed in order to understand the mechanism behind the shaping. Details regarding both topics are given in the following sections. Section 3.3 contains an analysis on how to minimize the ion-tail characteristics in order to improve the signal quality and the compression factor for high track densities.

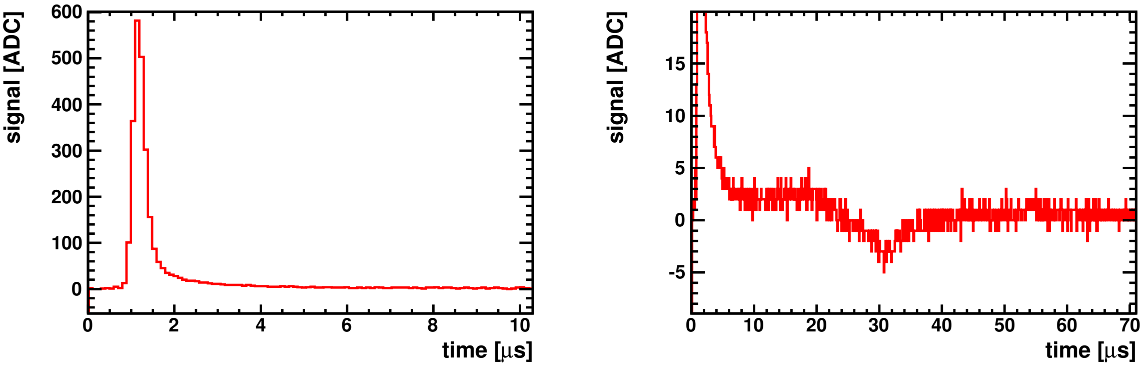

Figure 3.3: Typical pad-signal including the ion-tail. O-ROC signal from a cosmic ray commissioning run in 2006 for an anode voltage setting of 1750 V at (sec,row,pad)=(38,41,83). *Left:* zoom into the time (x) axis to visualize the pulse structure. *Right:* zoom into the signal (y) axis to visualize the typical ion-tail structure.

3.1 Ion-tail characterization and shape variations

Various cosmic muon calibration data were taken during the years 2006 and 2008. The chamber signals were read out at a 10 MHz sampling rate using the ALTRO chip in a mode where the tail cancellation and zero-suppression functionality was disabled (see section 3.3 for further details). According to the sampling rate, 1 digitized time-bin represents 0.1 μs (or 100 ns). For the analysis, pulses with sufficiently low noise and low multiplicity (no pile up) within a certain pulse-height range were selected.

Figure 3.4 contains a 2D-Hit-Graph with zoom into the y-axis. The signals were taken from O-ROC 38 in order to minimize the effect of possible geometrical variations between the different chambers. The pulses were normalized according to their pulse height (100 %) to allow a direct comparison of the tail variations within one sector. The plots reveal an increasing variation close to the end of the first plateau within the ion-tail (at $\approx$ 22 μs). These variations can be attributed to the different signal heights (different size of the incoming clusters), where a more spreaded avalanche can be expected due to the angle of incidence (see section 3.2 for further explanations). An ion-tail characterization in dependence on the pulse height can be found in [43].

During the different test runs, several gas gains (anode voltages) were used, whereas the gate voltage and the gas composition were kept constant in a range of $V_{gate} = 100 \pm 30$ and $\Delta c_{(x)} = \pm 0.5\%$. Some more averaged pulses which correspond to different anode voltage settings are shown in figure 3.5. By averaging more than $\approx$10.000 pulses per voltage setting, the resulting error (RMS) of the averaged signal reaches values lower than the line-width used in the plot. The lowest two voltage settings are an average of only 1000 pulses per sector, and therefore exhibit slightly larger fluctuations. The signal peak was normalized to 100 in order to allow a direct comparison of the different signal shapes, especially of the following ion-tail plateaus and peak heights.

The ion-tail, as presented in figure 3.5, is characterized by a plateau of variable height followed by a negative peak. As the gain (anode voltage) increases, the plateau value increases and the negative peak moves to earlier times. The pulse shapes of the two

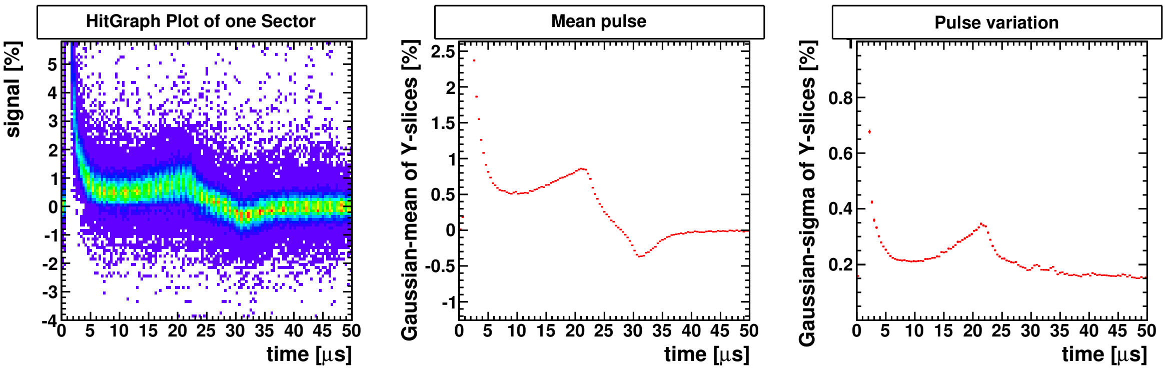

Figure 3.4: VARIATION OF PULSES WITHIN ONE SECTOR (O-ROC-38 at 1750 V) *Left*: Hit-Graph with normalized pulses. *Middle:* mean pulse within sector 38 with RMS smaller then line width. *Right*: Pulse variation by means of σ (of Gaussian-fitted Y-slices).

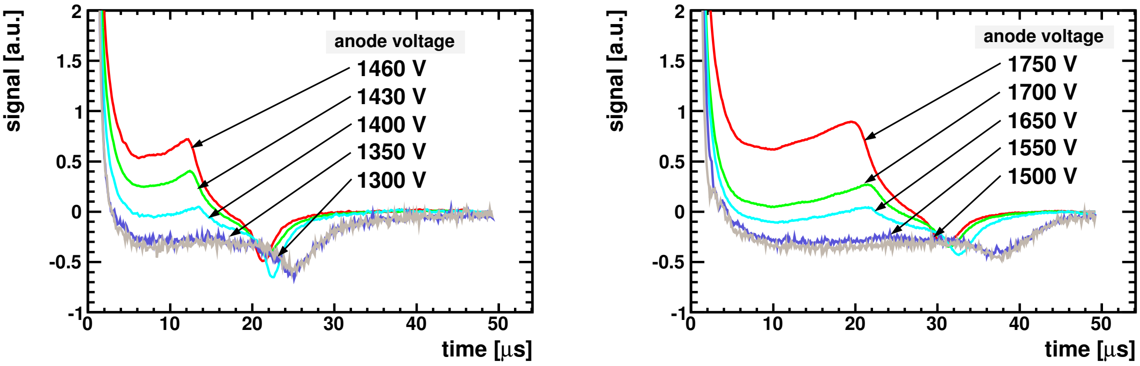

Figure 3.5: MEASURED AVERAGE SIGNALS for several anode voltage (gain) settings. *Left*: I-ROC. *Right*: O-ROC.

chambers show a significant difference in the location of the negative peak, which can be attributed to different gap sizes (see figure 3.1). These pulses are very similar to the ones measured for an inner read-out chamber prototype as presented in [44]. Indeed, the difference mentioned in this reference, which was attributed to the different gas composition, could also be explained by the difference of the anode voltage (gain) settings. Further details can be found in section 3.2.

3.2 Signal shape simulations

The basics of signal creation in MWPCs is well understood and is implemented, for example,in simulation packages like Garfield [39]. This program allows us to simulate the detector response including primary ionization, electron drift, diffusion and the induced signal on different electrodes for the geometry of interest. Detailed models regarding the avalanche process itself and the ions produced in the process (typical ion-tail) are currently in the state of development.

However, various models have been developed and measurements have been performed in the past years [45–47] where mostly the ions, produced in the electron avalanche region were used in order to quantify the avalanche size, the signal and the gain.

In [48] a first attempt was made to explain the variations of the ion-tail characteristics present in the MWPC geometry of the ALICE TPC detector. The present work presents a more detailed approach in order to quantify the influence of different gap sizes and gain (voltage) settings on the signal shape. Several tracks were simulated and the average signals were compared to the measurements as presented in figure 3.5. Figure 3.2 shows an example of a single simulated event. The ‘wiggly’ lines represent the electrons drifting to the anode wires while the smooth lines show ions drifting from the anode wires to the cathode wires, the gate wires and the pads. In this simulation the avalanche is assumed to be very localized, so the ions are starting to drift from the wire surface at the point where the incoming electron arrives. The angular electron-arrival distribution around the anode wire is Gaussian ($\sigma \approx 40°$) and is basically independent of the anode voltage (gain) settings but depends on the chamber geometry [49].

By positioning single ions at different angles around the anode wire, the signal contribution from the different ion drift paths can be obtained as shown in figure 3.6. If the ions reach the pads, the signal is positive. If the ions drift to a cathode wire or a gate wire, the induced signal is negative.

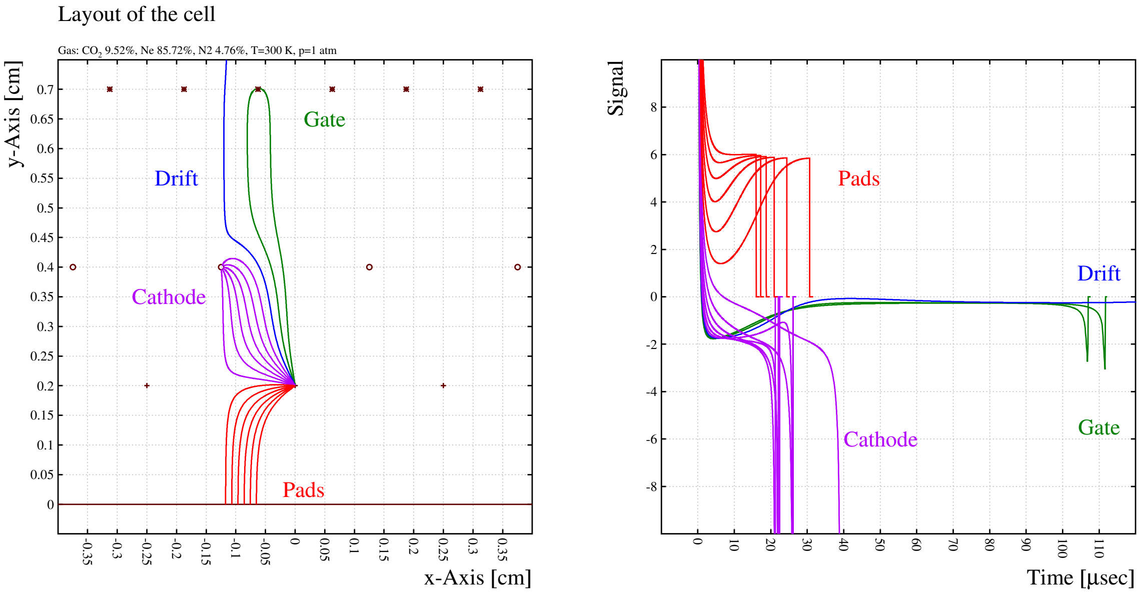

Figure 3.6: Ion tracks (left) and induced signals (right) from single ions of different angular positions to the multiplication wire.

It turns out that for all the different voltage and gain settings, the simulated signal shows an undershoot and the ‘high’ plateau visible in the measured signals is not reproduced. As seen in figure 3.2, if no diffusion is assumed, no ion is able to drift towards the pad plane, therefore no positive plateau can be reached. Even when including the diffusion of the electron, most ions in the simulated event move to the cathode wires. On average, this only causes an undershoot (negative plateau). We, therefore, have to conclude that the spread of the electron-arrival positions at the wire, even due to diffusion, cannot explain the positive plateau seen in the measured signals (see figure 3.5). We must, therefore, assume that the electron avalanche is spreading around the wire. This spread must increase with the gas gain, as is mentioned in [46].

As a first approach we considered different distributions for the avalanche itself. But in order to allow a quantitative comparison between simulated and measured data, the magnitude of other effects as well as the correct ion mobilities had to be considered first.

3.2.1 Signal shape dependencies

In general, CO_2 has a first ionization potential well below that of Ne and has a ionization cross section 5 times higher whereas CO_0 ions have a lower ion mobility. Since this would heavily influence the position of the main peaks, further considerations where required. When computing the partial Townsend coefficients, one finds that the ions are produced in competing amounts at fields near 186 kV/cm, which is the field on the surface of the avalanche wire. For lower fields, especially at the start of the avalanche, CO_0 ionizes more. For higher fields, Ne is the dominant ion [28].

However, since Ne is the dominating gas component ($\approx$ 90 %) within the ALICE TPC, we considered Ne^+ to be the dominating contributor at the present fields, therefore only mobilities for Ne^+ in Ne were taken into consideration. These values can be found in [50, 51]. This choice proved to be valid since the position of the main peaks within the ion-tail could be fairly well reproduced when choosing the pertinent voltage and geometrical settings.

Every single setting which could influence the drift field within the MWPC and therefore the drift path of the ions was carefully evaluated. The influence of geometrical choices, different voltage settings on the anode and gate wires as well as considerations regarding the avalanche size and shape where disentangled. Qualitative changes of the signal shape in dependence on these settings were evaluated by summing over the ions drifting away from the multiplication wire. The number of ions was set to 12.000 which can be calculated in a reasonable time and is sufficiently large to result in a smooth average signal, as is shown below.

Geometrical parameters: As discussed in the introduction of this chapter, the ALICE TPC MWPC basically host two different geometries, where the difference lies within the gap size d_{gap} between the cathode and the gate wires (see figure 3.1). The signal shape in dependence on different gap sizes and on small geometrical fluctuations can be found in figure 3.7.

The main effect when increasing the gap size is, that the time-position of the negative peak increases. The simple reason behind that is in fact the longer drift time due to the bigger distance to the cathode wires. In contrast to the measured mean signals, simulated signal shapes display a strong and significant negative spike. The smearing of these spikes can be attributed to fluctuations of the wire positions, as is shown in figure 3.7. In reality, these fluctuations are assumed to be Gaussian and are in the range of $\sigma_{geom} \approx 50\ \mu$m.

Voltage settings: In general, lowering the anode voltage has a similar effect as an increase of the gap size (compare figure 3.7 and figure 3.8). However, increasing the anode voltages would not only lead to higher gains (multiplication factors of the signals) but also to an earlier start of the avalanche due to the higher fields and therefore an enlarged avalanche spread around the anode wire. But, as seen in figure 3.8, the simple assumption

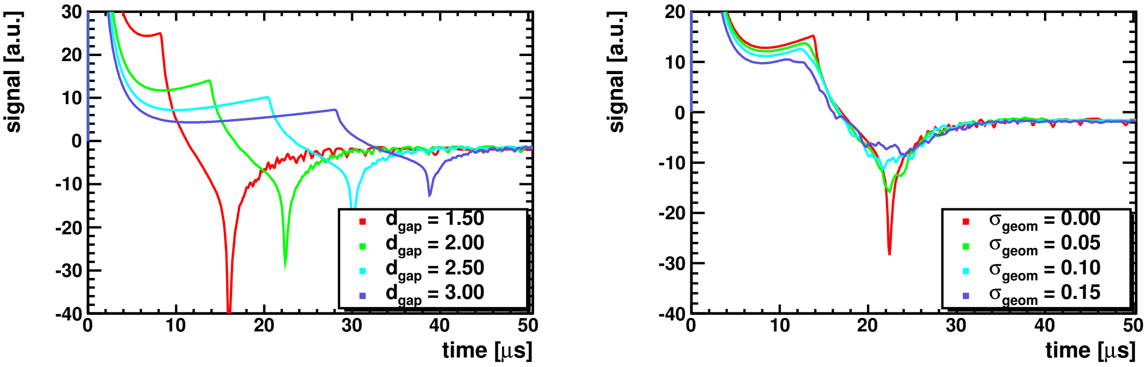

Figure 3.7: SHAPE DEPENDENCE ON GEOMETRICAL PARAMETERS. *Left*: dependence on the gap size d_{gap} between the cathode and gate wire plane (I-ROC is 2 mm gap and O-ROC is 3 mm). *Right:* Dependence on minimal geometrical fluctuations σ_{geom} of the wire positions.

that the corresponding change of the drift field within the chambers can account for the drastic changes in the plateau heights of the measured signal can not be confirmed (see next paragraph for further details).

A possible change of the gate voltage settings does have an insignificant impact on the electric field and therefore the ion-tail characteristics. A diminution down to -300 V has almost no impact on neither the plateau height nor the negative peak position.

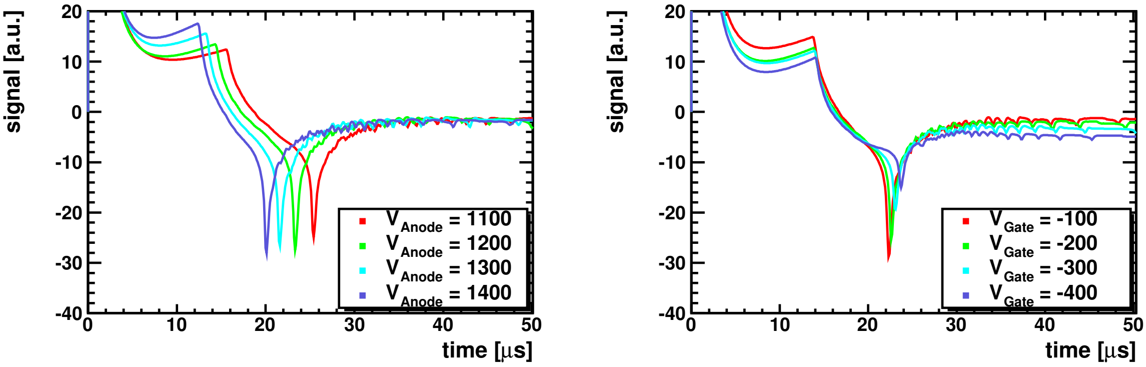

Figure 3.8: SHAPE DEPENDENCY ON VOLTAGE SETTINGS for an I-ROC geometry. *Left*: different anode voltage (gain) settings. *Right*: different gate voltage settings.

Avalanche spread: Changes of the avalanche distribution (e.g. increasing σ) around the wire do not change the time positions of the significant negative peaks but do change the height of the first plateau. This means, if the avalanche size reaches the lower half of the anode wire, ions start to travel towards the pad plane which results in a higher positive plateau within the first part of the ion-tail. Different avalanche distributions do not essentially influence the signal shapes itself, but are different in terms of the numerical value σ describing the avalanche spread. This can be seen in figure 3.9. It is generally accepted to assume a Gaussian avalanche distribution, even if it does not fully account for the avalanche shape itself, but it is easier to compare the values found with previous studies.

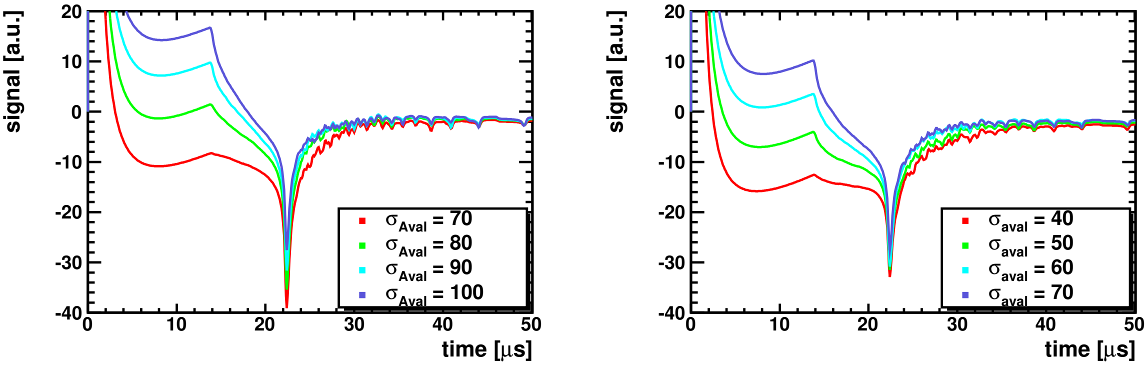

Figure 3.9: SHAPE DEPENDENCY ON THE MULTIPLICATION AVALANCHE for an I-ROC geometry. *Left*: Gaussian distribution. *Right*: Laplace distribution.

3.2.2 Determination of the avalanche spread

Since all but one of the above mentioned parameters are fixed through the experimental setup, the size of the avalanche represented by the sigma of the Gaussian can be adjusted to give the height of the positive plateau as present in the measured signal shapes. This allows to quantify the size of the avalanche for different anode voltages.

According to this analysis, the avalanche size increases with increasing gain (anode voltage) settings, as one would have expected. Further details and corresponding plots including the size of the determined avalanche spread were published in [49].

In general, it is believed that also the gas composition plays an important role not only for the position of the main peaks but also for the avalanche spread. In [23] the difference in gas gain for a Ne-CO_2 gas mixture, previously used in the ALICE TPC, and the current Ne-CO_2-N_2 gas mixture, is shown. Since within the present model, the gas composition is just represented through the assumption of the dominant ion mobility, further investigations would be needed in order to understand possible additional effects. Including the cross sections, production rates, ionization energies and the Penning effect would lead to a more precise model; however, it is not the subject of the current work.

The systematic time offset of the negative peak (cathode-ions peak) between simulated and measured pulses indicates that especially at the start of the avalanche the assumption that the Ne ions dominate might not be true. This systematic shift starts with 10 % at low gain, but decreases significantly when increasing the gain. Since, according to [52], CO_2 as well as N_2 have a lower ion mobility than Ne, especially in the start region of the avalanche the ratio between Ne^+ and CO_2^+ N_2^+ might not be ignored anymore. However the main characteristics of the ion-tail are reproduced up to a reasonable level.

3.3 ALTRO chip - raw data optimization

A rate of 200 events/s produces a data volume of approximately 150 GByte/s in the ALICE TPC if no data reduction technique or optimization is used. One of the most common data reduction methods is zero-suppression i.e. the suppression of data below a pre-defined threshold. Therefore it is essential to keep the baseline as constant as possible to correctly identify pulses which are above threshold. In environments of large multiplicity, zero-suppression becomes ineffective because of pile up effects caused by the long ion-tail. Therefore, a circuit able to cancel the complex and long ion-tail is a key requirement for the functioning of the ALICE TPC.

To reach these higher challenges of new HEP experiments, a special mixed analogue-digital ship, called ALTRO (ALice Tpc Read-Out) was developed. This specially designed read-out chip is dedicated to the digitization and processing of gaseous detector signals. It contains 16 channels operating concurrently on the analogue signals coming from 16 independent inputs. Upon arrival of a first level trigger, each input signal is sampled, processed and stored in a data memory. A general description including performance statements can be found in [42]. Details regarding the underlying design-algorithms and the customized integrated circuits are available in [53], whereas [54] contains a detailed manual on how to make use of the programmable parts.

A basic overview on how the signal is processed is given in figure 3.10. After the analogue to digital conversion (ADC), the signal processing is done in basically five steps: a first correction and subtraction of the signal baseline, the cancellation of an ion-tail structure, a second baseline correction, the suppression of signals below the noise threshold (zero suppression) and the data formatting. The data processing and the read-out of the data memory are performed at different frequencies (different color in figure 3.10).

The first Baseline Correction and Subtraction (BCS1) can be used to correct for systematic instabilities of the signal baseline caused by e.g. coupling of AC or DC or by

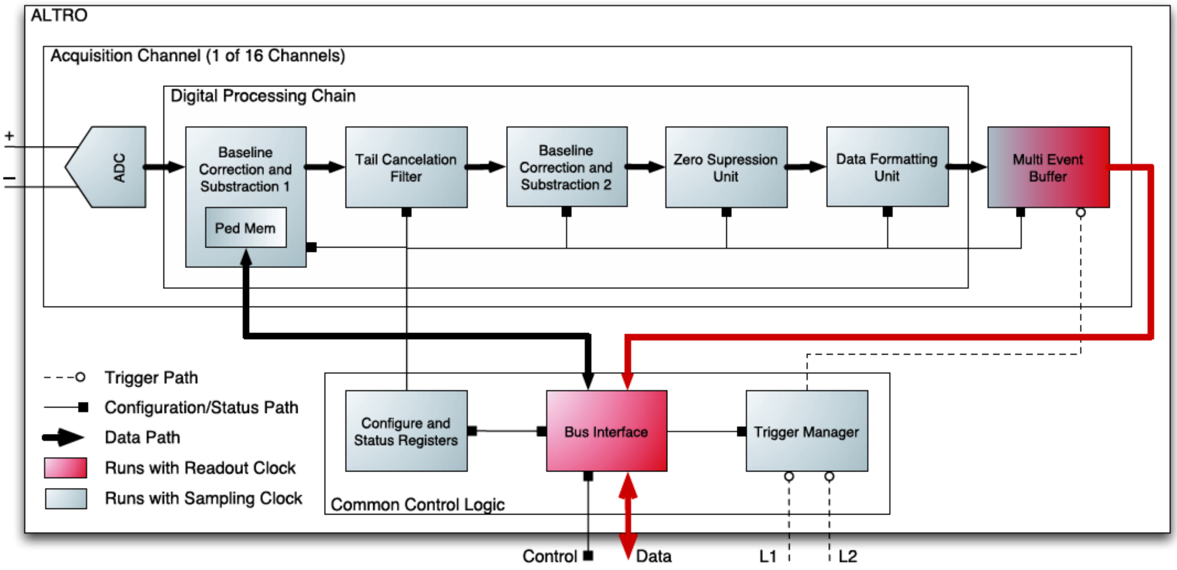
ALTRO
Acquisition Channel (1 of 16 Channels)
Digital Processing Chain
+
−
ADC
Baseline Correction and Substraction 1
Ped Mem
Tail Cancelation Filter
Baseline Correction and Substraction 2
Zero Supression Unit
Data Formatting Unit
Multi Event Buffer
Trigger Path
Configuration/Status Path
Data Path
Runs with Readout Clock
Runs with Sampling Clock
Configure and Status Registers
Bus Interface
Trigger Manager
Common Control Logic
Control
Data
L1
L2

Figure 3.10: Block scheme of the ALTRO chip. Included is the digital processing chain for the signal optimization [43].

switching the gating grid on or off. It allows the subtraction of time-dependent pedestal values taken from the pedestal memory, which are filled by the daily pedestal-calibration runs.

The second stage of the optimization process is the Tail-Cancellation Filter (TCF). As discussed before, the signal of a gas detector often includes the long ion-tail of rather complex shape. In order to perform an efficient zero suppression, these tails have to be canceled as accurately as possible. The built-in TCF is based on the approximation of the tail by a sum of exponentials. Therefore, the TCF consist of three dedicated Pole-Zero (PZ) filters. Flexibility for the 16 different channels is given by the possibility to re-configure the programmable coefficients channel per channel.

After the tail cancellation a second Baseline Correction and Subtraction (BCS2) corrects for non-systematic perturbations of the baseline. It is based on a Moving Average Filter (MAF) which computes the moving average on certain samples of the digitized signal and then subtracts this value. As long as the amplitude of the ion-tail peaks is below a certain threshold, this method partially corrects for the ion-tail as well. But when it comes to high track densities one finds that only the TCF can provide a certain baseline stability since the MAF becomes less efficient if the pulses are not well separated.

Further details regarding the ALICE read-out and the different stages of the ALTRO chip can be found in [43, p.17] and the ALTRO manual [54]. The following subsection focuses on the underlying algorithms to find the optimal parameters of the TCF stage.

3.3.1 Tail-Cancellation Filter

The long signal tail (as shown in figure 3.5) together with a high occupancy environment creates pile up effects that hamper the efficiency of the zero-suppression. In order to minimize these effects and to maximize the compression efficiency, a suitable filter is needed.

Within the ALTRO chip, the TCF was implemented by placing three first order IIR circuits in cascade [53]. Each stage of the filter is controlled by means of two coefficients (a_i and b_i), that can be programmed independently for each of the 16 channels. The TCF can be enabled or disabled via a global register. Once it is activated, the incoming pulse is shaped according to the programmed coefficients. The filter implementation corresponds to the transfer function in the Laplace-domain depicted in equation 3.1.

$$H(s) = \frac{s+a_1}{s+b_1} \cdot \frac{s+a_2}{s+b_2} \cdot \frac{s+a_3}{s+b_3}. \tag{3.1}$$

The computation of the six coefficients can be done via analyzing real non-zero suppressed reference pulses, as for example data from cosmic runs. When the ion-tail structure is identified, one of the methods described below can be used in order to find the optimal TCF parameters.

In general, the signal is convoluted with the Impulse Response function (IRF) of the pre-amplifier and the shaper within the electronics. Therefore the input signal of the TCF $d(t)$ can be written as

$$d(t) = I(t) * P(t).$$

Where $I(t)$ and $P(t)$ are respectively the impulse responses of the tail and the amplifier mechanisms.

Obtaining the TCF coefficients via a recursive approach

An approximation for the signal $d(t)$ as a set of real functions $f(nt)$ on a time-discrete scale was proposed by [53, chap.4]. This function can be:

$$f(nt) = \begin{cases} e^{-bnt} \cdot [1 - e^{(b-a)}] & \text{if } n > 0, \\ 1 & \text{if } n = 0. \end{cases} \tag{3.2}$$

with its corresponding Laplace-transform:

$$F(s) = \frac{s+a}{s+b} \; . \tag{3.3}$$

This corresponds to a typical PZ filter transfer function in the s space. A discrete response $u(nT)$ to the correction system $h(nT)$ (e.g. a single PZ filter) can be written as a convolution term:

$$u(n) = \sum_{n_0=0}^{+\infty} d(n - n_0) \cdot h(n_0). \tag{3.4}$$

As is shown in [53, chap.4], when choosing the Z-domain instead of the Laplace domain, a recursive expression to approximate the PZ filter parameters a_i and b_i can be found. In this reference, the values are transformed into pairs of *pole* and *zero* (P,Z) values which are related to a and b via

$$(pole, zero) = (P, Z) = (e^{-b}, e^{-a}) \qquad \text{with } Z, P \in [0, 1]. \tag{3.5}$$

Since there are three PZ filters implemented in the ALTRO, this method can be used twice to derive the parameters for the first two PZ filters (first 4 TCF parameter) followed by an amplitude equalization (using a similar formalism) which can be done in the third filter (plus 2 TCF parameters).

The success rate of this recursive method heavily depends on the quality of the reference pulses (input signal). When it fails to compute accurate parameters, it often produces parameters which render the ion-tail even more dominant. Therefore a quality assurance algorithm was developed and presented in [43]. The basic idea behind this algorithm is simply to calculate a high number of different parameters for a corresponding number of varying pulses. By the method of “weighted quality” including parameters like undershot recognition, width difference and amplitude difference, a set of parameters is found which works best for all the different input pulses of the different channels. In this way, badly computed parameters are rejected. Unfortunately this procedure looses the ability to compare pulse variations on a single-channel level.

Obtaining the TCF coefficients via a fitter approach

This kind of technique was first mentioned in [55] (unipolar tail cancellation) and includes the physical interpretation of the pulse-shaper peaking time τ_p as well as the decay-time constants τ_i from the signals which are approximated via exponentials. A detailed representation regarding the derivation of the corresponding fit-function can be found in [17, p.200]. However, a brief overview is given in the following.

In general, a signal arising from a point ionization entering the avalanche region of the proportional counter is fairly well represented by:

$$i(t) = \frac{Q}{2t_0 \ln \frac{b}{a}} \cdot \frac{1}{1 + t/t_0} = I_0 \frac{1}{1 + t/t_0}, \tag{3.6}$$

which can be approximated by a sum of exponential with increasing time constants $\tau_n = t_0/\alpha_n$

$$i(t) \approx I_0 \sum_{n=1}^{N} A_n e^{-\alpha_n t/t_0} = I_o \sum_{n=1}^{N} A_n e^{-t/\tau_n}, \qquad \tau_n < \tau_{n+1}. \tag{3.7}$$

The appropriate Laplace transformation is

$$I(s) = \mathcal{L}[i(t)] = I_0 \sum_{n=1}^{N} \frac{A_n}{s + 1/\tau_n}. \tag{3.8}$$

If a PZ filter with the time constants τ_n and τ of the form

$$H_{PZ}(s) = \frac{s + 1/\tau_n}{s + 1/\tau}, \tag{3.9}$$

is applied to the signal $I(s)$ it cancels the n-th exponential term within the signal. The ALTRO provides three programmable PZ filters, whereas the last filter is commonly used to reestablish the exact signal height. Therefore we choose to approximate our complex signal shape via three exponential terms, where the first one corresponds to the electron signal, which is of course to be kept, and the later two represent the ion-tail structure which is to be canceled. Therefore, a simple fit function would be

$$i(t) = I_0 \frac{1}{1 + t/t_0} \approx I_0 (A_1 e^{-t/\tau_0} + A_2 e^{-t/\tau_2} + A_3 e^{-t/\tau_3}). \tag{3.10}$$

The parameters A_i and $\tau_i = t_0/\alpha_i$ can be found through common minimization procedures (least square fitting) of the original chamber signal or of reference pulses. Rewriting $I(s)$ of equation (3.8) with a common denominator

$$\sum_{i=1}^{3} \frac{A_n}{s + 1/\tau_n} = \frac{as^2 + bs + c}{(s + 1/\tau_1)(s + 1/\tau_2)(s + 1/\tau_3)}. \tag{3.11}$$

with $a = A_1 + A_2 + A_3$, $b = \frac{A_1}{\tau_2} + \frac{A_1}{\tau_3} + \frac{A_2}{\tau_1} + \frac{A_2}{\tau_3} + \frac{A_3}{\tau_1} + \frac{A_3}{\tau_1}$, $c = \frac{A_1}{\tau_2 \tau_3} + \frac{A_2}{\tau_1 \tau_3} + \frac{A_3}{\tau_2 \tau_2}$, and writing the polynomial in the numerator in the form

$$as^2 + bs + c = a(s + 1/\tau_a)(s + 1/\tau_b),$$

with $-1/\tau_a$ and $-1/\tau_b$ as the roots of the polynomials, gives the final form of the signal in the Laplace domain

$$I(s) = I_0 \frac{a}{(s + 1/\tau_1)} \frac{(s + 1/\tau_a)}{(s + 1/\tau_2)} \frac{(s + 1/\tau_b)}{(s + 1/\tau_3)}. \tag{3.12}$$

By applying two PZ filters with the time constants τ_2, τ_a and τ_3, τ_b found through the minimization procedure, we transform the signal into a single exponential, which is the signal coming from the electrons only.

$$I_e(s) = I(s) \cdot \frac{(s + 1/\tau_2)}{(s + 1/\tau_a)} \frac{(s + 1/\tau_3)}{(s + 1/\tau_b)} = I_0 \frac{a}{s + 1/\tau_1}. \tag{3.13}$$

This is rewritten in the time domain

$$i_e(t) = I_0(A_1 + A_2 + A_3)e^{-t/\tau_1}. \tag{3.14}$$

At this point it is rather clear how to translate the parameters found from the **recursive approach** into the fitted parameters from the **fitter approach** and vice versa.

$$P_1 \doteq e^{-1/\tau_a} \qquad P_2 \doteq e^{-1/\tau_b} \qquad Z_1 \doteq e^{-1/\tau_2} \qquad Z_2 \doteq e^{-1/\tau_3}. \tag{3.15}$$

Although the τ_n values would represent a more intuitive format since they are the time constants of the different exponential terms, it is more convenient to use the (P,Z) pairs in view of the numerical handling. After the parameters for the first two PZ filters have been found, the parameters (P_3, Z_3) for the third PZ filter can be used to reestablish the correct height of the pulse as is shown in [53]. Furthermore, since the ALTRO chip can only be programmed with sixteen digits (2^{16} values), the (P,Z)∈[0,1] pairs have to be translated into the corresponding ALTRO format via the simple relation

$$\big(K_i, L_i\big) = \big(P_i \cdot (2^{16} - 1), Z_i \cdot (2^{16} - 1)\big). \tag{3.16}$$

A more efficient approximation to the chamber signal can be made by convolving the exponential terms (approximation of the chamber signal) with the Impulse Response function (IRF) of the electronic circuits. For example, a normalized Gamma function of the order n is equal to the transfer function of an unipolar shaper.

$$h_{uni}(t) = \left(\frac{t}{t_p}\right)^n e^{n\left(1-\frac{t}{t_p}\right)}, \qquad H_{uni}(s) = \frac{t_p e^n n!}{(n + s\ t_p)^{n+1}}, \tag{3.17}$$

wherein t_p is the peaking time of the electronics. This value is usually optimized according to the needs of the signal which has to be measured. However, the signal which is seen by the TCF is then

$$u(t) = \mathcal{L}^{-1}\left[H_{uni} \cdot I_0 \sum_{m=1}^{N} \frac{A_m}{s + 1/\tau_m}\right]. \tag{3.18}$$

An analytic representation of $u(t)$ can be expressed by making use of the relation

$$\mathcal{L}^{-1}\left[H_{uni}(s)\cdot\frac{A}{s+1/\tau}\right]=\mathcal{L}^{-1}\left[\frac{t_p e^n n!}{(n+s\,t_p)^{n+1}}\cdot\frac{A}{(s+1/\tau)}\right]=A\cdot f(t,\tau), \tag{3.19}$$

$$\text{with}\quad f(t,\tau)=t_p n! e^n\left(n-\frac{t_p}{\tau}\right)^{-(n+1)}\left(e^{-t/\tau}-e^{-nt/t_p}\sum_{m=0}^{n}\frac{1}{m!}\left[\left(n-\frac{t_p}{\tau}\right)\frac{t}{t_p}\right]^m\right).$$

In case of three exponential terms a fit function including the IRF of the electronic shaper can be expressed as

$$g(t)=A_1\cdot f(t,\tau_1)+A_2\cdot f(t,\tau_2)+A_3\cdot f(t,\tau_3). \tag{3.20}$$

The IRF was found to be represented with sufficient accuracy through a gamma function of the fourth order ($n=4$) with a peaking time t_p of 0.22 μs. These numbers were found by means of analyzing the pertinent pulser-calibration runs. The inclusion of these values into the fit function (3.20) allows to determine finally the fit parameters A_n and τ_n by means of a simple *TMinuit* minimization procedure (see [56]). The so found fit values can then be used to determine the corresponding PZ filter parameters as it was stated above.

Applying the found TCF coefficients

An example fit is given in figure 3.11, where a typical pulse from the outer read-out chamber (O-ROC) was fitted. The found fit parameter, already translated into time coefficient of the corresponding first two PZ filters, are:

$$\begin{aligned}1^{st}\text{ PZ filter:}\quad &(\tau_a,\tau_2)=(1.02,1.27)\ \mu s,\\ 2^{nd}\text{ PZ filter:}\quad &(\tau_b,\tau_3)=(21.77,29.38)\ \mu s.\end{aligned}$$

The corresponding response of, for example, the first PZ filter can be calculated using the analytical expression of the convolution of the input signal $v(t)$ with the delta response of the PZ filter

$$u(t)=\int_0^t w_{PZ}(t-t')v(t')dt'=v(t)-\int_0^t e^{-(t-t')/\tau_a}\,v(t')\,dt', \tag{3.21}$$

$$\text{with}\quad w_{PZ}=\mathcal{L}^{-1}[W_{PZ}(s)]=\delta(t)-\frac{\tau_2-\tau_a}{\tau_2\tau_a}e^{-t/\tau_a},$$

or by using the recursive formula within the discrete time-space as given in [53, p84]. After calculating the response of the first two stages, the height normalization can be performed. The resulting Tail-Cancellation parameters for the pulse as shown in figure 3.11 are then:

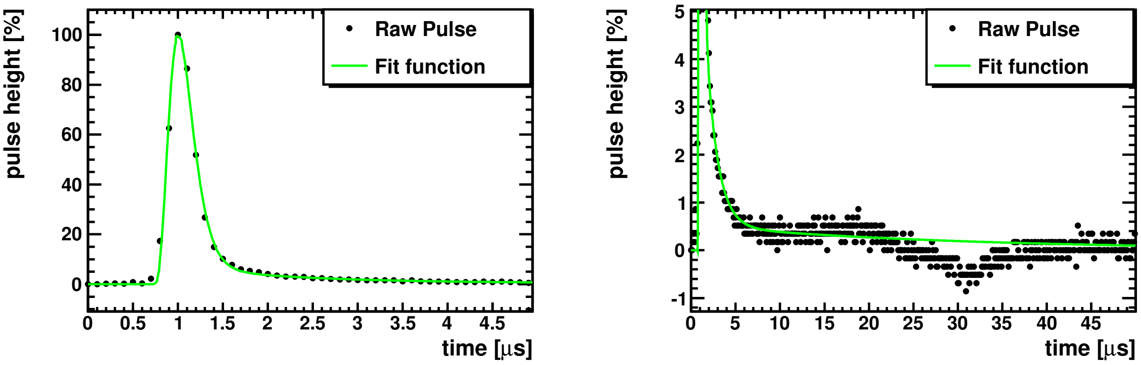

Figure 3.11: FITTED O-ROC SIGNAL at an anode voltage of 1750 V. *Left:* zoom into the time (x) axis. *Right:* zoom into the signal (y) axis.

$$
\begin{aligned}
1^{st}\text{ PZ filter:}\qquad & (P_1, Z_1) = (0.907038, 0.924218),\\
2^{nd}\text{ PZ filter:}\qquad & (P_2, Z_2) = (0.995417, 0.996602),\\
3^{rd}\text{ PZ filter:}\qquad & (P_3, Z_3) = (0.023925, 0).
\end{aligned}
$$

The result of applying the parameters obtained on the input pulse is displayed in figure 3.12. The first stage cancels the immediate ion-tail at the falling edge of the pulse and therefore shortens the signal width. This results in a higher robustness against immediate pile up effects in high occupancy environments. The second stage restores the baseline within the first twenty microseconds, thus raising the efficiency of the following zero suppression.

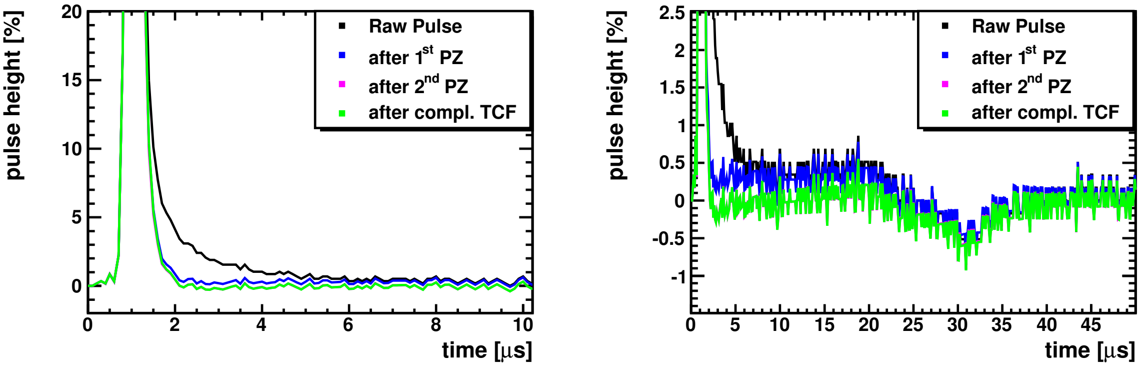

Figure 3.12: TAIL-CANCELLATION STAGES on a O-ROC signal at an anode voltage of 1750 V. *Left:* zoom into the time (x) axis. *Right:* zoom into the signal (y) axis.

The negative peak at around 30 μs after the pulse could not be canceled due to the limitation of the provided PZ filter functionality. It was tried to use a 4-term exponential function within formula (3.20) including a negative amplitude $-A_4$ to correct for the late peak. But this fit turned out not to be feasible due to the noise level of the available data and the average size of the peak ($\leq$ 0.5 % of the pulse height). Besides that, an exponential term with negative amplitude and a large time coeffizient always engages the earlier exponential and is therefore unstable and unrealiable within an automatized procedure.

The fitting approach is much more stable if the noise level is kept below a reasonable height. Due to this stability, a pad-per-pad comparison regarding main variations of their averaged pulse due to geometrical differences could be performed. Results and quality assurance considerations are discussed in the following subsection.

3.3.2 Analysis and quality assurance

A schematic representation regarding the TCF parameter extraction and the analysis strategy is given in figure 3.13. The extraction of average pulses, the complete fitting procedure and the transformation into ALTRO format was implemented within the AliRoot framework [33] and can be found in the class *AliTPCCalibTCF*. The quality assurance of the obtained parameters and their impact on the signal shape was tested with the implemented ALTRO emulator functionality.

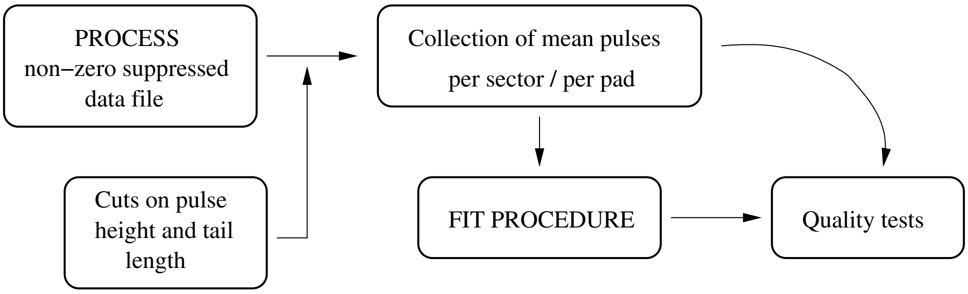

Figure 3.13: Basic block diagram for shaping parameter extraction.

As mentioned before, the ALTRO chip allows to set the TCF parameters independently for every single channel (pad). Therefore, the following question had to be answered. Are geometrical fluctuations between each pad (e.g. wire sag) the dominant factor or are the cluster size and the inclination angle of the primary electrons responsible for the pulse fluctuations as seen in figure 3.4?

It turned out that the same pulse variations (for pulses collected within one sector) were also found when analyzing pulses collected from a single pad. Therefore, the cluster size (charge) as well as the electron-anode inclination angle (for smaller clusters) make the biggest impact. Varying ion-tail heights in dependence of the cluster charge (pulse height) were already presented in [43]. The following analysis shows, that in comparison with this effect, geometrical and electronics fluctuations of the ion-tail structure on a channel-per-channel level are negligible.

Non-Zero-Suppressed (non-ZS) data were taken during the commissioning phase in autumn 2006. These data were taken at different gain settings. Averaged mean pulses for I-ROCs and O-ROC geometries were already presented in section 3.1. Figure 3.14 displays collected pulses as initiated by cosmic tracks passing through the magnetic field within the TPC. By collecting a statistic of several million events, mean pulses per pad could be established.

Only pulses which fulfilled the following criteria were considered to calculate a representative mean pulse. Their overall noise level was lower than 1 ADC. They provided

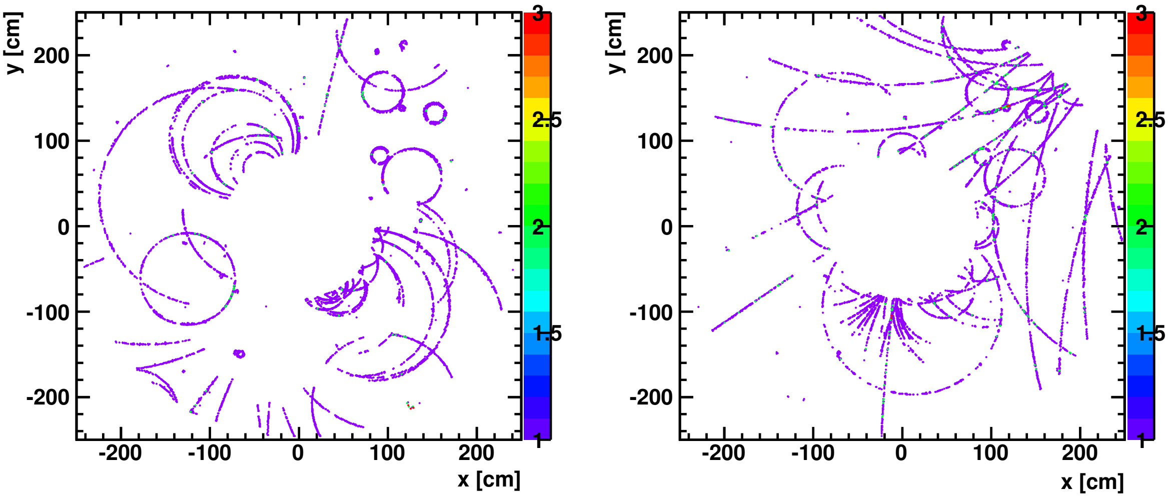

Figure 3.14: Superposition of cosmic tracks and cluster positions as collected over three events triggered by ACORDE. *Left:* TPC A side (positive z axis) *Right:* TPC C side (negative z axis).

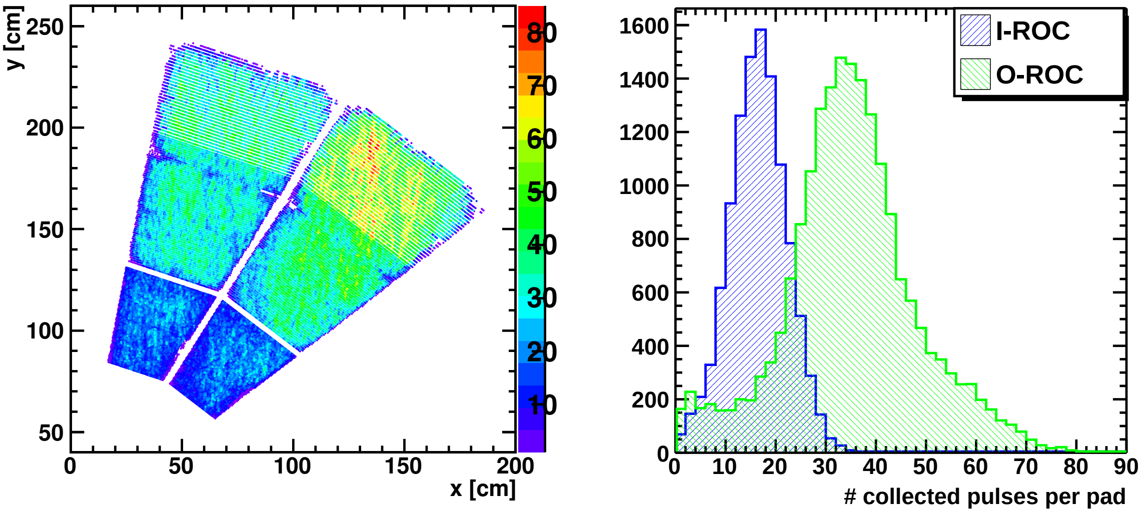

Figure 3.15: Number of collected pulses per pad within the sectors (2,3,38,39) from run number: 2601 (from the year 2006). *Left:* collected pulses per pad versus (x,y) position. *Right:* pad occupancy distribution.

a tail long enough to be suitable for the analysis ($\geq 50\ \mu$s). They did not contain any piled-up signals along their tail. And, their pulse height was at least 30 ADC in order to minimize the remaining noise effect.

The number of collected pulses per pad versus their (x,y) position within the I-ROC sectors (2,3) and the O-ROC sectors (38,39) are shown in figure 3.15. The statistics shown refers to approximately one million summed events triggered by ACORDE, which is placed on the top of the ALICE experiment. The edges of the chambers show significantly less collected pulses due to the fact, that their noise level was higher. The mean number of collected pulses per pad differs between the I-ROC and O-ROC. This is simply due to the smaller pad size within the I-ROCs, while the mean occupancy of cosmic tracks is the same.

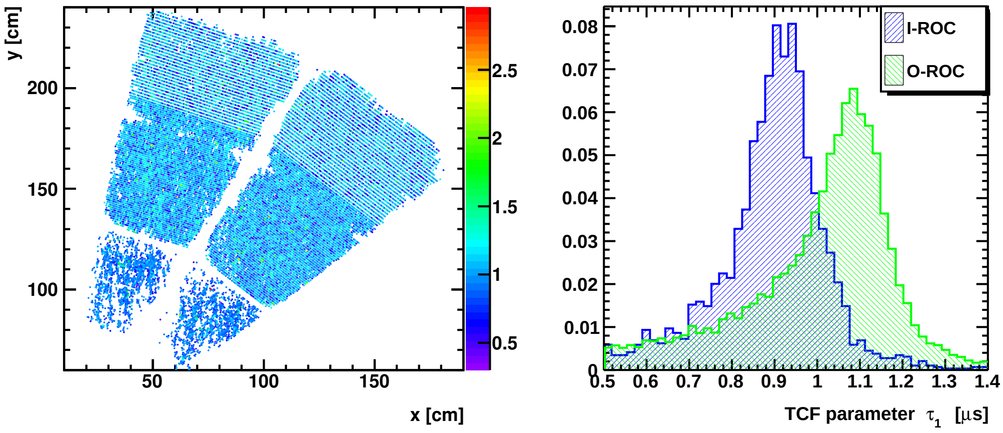

Figure 3.16: TCF PARAMETER τ_1. *Left:* parameter per pad versus (x,y) position. *Right:* normalized parameter distribution.

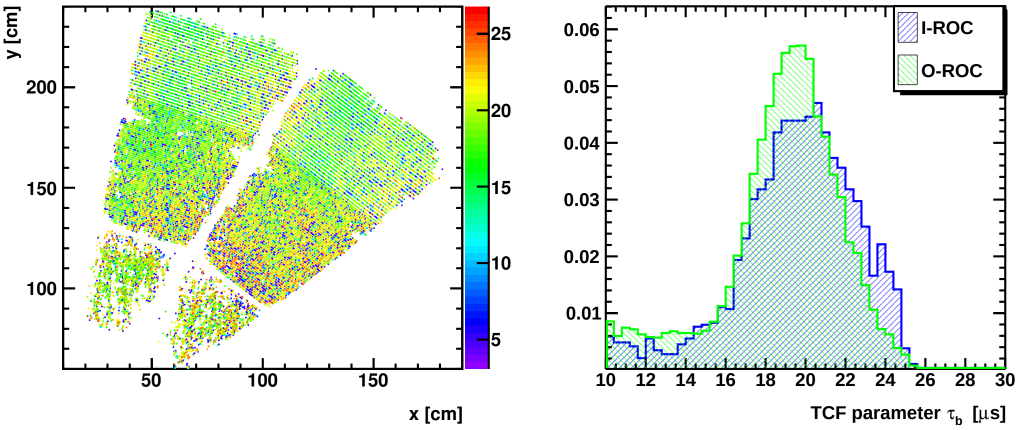

Figure 3.17: TCF PARAMETER τ_b. *Left:* parameter per pad versus (x,y) position. *Right:* normalized parameter distribution.

In the following, the so found mean pulses, which represent an average over ≥ 20 pulses, were fitted and analyzed. Figure 3.16 and 3.17 contain typical plots regarding the regional and quantitative distributions of the parameters found.

In combination with the parameter τ_a, the TCF parameter τ_1 displays the essential behavior of the first PZ filter stage and therefore, the cancellation of the immediate ion-tail. Clear differences are seen between the mean values within the I-ROC and O-ROC geometry due to the different gap size and therefore, due to different weighting fields close to the anode wire. Nevertheless, no regional dependency within one sector was observed.

The TCF parameter τ_b reflects the properties of the second PZ filter stage, which tries to restore the baseline on a later time scale. A high variance regarding this parameter is observed. This can be explained by varying plateau heights due to the lack of high statistics for the pad-pulse average. However, the mean positions are identical due to the gain equalization by means of different voltage settings for the I-ROC and O-ROC (compare section 3.1). When averaging over all pulses per sector, all sector-wise τ_b were lying at the mean presented with a variance smaller than 1 μs.

The observed variances of the found TCF parameters are therefore clearly dominated by the pulse-per-pulse variations and not by possible geometrical (pad) fluctuations, since no regional preferences within the sectors was observed. However, this statement can be proven by applying the found parameters to either averaged or to single pulses. In order to quantify the influence of the applied TCF parameters, the following quality parameters were introduced.

Quality assurance

The main objective of the TCF is to shorten the pulse by means of canceling the immediate ion-tail after the electron signal and to restore the baseline as fast as possible without producing a significant undershot within the first subsequent microseconds. How well these objectives are fulfilled by the shaping parameters can be observed by introducing simple but effective quality parameters, which compare the original pulse with the pulse after the TCF. The monitored parameters are:

- width reduction calculated at a 5 % level of the pulse height;
- maximum and/or mean undershot after the pulse;
- pulse height deviation from the original pulse;
- charge (area) reduction due to ion-tail cancellation.

Within all tests, the pulse height deviation was at maximum ±1 ADC which proves that the algorithm to restore the original pulse height works with almost perfect efficiency. The area reduction depends essentially linearly on the ratio between width reduction and introduced immediate undershot. On average, the baseline reconstruction, when averaged over the following 50 time-bins, works within the expectations.

One set of TCF parameters per sector, when applied on averaged pulses (on the pad level), showed a lower quality performance than the dedicated TCF parameters which were evaluated from the averaged pulses itself. This could lead to the erroneous statement, that programming the parameters individually for every channel would improve the pulse quality. In fact, this improvement is just due to the optimization of the parameters for every single averaged pulse.

Figure 3.18 proves the opposite. One set of parameters determined per sector instead of calculating them pad-wise does not show a quality drop when applied to single raw pulses. The reason is that the dominating effect causing the intrinsic pulse-per-pulse fluctuations of the ion-tail are the cluster size fluctuations and not the pad-per-pad variations. When calculating dedicated TCF parameters for every single raw pulse, the quality of the tail cancellation certainly improves in terms of baseline reconstruction. This also demonstrates that the method of obtaining the parameters is capable of finding the optimal parameters for each individual pulse shape and ion-tail.

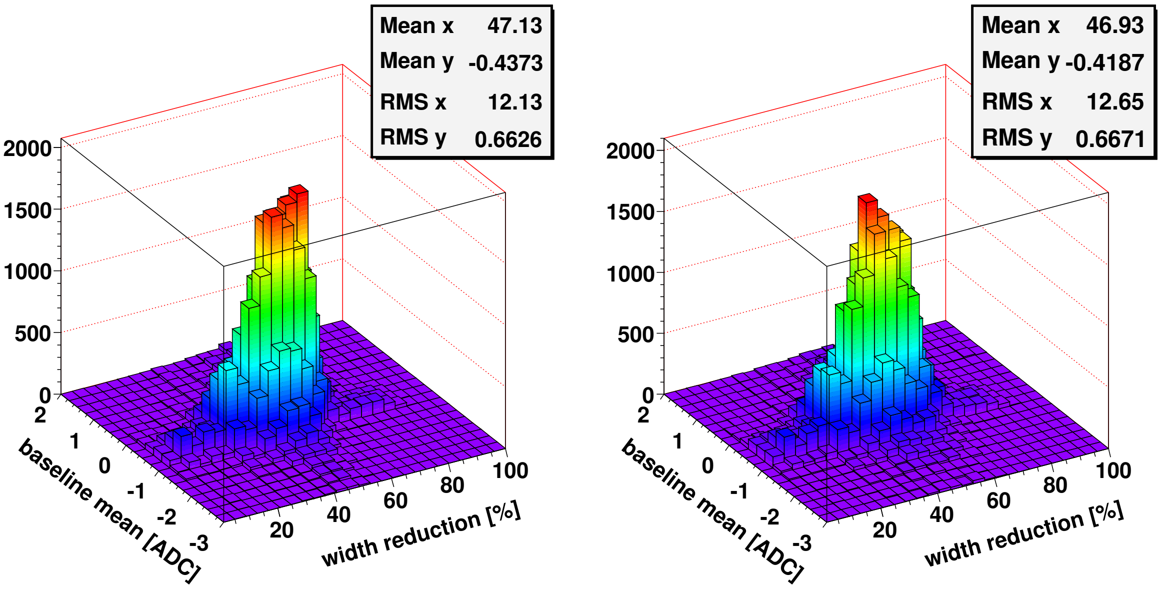

Figure 3.18: Width reduction versus baseline reconstruction for TCF parameters as applied on single pulses. *Left:* one set of parameter per sector *Right:* one set of parameter per pad (channel). No significant differences were observed.

However, since calculating the optimal parameters can not be done within the electronic itself (for each individual pulse), one set for I-ROC and one set for O-ROC geometries is sufficient. One does not need better granularity. It is foreseen to redo the TCF analysis at most once per year. Long time changes due to, for example, aging effects are not expected, but can not be excluded with the data at hand.

Shaping parameters for high and ultra-high gain settings

With increasing gain, the avalanche size around the multiplication wire increases. Therefore, the ratio between the number of ions, which go to the pad, and the number of ions, which go to the cathode, changes. The result is that with increasing gain the region before the first peak becomes positive. Example mean pulses at medium, high and ultra-high gain (commissioning data, 2006 and 2008) are given in figure 3.5.

During the commissioning phase of 2008 non-ZS cosmic data was taken at medium and high gain settings (standard settings for pp collisions). At these gain settings the ion-tail reveals an immediate undershot after the main peak of the signal. Such kind of an undershot can be corrected using a negative amplitude (e.g. $-A_3$) within the fit function. Unfortunately, the fit procedure becomes more sensitive to the quality of the signal since the second (positive) and third (negative) exponential term are in competition. One extreme would be the reconstruction of the baseline without canceling the immediate tail (within the first μs). The other extreme would be to focus on the cancellation of the immediate tail but to accept an immediate undershot in this region. Both effects can be minimized with signal shapes such as for ultra-high gain. However, balancing these effects for high and medium gain settings (signal characterized through an immediate undershot) can not be automatized easily and have to be checked visually. Example mean pulses, before and after the cancellation of the ion-tail, are shown in figure 3.19.

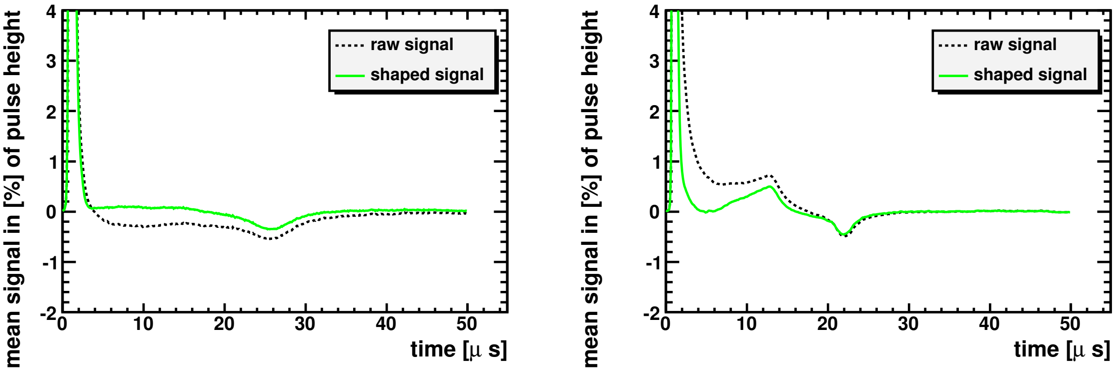

Figure 3.19: Mean ion-tail at high gain and ultra-high gain. *Left:* high gain setting with an I-ROC voltage of 1350 V. The raw pulse contains an immediate undershot after the signal. *Right:* ultra-high gain setting with an I-ROC voltage of 1460 V. The raw pulse has a positive plateau.

Chapter 4

Dynamic effects and distortions

So far, the discussed effects, which influence the magnitude and place of distortions within the TPC, were of static character. Within this chapter, dynamic effects like temperature, pressure and gas composition are considered. The first section contains a parametrization and therefore a disentanglement of the different drift velocity dependencies as simulated with Magboltz [26]. Since temperature stability plays an important role, the second section contains a representation of performed Computational Fluid Dynamics (CFD) simulations. Key case studies and their influence on the temperature distribution within the TPC gas volume are described. The third section presents a direct comparison of drift velocities found via the various sensors (temperature, pressure) in and around the TPC and the drift velocities as evaluated by means of the ITS-TPC track matching.

In general, the calibration strategy regarding the electron drift velocity and its dynamic dependencies includes the following methods:

- matching laser tracks with the surveyed mirror position;
- matching central electrode data with the known position of the central electrode;
- use of cosmic tracks - matching tracks from two halves of the TPC;
- use cosmics or collision data - matching TPC and ITS tracks;
- use the temperature, pressure and gas measurements to predict the drift velocity.

Nevertheless, these methods can not be used to disentangle the different influencing effects like for example, changes in pressure and temperature. Thus, a fast parametrization based on simulated drift velocities was worked out.

4.1 Parametrized drift velocity dependencies

An introduction to drift velocity and diffusion coefficients is given in section 1.3. Anyhow, as shown in the Langevin equation (1.3), the drift velocity v_d is a function of the field (electric, magnetic) and the mobility of the electrons. The mobility depends on the gas density, which is a function of the environment variables (pressure, temperature) as well as the gas composition, which can vary in time.

$$v_d = v_d(E/N) = v_d(E, B, T, P, C_{CO_2}, C_{N_2})$$

wherein E and B are the field values (electric, magnetic), N is the gas density, P is the atmospheric pressure, T is the temperature inside of the TPC and C_{CO_2} and C_{N_2} are concentrations for two out of three components of the drift gas Ne-CO_2-N_2 (90/10/5) within the TPC.

Within the TPC volume, these dependencies are changing with different time constants. A significant change of the drift velocity due to changes of the gas composition has a time constant of days. On the other hand the changes due to the pressure and temperature variation have to be corrected on the level of minutes. Essentially, the field components are, due to the static structure of the field cage, a static variable. They contain regional imperfections which do cause deviations (see section 2.2 and 2.3). Dynamic changes of the electrical field configuration due to space charge clouds are of concern as well. This topic is the subject of the following chapter.

Generally, the state-of-the-art program Magboltz [26] can be used to calculate various drift properties by means of Monte Carlo (MC) methods as for example the drift velocity within a certain gas mixtures, under certain environment conditions and with any chosen field. The claimed relative precision of the drift velocity calculation is 0.05 % which is certainly enough to get a first estimate based on pressure and temperature measurements. Since MC simulations are too time consuming to be used within a calibration code, a parametrization was worked out using simulated data points. Upper and lower tresholds of the dependencies were chosen in a reasonable range of expected variations within the TPC. The limits are given in table 4.1.

Table 4.1: Parameter range of simulated drift velocities where std. cond. is abreviation for "standard conditions"

parameter	std. cond.	MIN	MAX
E [V/cm]	400	395	405
T [K]	293	288	300
P [TORR]	744	719	759
CO_2 [%]	9.52	9.02	10.02
N_2 [%]	4.76	4.36	5.26

Throughout the reasonable range of varying parameters, essentially a linear behavior was observed. Therefore, a first order Taylor approximation in dependence of five variables was used to parametrize the drift velocity for the gas composition of Ne-CO_2-N_2 (90/10/5). The simulated drift velocities were recalculated to fit the relative change of drift velocity in percent (as compared to the absolute drift velocity at standard conditions). The reason is due to the larger absolute error of Magboltz which can introduce an additional systematic shift of the absolute drift velocity. Such a Taylor approximation would be less trustworthy. However, the relative change of drift velocity in percent can, therefore, be written as:

$$\Delta v_d = \Big(\frac{\partial v_d}{\partial E}\Delta E + \frac{\partial v_d}{\partial T}\Delta T + \frac{\partial v_d}{\partial P}\Delta P + \frac{\partial v_d}{\partial C_{CO_2}}\Delta C_{CO_2} + \frac{\partial v_d}{\partial C_{N_2}}\Delta C_{N_2}\Big). \tag{4.1}$$

The absolute scale (drift velocity in cm/μs at standard conditions) is going to be defined with the help of methods as mentioned in the introduction of this chapter. The following dependencies were obtained by means of fitting the simulated v_d's with the first order Taylor expansion as mentioned in equation (4.1). Additionally, a second order Taylor expansion was tried to see if the residuals could be reduced. The according coefficients are given below:

1^{st} order coefficients:

$$\begin{aligned}
\frac{\partial v_d}{\partial E} &= (0.24 \pm 0.02)\ [\%\, cm/V] \\
\frac{\partial v_d}{\partial T} &= (0.31 \pm 0.02)\ [\%/K] \\
\frac{\partial v_d}{\partial P} &= (-0.13 \pm 0.01)\ [\%/Torr] \\
\frac{\partial v_d}{\partial C_{CO_2}} &= (-6.60 \pm 0.29)\ [\%/\%] \\
\frac{\partial v_d}{\partial C_{N_2}} &= (-1.73 \pm 0.23)\ [\%/\%]
\end{aligned}$$

2^{nd} order coefficients:

$$\begin{aligned}
\frac{\partial^2 v_d}{\partial E^2} &= -0.001 \pm 0.009\ [\%\, cm/V] \\
\frac{\partial^2 v_d}{\partial T^2} &= -0.001 \pm 0.006\ [\%/K] \\
\frac{\partial^2 v_d}{\partial P^2} &= -0.001 \pm 0.001\ [\%/Torr] \\
\frac{\partial^2 v_d}{\partial C_{CO_2}^2} &= 0.33 \pm 0.95\ [\%/\%] \\
\frac{\partial^2 v_d}{\partial C_{N_2}^2} &= 0.15 \pm 0.64\ [\%/\%]
\end{aligned}$$

In general, Magboltz values have shown good agreement with corresponding measurements, as for example for Ne-CO_2 mixtures in [35] and [36]. The same temperature dependency of 0.31 %/K was found in [35] by means of simulations as well as high precision measurements of the drift velocity. As can be seen above, the second order Taylor expansion coefficients are so small, that they do not give any further significant contributions or insight into the general structure of the dependencies over the chosen range of variations.

Two dependency plots for pressure and temperature changes are shown in figure 4.1. There is not shown a small systematic parabola which is visible within the pressure dependency when plotting the residuals. This systematic offset increases if the validity range of the pressure is expanded. If larger pressure variations will be observed within the experiment, a second order Taylor expansion will probably become necessary. However, the sigma of the residual distribution is lower than the claimed relative precision of Magboltz, which is 0.05 %. This prooves that the first order Taylor approximation is valid within the chosen range of possible variations.

This parametrization was implemented within the ALICE offline framework AliRoot [33] (see class *AliTPCCalibVDrift*). This approximation at hand allows to estimate quickly and with sufficient precision the drift velocity variations as function of the field and gas property changes. Currently, it is used as an input for the drift velocity for the first order calibration and first reconstruction pass. Furthermore, it is used as a verification tool for the other methods to determine the drift velocity (see section 4.3).

4.2 Simulated temperature distribution within the gas volume

Since the TPC is using a non-saturated gas composition, the drift velocity is unusually sensitive to temperature variations. Therefore, the design goal is to control the tempera-

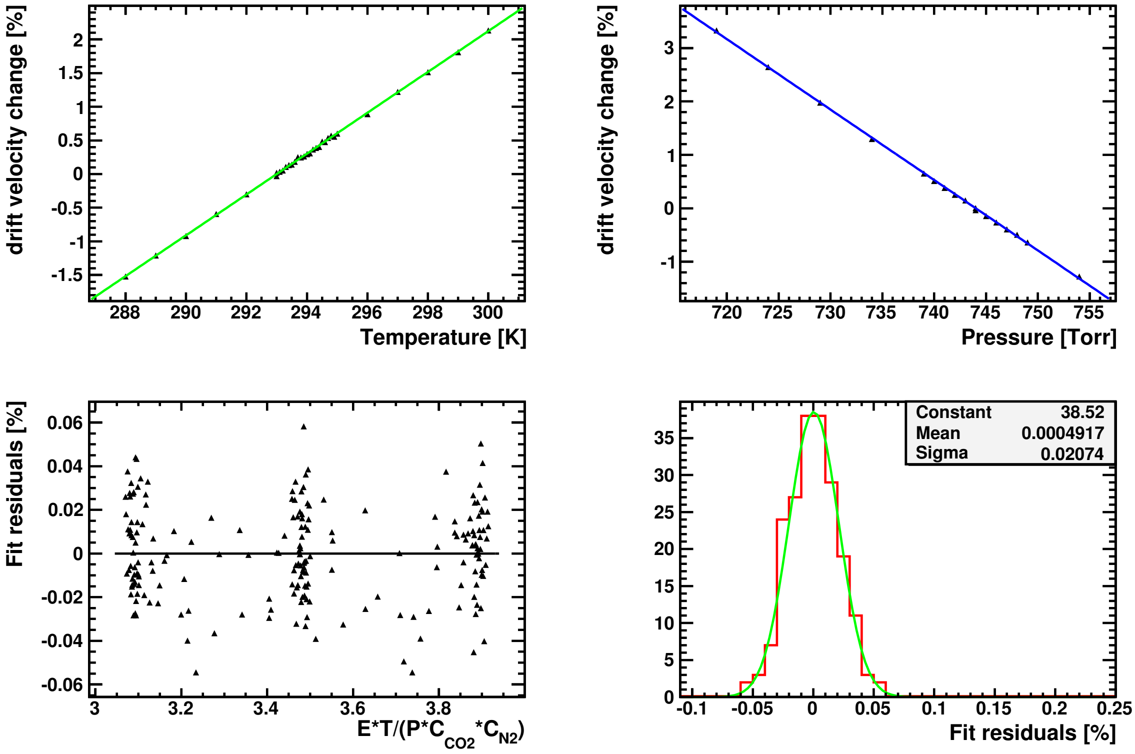

Figure 4.1: Fit residuals of drift velocity parametrization. Residuals are in % of drift velocity changes as simulated with Magboltz. *Upper left:* temperature dependency. *Upper right:* pressure dependency. *Lower left:* including all simulated data points. *Lower right:* histogram representation with error estimation.

ture with an accuracy better then $\Delta T \leq 0.1$ K. To reach this goal, special precautions were taken. For example, heat screeners were installed towards the L3 magnet and towards the end-coils of the Inner-Tracker System (ITS), on the outer and inner barrel of the TPC respectively. A dedicated cooling system was specially developed to provide adjustable cooling temperatures for the differently sized cooling pipes at the Read-Out chambers (electronics) [57].

Several temperature sensors were mounted on the Front End Electronic (FEE), on the Outer- and Inner Containment Vessels (OCV, ICV) and within the TPC gas volume itself (close to the MWPC). These sensors were calibrated with an accuracy better than 0.05 K in order to monitor the temperature stability of the system reliably [58].

However, no thermal screen was inserted in between the ITS and the TPC since this would have increased the material budget significantly. Basically, all detectors are to be kept at the same ambient temperature. But, due to necessary power runs, it takes some time to adjust the cooling power which is needed to hold the detector electronics at the foreseen temperature. Consequently, the aim of the following simulations was to predict the thermal behavior of the drift gas for a given number of different boundary conditions (temperature distribution scenarios).

4.2.1 CFD model description

A report is currently in preparation which contains simulation details as performed by the CFD team at CERN [59]. In here, a brief overview is given to understand the basic definitions as used in the parametrization models of the later case studies.

Geometry and material definition

The basic structure of the ALICE TPC was already mentioned in section 1.3. In terms of a CFD simulation, the most important parameters are the density, viscosity and conductivity values of the materials involved as well as the gas parameters (including its flow). The TPC consists of the outer and inner field cage vessels, which form the sensitive volume filled by approximately 90 m^3 of the drift gas (Ne-CO_2-N_2). Furthermore, an outer and inner containment vessel enclose the inner structure providing additional mechanical stability and an exterior heat shield against main heat sources such as ITS. The volume between this honey-comb based structures is flushed with pure CO_2 gas, thus providing an additional protection against drift gas impurities. The geometrical definitions like positions, diameters and used materials can be found in [20] and [22]. Cross sections of the composite material used for the field cage and containment vessels are described in detail in [20].

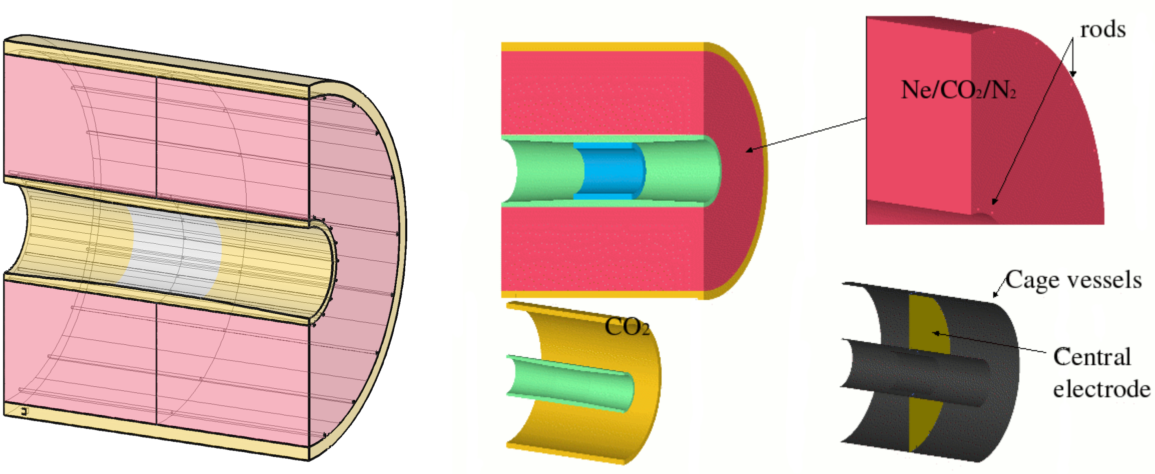

Figure 4.2: CFD MODEL - BASIC OVERVIEW. Shown are the drift volume (red), the containment volumes (green and yellow, flushed with CO_2), the gas in- and outlets (rods) and the central electrode in the middle of the structure. The blue volume represents the air layer between ITS and the inner containment (cage) vessel [60].

Thermo physical properties

The single-component gas properties were available within the StarCD database (see [59]). The corresponding properties of the gas mixture were calculated via weighted average according to their fraction. The resulting values are stated in table 4.2. For a steady-state FE or CFD analysis, which includes rather huge volumes of gas, one of the most important properties is the conductivity; therefore, the approximate formula as given in

Table 4.2: Thermo physical properties of the used gases (from StarCD database).

	fraction [%]	density d [kg/m^3]	viscosity ν [kg/ms]$\cdot 10^{-5}$	specific Heat c_p [J/kgK]	conductivity k [W/mK]
Ne	85.72	0.82542	3.17208	1030.27	0.0487575
CO_2	9.52	1.80817	1.49396	850.57	0.0169655
N_2	4.76	1.14527	1.78837	1040.76	0.0255984
Ne-CO_2-N_2	100.00	0.93425	2.94637	1013.65	0.0401545*

(*) ... approximation according to [61]

[61] was used to get a reliable value. The average thermal conductivity of the main vessels can be found in [62, p.32]. The used honey-comb composition is *nomex* with an average density of 29 kg/m^3. The corresponding thermal conductivity is 3.8934 W/mK.

Boundary & Initial Conditions

The inlets and outlets of the drift gas (drift volume) are rods placed axially (see figure 4.2) with holes of an approximate diameter of 1 mm, therefore the Ne-CO_2-N_2 gas flux is basically radial from the inner rods towards the outer rods. Due to the flux of 20 m^3/h, the drift gas is exchanged about five times a day. The CO_2 volume gas exchange is axially (in z direction). It is flushed with approximately 100 l/h on both, the inner and outer, CO_2 volumes.

The standard temperature is defined to be 20 °C on the Read-Out Chamber (ROC) surfaces, the inner and outer thermal screener as well as on the ITS. An additional ‘air’ layer between the inner containment vessel and the ITS and between the outer containment vessel and the outer thermal screener was built into the model. By doing so, the heat transfer from the assumed main heat sources could be modeled correctly.

4.2.2 Simulated case studies

To predict the magnitude of influence of different heat sources as well as to calculate the resulting temperature distribution within the TPC, the following deviations from the ideal homogeneous boundary conditions were simulated.

Heat source at ITS (heat flux through inner containment vessel)

The first case study assumes, that the inner-most detector in the center of the ALICE experiment could not be kept at the surrounding temperature of 20 °C. Therefore, different temperatures were applied at the outer volume of the ITS to calculate how it affects the temperature distribution within the TPC drift volume.

The first case study already reveals an important fact. Due to the low rate, natural buoyancy prevails on the forced gas flux of the drift gas exchange in radial direction, as is shown in figure 4.3. Figure 4.4 contains various temperature distribution plots within the gas volumes of the TPC. The reason for the temperature peak at the upper half of the TPC drift volume is due to the heat flux from the ITS, whose surface temperature

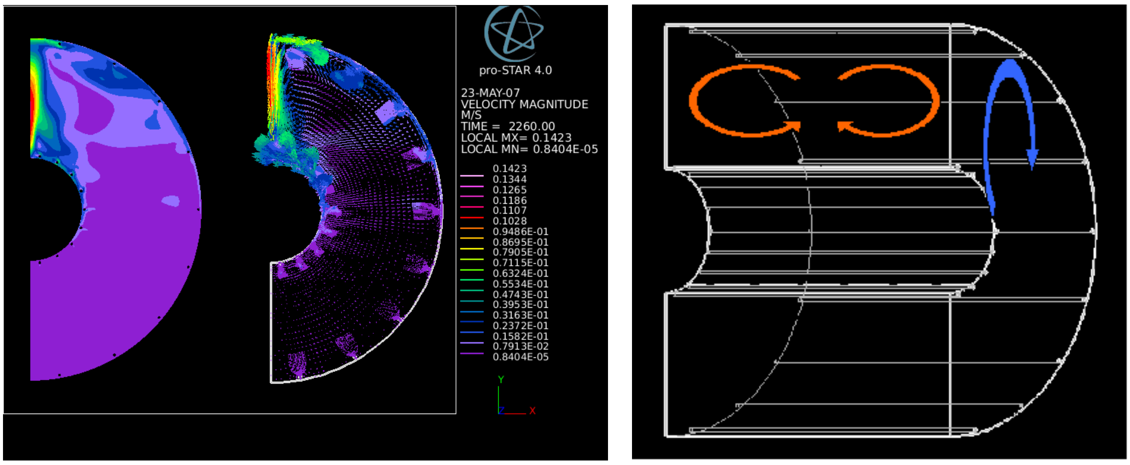
pro-STAR 4.0
23-MAY-07
VELOCITY MAGNITUDE
M/S
TIME = 2260.00
LOCAL MX= 0.1423
LOCAL MN= 0.8404E-05
0.1423
0.1344
0.1265
0.1186
0.1107
0.1028
0.9486E-01
0.8695E-01
0.7905E-01
0.7115E-01
0.6324E-01
0.5534E-01
0.4743E-01
0.3953E-01
0.3163E-01
0.2372E-01
0.1582E-01
0.7913E-02
0.8404E-05
Y
Z
X

Figure 4.3: GAS VELOCITY WITHIN THE DRIFT VOLUME. *Left:* gas velocity distribution as simulated with the boundary condition of 35 °C on the ITS. *Right:* mean vortices (buoyancy prevails) [60].

was set to 35 °C. When reaching the inner CO_2 gas volume, the maximum temperature already dropped to 23 °C due to the interposed air layer and the honey-comb structure of the containment vessel. A maximum temperature of 21.8 °C is carried on into the gas volume, where it manifests as a temperature peak in the vertical direction.

The temperature distribution plotted in figure 4.4 can be parametrized as follows: A simple first-order polynomial function (linear in 3 dimensions)

$$T_{linear}(x, y, z) = T_0 + T_x \cdot x + T_y \cdot y + T_z \cdot z, \qquad (4.2)$$

can be used to describe the global properties of the distribution. T_0 is the mean temperature and T_x, T_y and T_z are the temperature gradients in x, y and z respectively. Three different sets of calculations with varying boundary conditions (temperatures applied on the ITS) were performed and fitted with the model function. The results are shown in table 4.3. No mean gradient in horizontal (x) or longitudinal (z) direction could be observed. Nevertheless, the vertical direction shows a significant linear gradient as the temperature on the ITS increases.

The temperature peak in the upper half within the TPC, as seen in figure 4.4, can be modeled with a function which should preferably be represented in cylindrical coordinates. A combination between the linear model (4.2) and the peak model (4.3) reduces the total

Table 4.3: Temperature gradients within the TPC drift volume, when assuming a heat flux from the ITS.

	T_0[°C]	T_x [°C/500cm]	T_y [°C/500cm]	T_z[°C/500cm]
ITS - 25 deg	20.04 ± 0.01	0.00 ± 0.02	0.14 ± 0.02	-0.01 ± 0.02
ITS - 30 deg	20.08 ± 0.01	0.00 ± 0.02	0.22 ± 0.02	0.00 ± 0.02
ITS - 35 deg	20.16 ± 0.01	0.00 ± 0.02	0.25 ± 0.02	0.01 ± 0.02

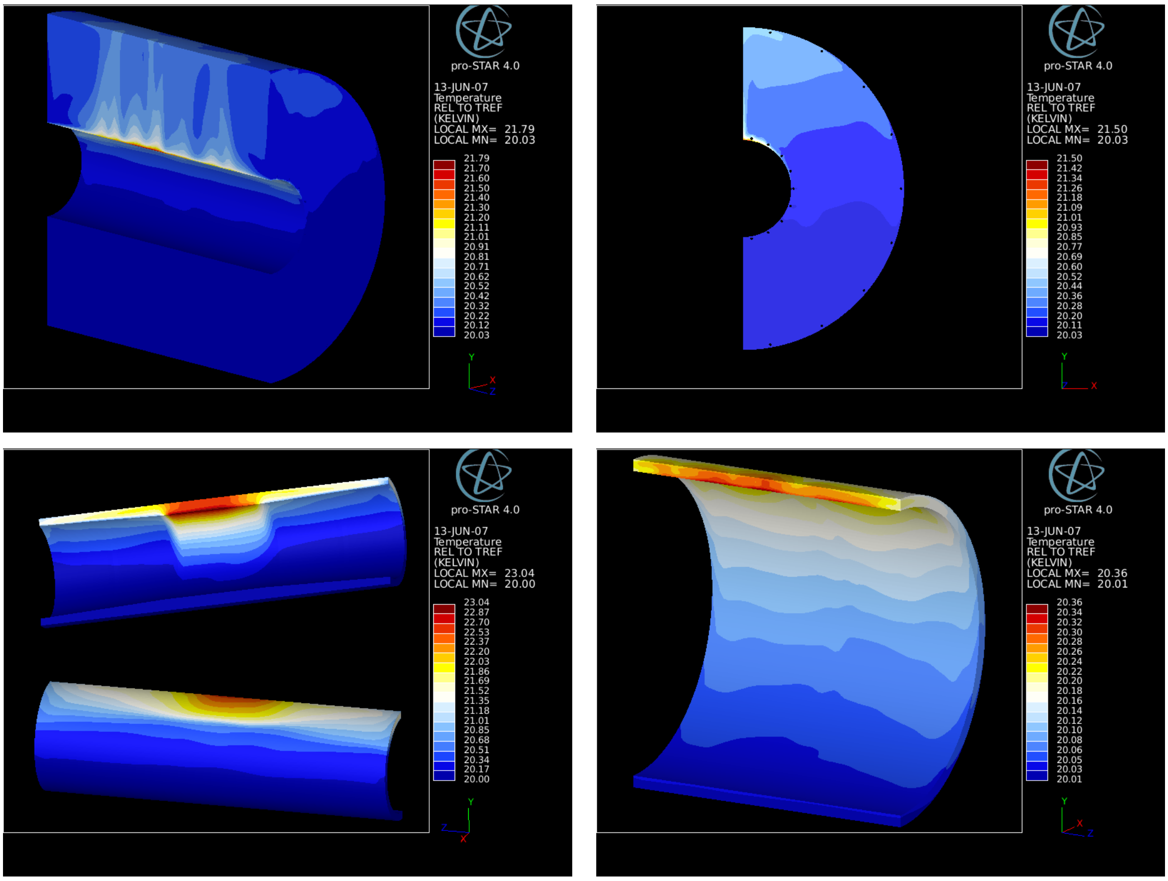
pro-STAR 4.0
13-JUN-07
Temperature
REL TO TREF
(KELVIN)
LOCAL MX= 21.79
LOCAL MN= 20.03
21.79
21.70
21.60
21.50
21.40
21.30
21.20
21.11
21.01
20.91
20.81
20.71
20.62
20.52
20.42
20.32
20.22
20.12
20.03
pro-STAR 4.0
13-JUN-07
Temperature
REL TO TREF
(KELVIN)
LOCAL MX= 21.50
LOCAL MN= 20.03
21.50
21.42
21.34
21.26
21.18
21.09
21.01
20.93
20.85
20.77
20.69
20.60
20.52
20.44
20.36
20.28
20.20
20.11
20.03
pro-STAR 4.0
13-JUN-07
Temperature
REL TO TREF
(KELVIN)
LOCAL MX= 23.04
LOCAL MN= 20.00
23.04
22.87
22.70
22.53
22.37
22.20
22.03
21.86
21.69
21.52
21.35
21.18
21.01
20.85
20.68
20.51
20.34
20.17
20.00
pro-STAR 4.0
13-JUN-07
Temperature
REL TO TREF
(KELVIN)
LOCAL MX= 20.36
LOCAL MN= 20.01
20.36
20.34
20.32
20.30
20.28
20.26
20.24
20.22
20.20
20.18
20.16
20.14
20.12
20.10
20.08
20.06
20.05
20.03
20.01

Figure 4.4: TEMPERATURE DISTRIBUTION WITHIN THE GAS VOLUMES. *upper left:* 3D cut along the z axis of the drift volume. *upper right:* (x,y) temperature distribution at z=0. *lower left:* Inner CO_2 volume. *lower right:* Outer CO_2 volume [60].

residuals to the fit as is shown in figure 4.5.

$$T_{peak}(r, \phi, z) = A_0 \cdot \exp\left[-\frac{r}{\tau_1}^{\frac{1}{2}} - \frac{z}{\sigma}^{2} - \frac{|\phi|}{\tau_2}^{\frac{1}{2}} \right] \tag{4.3}$$

The parameters obtained through the fitting procedure are written in table 4.4. The formula found by the fit turns out to be an excellent choice, since the parameters (τ_1,τ_2,σ), defining the width of the peak in (r,ϕ,z) respectively, do not vary with increasing temperature on the ITS. Instead, only the global scaling factor A_0 increases. This is an excellent opportunity to correlate the scaling parameter with the temperature as measured on the inner side of the inner containment vessel. There, the TPC hosts various temperature sensors which can be used to monitor the heat flux coming from the ITS. The direct correlation between the peak-function parameter A_0 and these temperature readings can be used to cross calibrate a possible peak structure of the temperature distribution within the TPC drift volume.

The residual plots as shown in figure 4.5 are generated by subtracting the fitted model function from the simulated data points. Only points within the sensitive volume (read out volume) were considered. The long tail (residuals up to 1.3 °C) on the upper side of the TPC could be reduced with the additional peak-model. A Gaussian fit of the residuals

Table 4.4: Peak parametrization, when assuming a heat flux from the ITS.

	A	τ_1	σ	τ_2	Temp. sensors [°C]
ITS - 25 deg	2.6 ± 0.4	14 ± 2	183 ± 6	4.01 ± 0.02	23.5
ITS - 30 deg	4.7 ± 0.4	13 ± 2	185 ± 7	4.01 ± 0.02	27.4
ITS - 35 deg	6.4 ± 0.5	13 ± 2	192 ± 7	4.00 ± 0.02	30.5

gives an overall error of σ=0.027 K.

In the case where the temperature sensors on the inner containment vessel exceed the temperature of around 23 degrees, the nonlinear peak model can be used in order to describe the temperature structure within the gas volume. So far, the pertinent temperature sensors did not indicate an extensive heat flux from the ITS, therefore such a peak structure is not to be expected. Without the peak structure, the linear model sufficiently represents the simulated data.

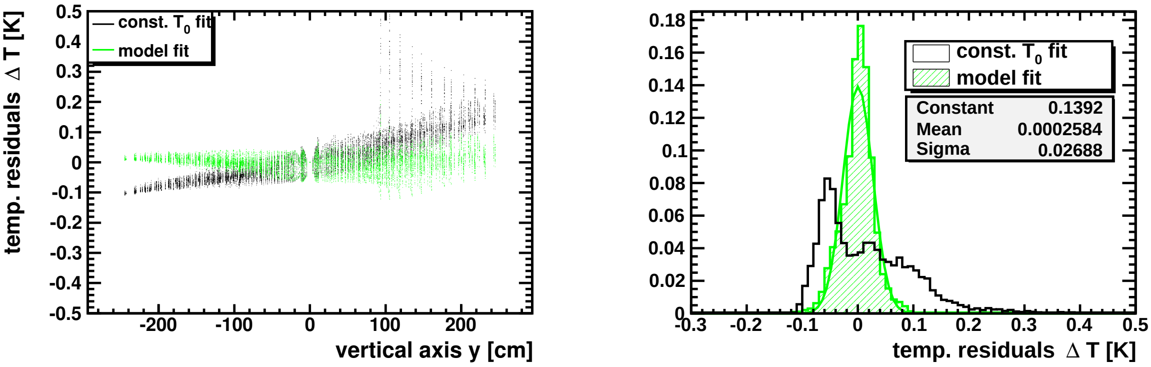

Figure 4.5: FIT RESIDUAL PLOTS FOR HEAT FLUX FROM ITS for the "ITS-35-deg" case; *Left:* temperature residuals for a constant T_0 and the $T_{linear} + T_{peak}$ model. *Right:* normalized residual distribution.

Heat source at the outer detectors (heat flux through outer containment vessel)

Two cases were simulated in order to quantify the influence of heat sources at the surroundings of the TPC. Therefore, outer temperature gradients of 1.5 °C and 5 °C were set as outer boundary conditions. The resulting mean temperture in the z direction is plotted in figure 4.6. If such a gradient occurs, the temperature distribution within the TPC gas volume can not be described with a simple linear model anymore. Although, the gradients in the x and z directions are zero, the gradient in the y direction increases towards the upper half of the TPC.

However, if the outer gradient does not exceed 1.5 °C, a linear model still fits the temperature distribution within the gas volume with the required precision. Nevertheless, systematic deviations towards the top of the TPC have to be handled separately, as is shown in figure 4.7.

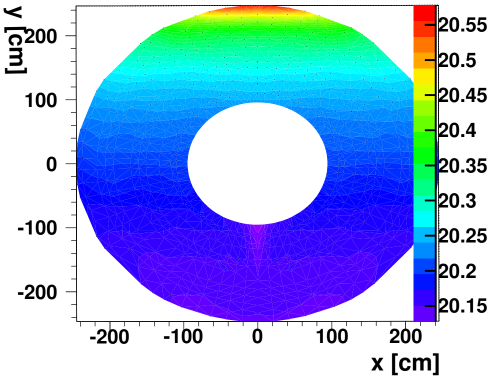

Figure 4.6: Mean temperature due to heat flux from the surroundings within the (x,y)-plane for the "OCV-1.5-deg" case. Plotted is the mean temperature in the z direction.

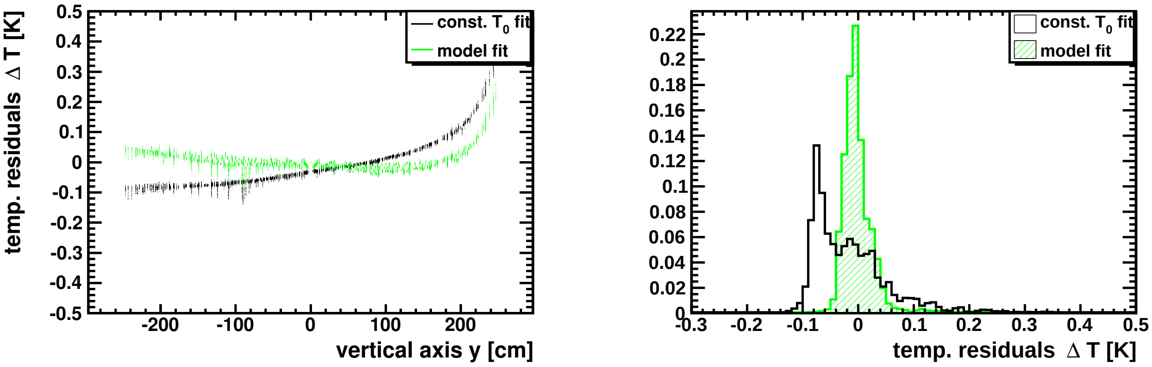

Figure 4.7: Fit residual plots for heat flux from outer detector. for the "OCV-1.5-deg" case; *Left:* temperature residuals for a constant T_0 and the T_{linear} model. *Right:* normalized residual distribution.

Gas temperature variations

If the drift gas, with a flow of 20 m^3/h, is not kept at the TPC temperature when flushed through the TPC, the following temperature distribution can be expected. In general, the distribution is rather non-linear within the volume. The gas itself is brought to thermal equilibrium relatively fast, whereas, at the same time, it tends to build up a vertical gradient. The reason for that is, as already mentioned, that buoyancy prevails over forced gas flow. However, regardless of the non-linearity of this case study, the final temperature distribution is fairly well represented by our linear model within the required accuracy, as is shown in figure 4.8.

Table 4.5 contains the fit parameters of the linear model for the simulated cases studied. If the temperature difference is less then 0.5 K, even the T_0 fit model turns out to be sufficient.

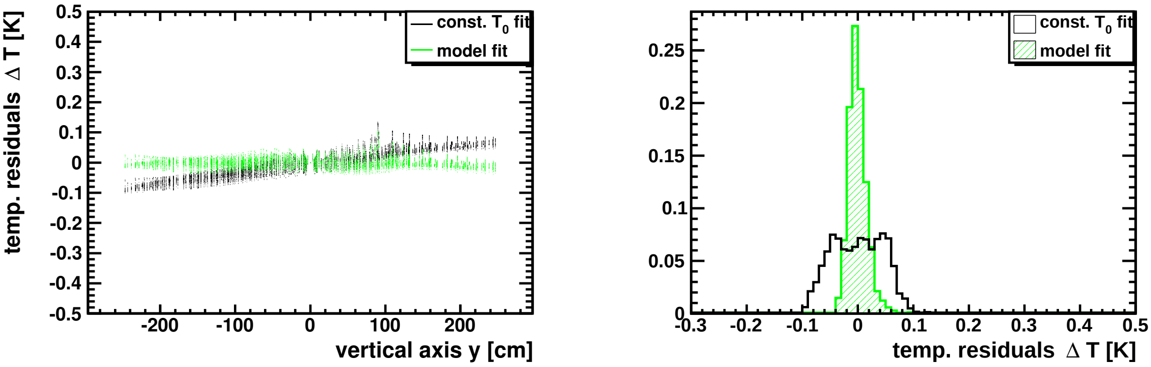

Figure 4.8: FIT RESIDUAL PLOTS FOR VARYING GAS TEMPERATURE for the "GAS-21.5-deg" case. *Left:* temperature residuals for a constant T_0 and the T_{linear} model. *Right:* normalized residual distribution.

Table 4.5: Temperature gradients within the TPC drift volume, when assuming a non-thermalized gas temperature.

	T_0[°C]	T_x [°C/500cm]	T_y [°C/500cm]	T_z[°C/500cm]
GAS - 20.5 deg	20.10± 0.00	0.00± 0.02	0.08 ± 0.02	0.00 ± 0.02
GAS - 21 deg	20.18± 0.00	0.00± 0.02	0.14 ± 0.02	0.00 ± 0.02
GAS - 21.5 deg	20.27± 0.00	0.00± 0.02	0.17 ± 0.02	0.00 ± 0.02

Heat from the read-out-chamber electronics

The read-out chambers are located at the left- and right-hand side of the TPC geometry. In the case, where the cooling of the Frond End Electronics (FEE) is not adjusted to the temperature of the other boundary surfaces, it could lead to a non homogeneous temperature distributions within the TPC. Two different case studies with temperature gradients on the ROC surfaces were performed. The outcome of the steady-state solution was fitted with the linear model. Table 4.6 contains the fitted gradients within the TPC volume. Again, no x or z gradient was observed; the y gradient corresponds to approximately 20 % of the original boundary temperature.

The linear model is perfectly capable to minimize the residuals for a temperature distribution as induced by non-thermalized ROC surfaces, as is shown in figure 4.9.

Table 4.6: Temperature gradients within the TPC drift volume, when assuming heat flux from the read-out chambers.

	T_0[°C]	T_x [°C/500cm]	T_y [°C/500cm]	T_z[°C/500cm]
ROC - 1.5 deg	20.60 ± 0.01	0.03 ± 0.01	0.30 ± 0.01	-0.01 ± 0.01
ROC - 3.0 deg	21.12 ± 0.01	0.03 ± 0.01	0.59 ± 0.01	-0.01 ± 0.01

Parametrization of the temperature distributions

In general, a linear model, as stated in formula (4.2), is sufficient to parametrize the temperature distribution within the sensitive area of the TPC drift volume. The temper-

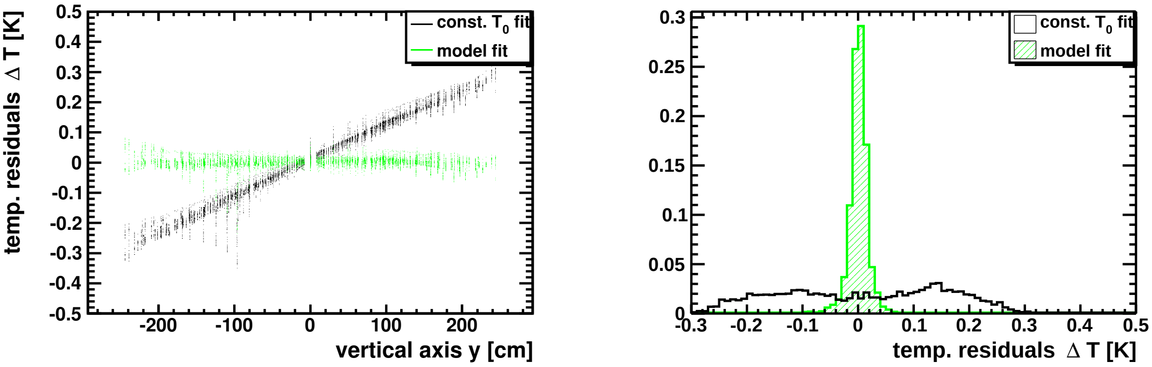

Figure 4.9: Fit residual plots for heat flux from the ROCs for the "ROC-1.5-deg" case; *Left:* temperature residuals for a constant T_0 and the T_{linear} model. *Right:* normalized residual distribution.

ature sensors situated within the TPC gas volume can be used in order to measure the temperature (gradient). The simple model of linear gradients was used in the analysis of these sensors during the various commissioning runs in 2006 and 2008 (see further details in section 4.3). However, if the temperature sensors situated on the inner and outer containment vessel would exceed temperature differences of plus 3 °C in comparison to that in the drift volume, the more sophisticated models of formula (4.3) will have to be used.

So far, just linear temperature gradients in the vertical direction were found before the temperature stabilization was performed. However, after the stabilization which was done by means of fine tuning the various cooling circuits, a temperature gradient of $T_y \leq 0.1$ °C/500cm was achieved on short time scales. More details are given in the following section.

4.3 Temperature and pressure variations

Drift velocity variations within the TPC gas volume can be monitored by measuring its main dependencies; namely, pressure, temperature and gas composition. Dedicated temperature sensors are situated within and around the TPC [63]. A pressure sensor is situated on the HMPID sub-detector support at the same height as the beam. The gas composition will be monitored by the GOOFIE system [30], which is currently in the state of installation and validation. All measured environmental properties are handled by the DCS system and transported via the Shuttle system into the OCDB, where all important reconstruction parameters are stored.

Temperature sensors

The temperature sensor readings can be analyzed by grouping the dedicated sensors together and fitting them with a corresponding fit function. The current implementation to analyze the temperature sensors can be found in the class *AliTPCTempMap* within the AliRoot framework [33]. It includes two-dimensional linear fitters of the pertinent planes where the sensors are situated.

These groups are, for example, sensors on the outer containment vessel (OCV), sensors on the inner thermal screens and containment vessels (ICV), sensors on the front-end electronic of the ROCs on the A and C side as well as sensors within the TPC gas volume, which are situated on the support frame of the ROCs. The later ones are used to evaluate the mean and the temperature gradients (in x,y and z) within the TPC.

Before the cooling circuits were adjusted in June 2008, temperature gradients of up to 0.8 K were observed with these temperature sensors as well as with the central electrode calibration data. Figure 4.10 contains a representative time snapshot of the temperature readings during the run period LHC08d (October, 2008). At that time, the cooling temperature within the different circuits was already adjusted to provide a homogeneous temperature within the TPC.

Within the run presented in figure 4.10, a temperature gradient of less then $\Delta T \leq 0.2$ K was observed. Furthermore, a negative temperature peak on the ROC A side is visible. This peak is due to a too high cooling power on the front end cards of sector A00, since they were not powered within this run. The rather homogeneous temperatures on the inner containment vessel indicate, that the heat load from the ITS detector did not influence the gas temperature within the TPC. A slight temperature gradient of less than 0.5 K was observed on the outer containment vessel. This gradient is most likely due to the outer thermal screen not operating and the temporarily installed ventilation system within the L3 magnet.

In general, the temperature distribution as observed with the temperature sensors is rather sensitive to all power-on and power-off processes of the front end electronics of the TPC itself, as well as similar processes from the TRD and the ITS systems. However, it takes on average 1 hour to reach a stable temperature distribution after the read-out electronics of the TPC has been turned on.

For the upcoming commissioning period in 2009 it is foreseen to fine-adjust the cooling circuits according to the heat dissipation of all sub-detectors, which have to run at stable conditions to perform this operation. With these adjustments completed it is expected, that the design goal of $\Delta T \leq 0.1$ K can be kept throughout the complete commissioning and future data taking periods.

Pressure sensor

Up to this moment, two pressure sensor readings are available via the DCS system. One is situated on the top of the shaft (surface pressure sensor), the other one is mounted on the support structure of the HMPID at beam height (cavern pressure sensor). The cavern pressure sensor is the most important one, since it is an indicator for the mean pressure within the TPC gas volume. The TPC is operating with a constant overpressure of 0.4 mbar to minimize atmospheric impurities within the drift gas.

Figure 4.11 displays pressure variations within the cavern as measured over a period of one week. Within this week, pressure variations of up to 15 mbar could be observed. According to the parametrized dependencies in section 4.1 this corresponds to a drift velocity change of up to 1.8 % within this time period. However, the temperature changes within this period were less then 0.2 K, which corresponds to a drift velocity change of less then 0.06 %.

The pressure gradient within the TPC can be calculated using the simple barometric

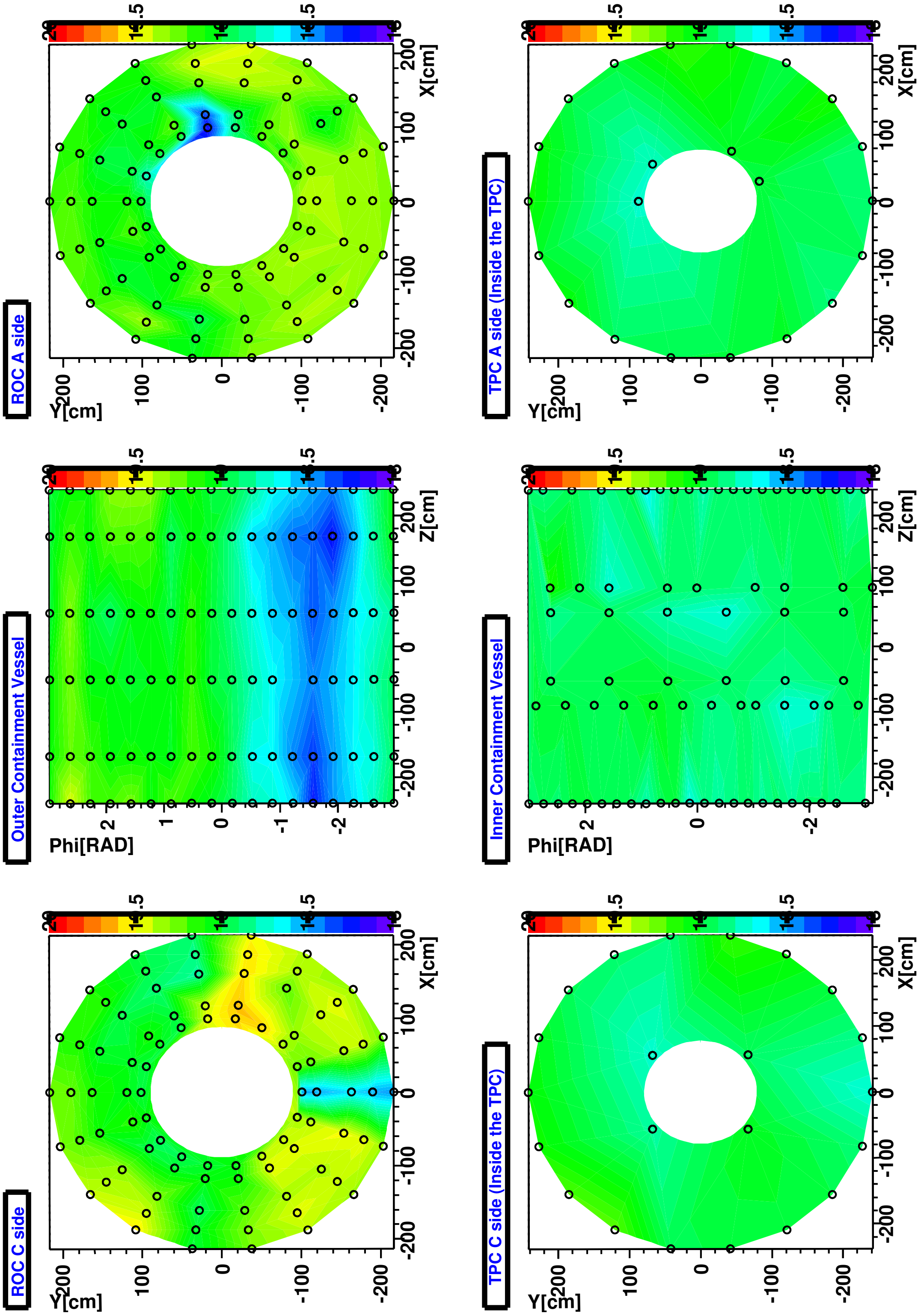

Figure 4.10: TEMPERATURE MAPS FROM SENSOR READINGS. Run number: 61420 (LHC08d period). Time: 3 h (from start of run). Sensors readings (marked with circles) are grouped according to their positions. The intermediate space was interpolated linearly.

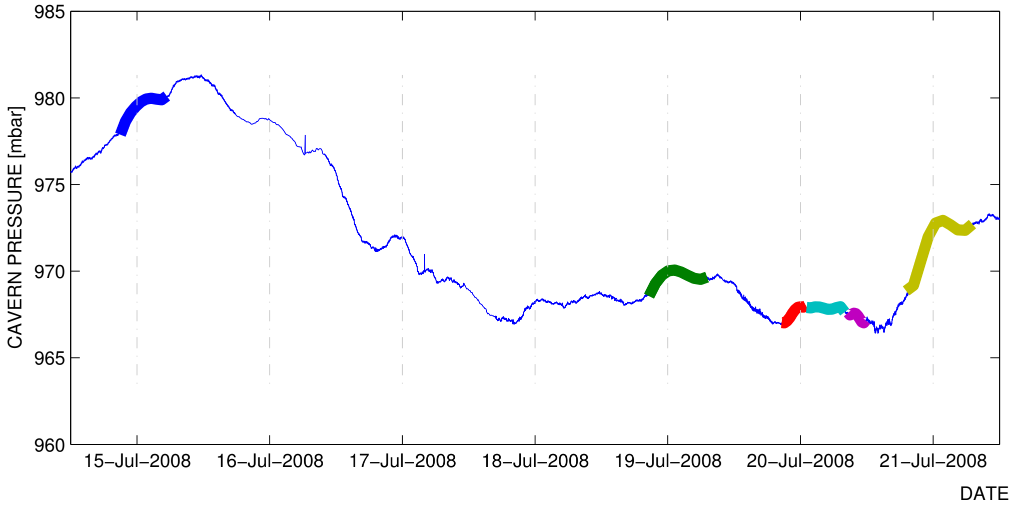

Figure 4.11: Pressure variations over one week. Shown are the readings from the cavern pressure sensor (at beam height) during one week (blue). The colored bold lines indicate different runs. During this week, a change of drift velocity up to 1.8 % can be attributed to the pressure variations.

formula as stated below. This leads to a pressure drop of:

$$\Delta p_h = \rho_{gas} \cdot h \cdot g = 0.934 \cdot 5 \cdot 9.81 = 46 \ Pa = 0.46 \text{ mbar},$$

over the full height of h=5 m which corresponds to a linear drift velocity increase towards the top of 0.04 %. The same pressure increase was found within the CFD simulation, as metioned in section 4.2, which takes additional pressure variations from the gas flux into account.

Unfortunately, unlike the temperature and the gas composition, the pressure variations can not be controlled and are therefore the biggest contributor to the drift velocity changes due to gas densities within the TPC. This fact is shown in the following subsection, where measurements of the TPC drift velocity are compared to the predictions based on the various measurements of the ambient conditions.

4.3.1 Drift-velocity: matching ITS-TPC tracks

By matching cosmic tracks, which cross the TPC and the ITS detector, the drift velocity changes within the TPC gas volume can be measured over time. Therefore, a simplified model which describes the reconstructed position of the cluster in dependence on the drift velocity changes was developed. This model can be used to minimize the differences in the cluster positions as they were reconstructed within the TPC and the ITS system.

In general, the ITS provides a better position resolution than the TPC; therefore, cluster positions and track inclinations as reconstructed by the ITS are more exact. Hence, when using the drift velocity parameters within the simplified model as fit parameters, the ITS-TPC track alignment provides most accurate drift velocity values. This method, however, can not be used to distinguish between the different influences like pressure and temperature variations, but provides values which are a superposition of those effects.

The simplified model which is implemented in the algorithm for the track matching on the A side is discussed below [64]. It assumes a scaling of the mean drift velocity v_0 in comparison to the drift velocity as used in the first reconstruction pass (at standard conditions). In addition, a linear gradient in the vertical (y) direction was included. Therefore, the true drift velocity v_d is a function of y:

$$v_d(y) = v_0 + a\,y. \tag{4.4}$$

The real z position of the cluster on the A side is therefore:

$$z = L_A - (v_0 + a\,y) \cdot t. \tag{4.5}$$

In here, L_A represents the total drift length within the TPC A side and a represents the gradient in the vertical direction. So far, the reconstruction software uses a constant drift velocity $v_d^{rec} = c \cdot v_0$, which deviates from the the real (changing) mean drift velocity v_0 by a factor c. Furthermore, the reconstructed z^{rec} position also includes wrong drift times due to possible trigger offsets t_0. Thus we get:

$$z^{rec} = L_A - c\,v_0 \cdot (t - t_0). \tag{4.6}$$

Rearranging those formulas and expressing t through equation (4.5) leads to the residuals which are minimized:

$$\Delta z = z^{rec} - z = -\frac{L_A - z}{v_0 + a\,y}(c\,v_0 + v_0 + a\,y) - c\,v_0\,t_0 \tag{4.7}$$

In here, the fit parameters are the scaling factor c, the real drift velocity v_0 and its gradient in the vertical direction a. When unknown, also the trigger offset t_0 can be fitted. The method is based on the general minimization procedure called a Kalman filter. It allows to include the error propagation from the previous minimization steps in order to maximize the convergence speed.

This model was motivated by the linear gradient as observed in the CFD simulations and the temperature sensors readings as well as the varying mean drift velocity due to the pressure variations. Possible drift velocity offsets due to long-term gas composition variations and mean offsets of the field settings are hereby included as well.

The following paragraphs contain a direct comparison of diferent runs during the LHC08d run period in autumn of 2008. The mean drift velocities v_0 found through the Kalman minimization are plotted in figure 4.12 (data from [64]). In there, drift velocity jumps between the different runs refer to periods where no data was taken. However, for the sake of an easier comparison, the x axis was chosen to be the integrated run time.

Figure 4.13 displays the pressure sensor readings as taken in the cavern. When compared to figure 4.12 it reveals the inverse relation between drift velocity and pressure. The first runs within the LHC08d run period also indicated, that a higher granularity than a mean pressure per run is needed. Therefore, starting from run 61312 onwards, pressure values with a granularity of minutes were stored within the OCDB.

The mean temperature within the TPC gas volume over this period was stable within 0.2 K, as is shown in figure 4.14. Furthermore, the vertical temperature gradient did not exceed 0.2 K throughout the displayed runs. Hence, a drift velocity change of maximum

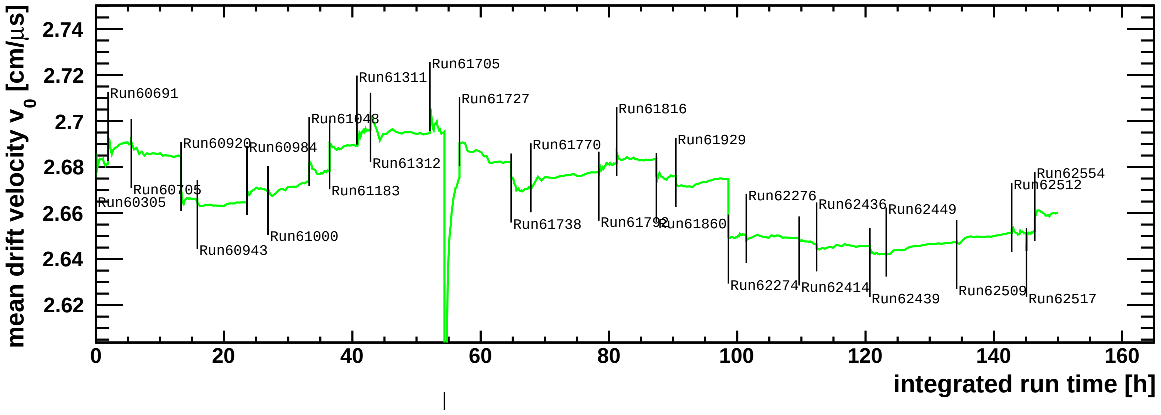

Figure 4.12: Mean drift velocities during the run-period LHC08d as found by the method of matching TPC-ITS tracks by means of the Kalman filter minimization. The x axis represents the integrated run time over usable runs, which provided usable sensor readings of the ambient conditions.

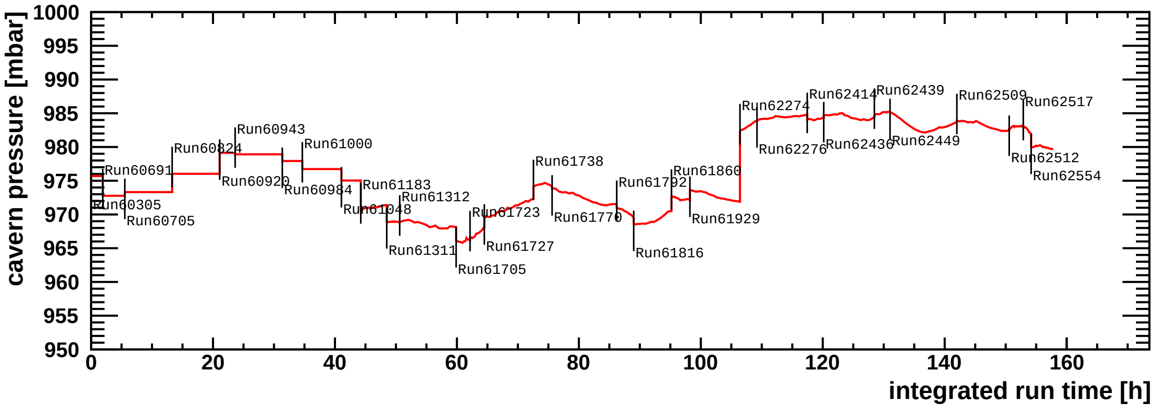

Figure 4.13: Pressure readings during the run-period LHC08d as measured with the cavern pressure sensor, which is situated at the same height as the beam line.

0.06 % can be attributed to temperature variations, which certainly does not explain the variations as shown in figure 4.15.

The relative change of the drift velocity is plotted in figure 4.15 for different runs during autumn 2008. Two different evaluation methods were considered. The green line represents the drift velocity change as found by means of the ITP-TPC track matching. The red line was evaluated using the pressure and temperature sensor readings within the parametrization model as discussed in section 4.1. In general, the method based on the ITS-TPC track matching is considered to be more accurate, since it includes not only P and T variations but the overall effects which influence the gas density.

The major offset at the start of run 61723 was due to wrong initial values of the fit parameters within the Kalman minimization procedure. Especially at the start of each run the error bars (not plotted) are larger in comparison to those at the end of the run. However, the major time dependence, even within the runs, could be reconstructed.

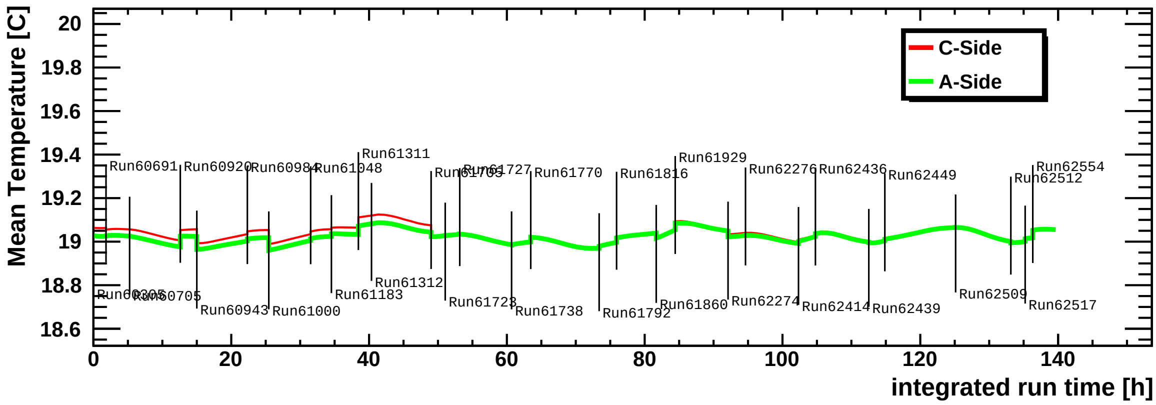

Figure 4.14: MEAN TEMPERATURES DURING THE RUN-PERIOD LHC08D independently evaluated for the A and C side within the TPC gas volume. The observed temperature stability is within 0.2 K. *Note:* the outer thermal screen was not operated during this runs.

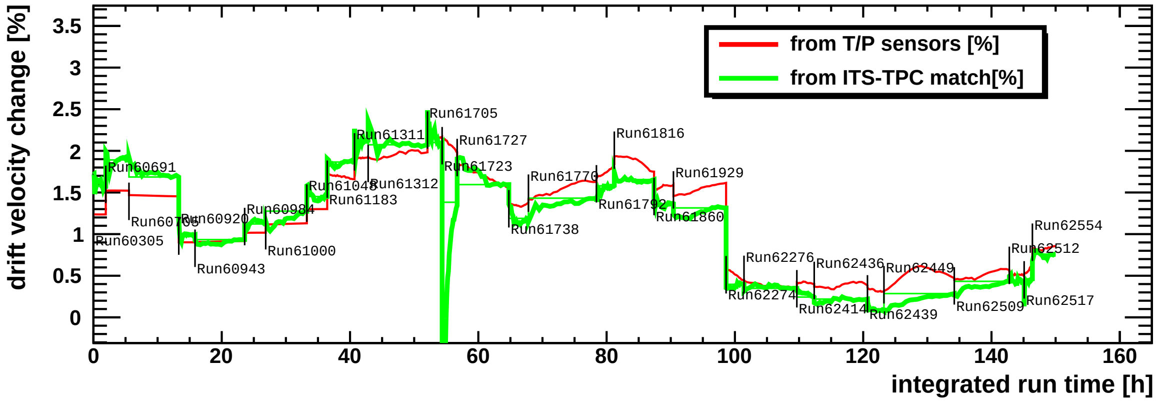

Figure 4.15: RELATIVE DRIFT VELOCITY CHANGE DURING THE RUN-PERIOD LHC08D. Compared are two evaluation methods.

Within figure 4.15 the relative change as found by means of the pressure and temperature readings show a systematic time dependent offset in comparison to the second method. It is believed that this offset, which swaps from positive to negative over the integrated run time, is due the gas composition variations which were not included in the analysis. No feasible gas composition readings were available at the moment of data taking. Basically, the GOOFIE monitoring system [30] should provide measurements regarding the CO_2 and N_2 concentrations within the TPC gas. However, during the run period LHC08d, the relative errors of these measurements exceeded 100 %. Thus, it was not possible to take the gas composition variations into account, in a quantitative way. However, when fitting the complete period of N_2 measurements, a tendency of a small increase could be observed. At least qualitatively, this increase would correspond to the time systematic offset between the two evaluation methods as shown in figure 4.15.

Although the drift velocity calibration by means of the ITS-TPC track matching is considered to be more accurate, it is not feasible to include it within the first reconstruction pass due to the required computational effort. Therefore, the parametrization of the drift velocity as discussed in section 4.1, is currently in use as a first order calibration of the drift velocity. This is possible since the sensor readings are immediately available after the run-data was stored. The 2^{nd} order drift velocity calibration, which is performed within the second reconstruction pass, is using this drift velocity changes as initial values. During the upcoming commissioning runs in 2009 it is expected that with the help of this strategy the drift velocity calibration will reach its required relative accuracy of 10^{-4}.

4.4 High multiplicity environments

So far, just dynamic drift velocity changes due to the gas density (affected by changes of pressure, temperature and composition) were discussed and measured in the experiment. However, when high multiplicity events with possible space charge pile up are considered, the need for a more detailed model becomes imperative. How the drift velocity depends on the electrical field was already discussed in section 4.1. But with varying electrical field components, also the mean direction of the electrons are influenced as discussed in section 2.3.

Especially for heavy-ion collisions, distortions due to space charge pile up are not negligible anymore. In the analysis of a single collision of heavy ions, the fluctuations of space charge within the TPC gas volume is highly dynamic. However, when a pile up of several hundred events is analyzed, the space charge within the volume might become rather static due to the ion mobility, which is slower by a factor 1000 than that of the electrons. The accuracy of calculated distortions depends heavily on the accuracy of the field calculation.

How such field calculations for a TPC field cage geometry can be performed without using time consuming Finite Element methods is the topic of the following chapter. It includes the field calculation and the simulation of expected space charge scenarios within the TPC as well as the possible dynamic distortions of the electron drift throughout the drift volume.

Chapter 5

Analytical approach to space charge effects

Within the previous chapters all major effects which can cause deviations of the ideal electron drift within TPCs, both of static and dynamic nature, were discussed. The magnitude of their contributions was identified and correction models were presented. Especially in high multiplicity environments like Pb–Pb collisions additional distortions due to dynamic variations of the drift field are expected. The ions generated by high energy particles traversing the gas volume accumulate within the drift volume which causes non-negligible dynamic variations of the drift field.

The basic concept of simulating such deviations is shown in figure 5.1. The first step is to calculate the electrical field deviations due to positive ions accumulated within the volume. Up to now, this task is performed by solving the inhomogeneous Laplace equation with the help of discrete numerical methods like Finite Elements. Due to computational limitations, assumptions like radial symmetry are common. Therefore, radially symmetric space charge distribution cannot be handled within a feasible time and acuracy. Furthermore, due to limitations regarding the cell size of the model, the space charge distribution are generally assumed to be rather smooth. A short description of the numerical model as it is used within the STAR experiment can be found in [65].

In contrast to [65], the first section in this chapter contains an analytical approach based on Green's functions to calculate the field deviations caused by positive space charges, for geometries typically used for TPCs. Further details on the derivation of the analytical solutions and their properties can be found in [66] (or [67] for a slightly different TPC geometry). However, step two in figure 5.1 represents the simulation of the consequent distortions of the electron drift. This can be done by solving the Langevin equation as already used in section 2.2 but now, with an inhomogeneous electrical drift field.

The second section within this chapter contains details regarding the simulation of expected and possibly unexpected (unlikely) space charge scenarios within the ALICE TPC as well their distorting potential. The space charge pile up was found using the state-of-art simulation code as it is implemented within the ALICE offline framework [33]. To calculate the resulting distortion, either Garfield [39] or a customized algorithm (Euler or Runge-Kutta based) can be used.

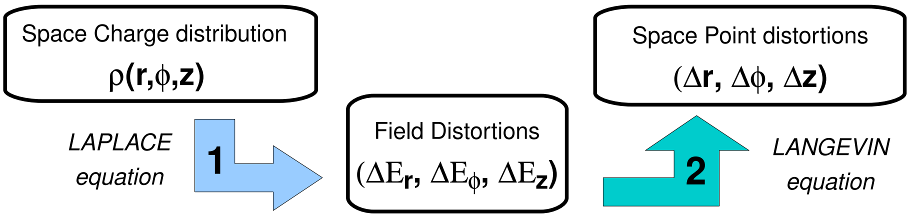

Figure 5.1: Basic concept of simulating space charge deviations. Solving the inhomogeneous Laplace equation for a given space charge accumulation ρ leads to the electrical field deviations $\Delta\vec{E}$. Then, by solving the Langevin equation, the resulting electron drift distortions are calculated.

5.1 Point charge in a coaxial cavity

The geometry of a typical TPC, e.g. [20], can be approximated by two concentric cylinders of radii $r = a$ and $r = b$ with $a < b$. The cylinders are closed at $z = 0$ and $z = L$. The conductivities of these surfaces bounding a coaxial cylindrical cavity are assumed to be infinite. The task is to calculate the potential and the electric field due to an arbitrary charge distribution contained in this cavity. This can be done with the help of the corresponding Green's function $G(r, \phi, z; r', \phi', z')$, which gives the potential at the point (r, ϕ, z) of a point charge located at the point (r', ϕ', z'). The potential of a charge cloud is obtained by integrating the Green's function times the charge distribution over the volume occupied by the charge distribution (see subsection 5.2.2). Methods to derive the Green's function and to express the solution are well described by [68], [69] and [70]. Useful representations of the solution for the problem at hand are given in [71].

For the application to the TPC space charge effect it is necessary to evaluate the potential and the electric field at almost all points of the cavity, including configurations where the point of observation is near to the source point, and both may be near to one of the boundaries. These requirements lead to considerable difficulties: the Green's functions for such a cavity can only be represented by infinite series and/or integrals. These series or integrals may become poorly convergent (those for the electric field components even divergent) on and near manifolds, i.e. curves or surfaces, passing through the source point. This unfavorable behavior is not confined to the singular manifold but prevails in a volume surrounding it. Fortunately, the same Green's function can be represented in various ways; each representation has its own singular manifold. But these manifolds have different shapes and extents; so, one representation may be usable in a volume where another one fails. For that reason it is recommended to find as many different representations as possible and as long as these are practical to use from the point of view of analytical and numerical evaluations.

There are unfavorable configurations where the field and the source point are very near to each other or/and both are very near to a boundary. There are recipes for curing these curses by extracting dangerous terms from the series or integrals in such a way that this subtraction can be compensated by known closed expressions. Such remedies were described before [72, 73]. An additional representation using these methods is discussed in section 5.1.4.

The art of separation

The potential equation in cylindrical coordinates

$$\Delta\Phi = 0, \qquad \left(\frac{\partial^2}{\partial r^2} + \frac{1}{r}\frac{\partial}{\partial r} + \frac{1}{r^2}\frac{\partial^2}{\partial \phi^2} + \frac{\partial^2}{\partial z^2}\right)\Phi(r,\phi,z) = 0, \tag{5.1}$$

can be separated with the well known ansatz

$$\Phi(r,\phi,z) = R(r)\bar{\Phi}(\phi)Z(z). \tag{5.2}$$

The azimuthal factor of the solution must be periodic $\bar{\Phi}(\phi) = \bar{\Phi}(\phi + 2\pi)$, therefore the following solution is common:

$$\bar{\Phi}_m(\phi) = C_m\, e^{im\phi} = A_m \cos(m\phi) + B_m \sin(m\phi) \qquad \text{with } m \in \mathrm{Z}. \tag{5.3}$$

This implies a positive separation constant α^2 when separating the azimuthal term from the combined radial and longitudinal expression wherein the periodic boundary conditions enforce the separation constant to be an integer $\alpha = m \in \mathrm{Z}$.

The sign of the second separation constant arising in the separation of the radial from the longitudinal factor of the solution may be chosen positive or negative; in consequence the radial factor comprises normal Bessel functions or modified Bessel functions of integer order m.

$$\frac{R_{rr}}{R} + \frac{1}{r}\frac{R_r}{R} - \frac{m^2}{r^2} = -\frac{Z_{zz}}{Z} = \begin{cases} -\beta^2, & \text{case I;} \\ \beta^2, & \text{case II .} \end{cases} \tag{5.4}$$

These two types of solutions will be worked out in the following two subsections. The rather unconventional choice of a negative $-\alpha^2$ when separating the azimuthal factor from the others leads to the one-dimensional diffusion equation and its general solution

$$\bar{\Phi}_\alpha(\phi) = C_\alpha\, e^{\alpha\phi} = A_\alpha \cosh(\alpha\phi) + B_\alpha \sinh(\alpha\phi). \tag{5.5}$$

How to fulfill the periodic boundary conditions with this kind of solution will be discussed later on at the appropriate place in the course of the complete derivation (see subsection 5.1.3).

As before, the sign of the second separation constant used to separate the longitudinal from the radial term can be chosen positive or negative which leads to the following cases:

$$\frac{R_{rr}}{R} + \frac{1}{r}\frac{R_r}{R} + \frac{\alpha^2}{r^2} = -\frac{Z_{zz}}{Z} = \begin{cases} -\beta^2, & \text{case III;} \\ \beta^2, & \text{case IV .} \end{cases} \tag{5.6}$$

These cases implying normal or modified Bessel functions of imaginary non-integer order will be discussed in subsection 5.1.3.

5.1.1 Green's function represented by ordinary Bessel functions

Case I of equation (5.4) leads to

$$\left(\frac{\partial^2}{\partial z^2} - \beta^2\right) Z = 0, \tag{5.7}$$

$$\left[\frac{\partial^2}{\partial r^2} + \frac{1}{r}\frac{\partial}{\partial r} + \left(\beta^2 - \frac{m^2}{r^2}\right)\right] R = 0. \tag{5.8}$$

where the radial term is a solution of Bessel's differential equation with argument βr. The general solutions are:

$$Z_m(z) = C_m \cosh(\beta z) + D_m \sinh(\beta z), \tag{5.9}$$

$$R_m(r) = E_m J_m(\beta r) + F_m Y_m(\beta r). \tag{5.10}$$

Accounting for the Dirichlet boundary conditions at the inner and outer radii, $r = a$ and $r = b$, we find the following solution:

$$R_{mn}(r) = Y_m(\beta_{mn} a) J_m(\beta_{mn} r) - J_m(\beta_{mn} a) Y_m(\beta_{mn} r). \tag{5.11}$$

In here, the radial factor of the potential is obviously zero for $r = a$. Discrete values of β result from the boundary condition at $r = b$. β_{mn} can be calculated from $x_{mn} = \beta_{mn} b$, which is the n-th zero of

$$J_m(x) Y_m(lx) - J_m(lx) Y_m(x) \qquad \text{with } l = a/b. \tag{5.12}$$

A few examples of function (5.11) comprising the discrete β_{mn} chosen to fulfill the boundary conditions at $r = b$ can be found in [66].

The Green's function can be found through solving the inhomogeneous potential equation with a unit source (in cylindrical coordinates)

$$\Delta G(\vec{x}; \vec{x}') \;=\; -\,\delta(\vec{x} - \vec{x}'), \tag{5.13}$$

$$\left[\frac{\partial^2}{\partial r^2} + \frac{1}{r}\frac{\partial}{\partial r} + \frac{1}{r^2}\frac{\partial^2}{\partial \phi^2} + \frac{\partial^2}{\partial z^2}\right] G(r, \phi, z; r', \phi', z') = -\,\frac{\delta(r - r')}{r'}\,\delta(\phi - \phi')\,\delta(z - z'), \tag{5.14}$$

using the Fourier series representations of the delta distributions for ϕ and r:

$$\begin{aligned}
\delta(\phi - \phi') &= \frac{1}{2\pi}\sum_{m=-\infty}^{\infty} e^{im(\phi - \phi')} = \frac{1}{2\pi}\sum_{m=0}^{\infty}(2 - \delta_{m0})\cos[m(\phi - \phi')], && (5.15)\\
\frac{\delta(r - r')}{r} &= \sum_{n=1}^{\infty}\frac{R_{mn}(r) R_{mn}(r')}{\bar{N}^2_{mn}} \quad \text{with} \quad \bar{N}^2_{nm} = \int_a^b R^2_{mn}(r)\; r dr, && (5.16)\\
m &= 0, 1, 2, \dots\;.
\end{aligned}$$

The normalization constant $\bar{N}^2_{nm}$ is

$$\bar{N}^2_{nm} \;=\; \frac{2}{\pi^2\,\beta^2_{mn}}\;\left[\frac{J^2_m(\beta_{mn} a)}{J^2_m(\beta_{mn} b)} - 1\right]. \tag{5.17}$$

This is found from a formula for integrals over squares of Bessel functions [74, p.132,eq.(11)]. The resulting expression is simplified with the help of the eigenvalue condition $R_{mn}(b) = 0$. The complete derivation can be found in the appendix of [66].

We choose the following ansatz for the Green's function:

$$G(r,\phi,z;r',\phi',z') = \frac{1}{2\pi}\sum_{m=0}^{\infty}\sum_{n=1}^{\infty}(2-\delta_{m0})\cos[m(\phi-\phi')]\frac{R_{mn}(r)R_{mn}(r')}{\bar{N}_{mn}^2}\, g_{mn}(z,z'). \quad (5.18)$$

Inserting the above representations of the delta distributions into (5.14) and using the solutions already found for the equations of the radial and azimuthal factors, we find the remaining inhomogeneous differential equation for the longitudinal factors, which is

$$\left(\frac{\partial^2}{\partial z^2} - \beta_{mn}^2\right) g_{mn}(z,z') = -\,\delta(z-z'). \quad (5.19)$$

The corresponding homogeneous equations is the one-dimensional time-independent diffusion equation. Its Green's function can be found with the method of particular integrals as described in [68]. Therefore we choose the Green's function to be:

$$g_{mn}(z,z') = A_{mn}\begin{cases} Z_1(z)Z_2(z'), & \text{for } 0 \le z < z' \le L; \\ Z_2(z)Z_1(z'), & \text{for } 0 \le z' < z \le L. \end{cases} \quad (5.20)$$

or equally, with $z_<$ for $0 \le z' < z \le L$ and $z_>$ for $0 \le z < z' \le L$,

$$g_{mn}(z,z') = A_{mn}Z_1(z_<)Z_2(z_>). \quad (5.21)$$

Here, Z_1 and Z_2 are the particular solutions of the homogeneous equation for the two boundary conditions, $Z(0) = 0$ and $Z(L) = 0$. We chose $Z_1 = \sinh(\beta_{mn}z_<)$ and $Z_2 = \sinh(\beta_{mn}(L - z_>)$. A_{mn} can be calculated via

$$A_{mn} = -\frac{1}{p(z')W(z')},$$

where $W(z)$ is the Wronskian of the two particular solutions, i.e. $W(z) = W(Z_1, Z_2) = \beta_{mn}\sinh(\beta_{mn}L)$. In our case, $p(z) = 1$. The Green's function of the one-dimensional diffusion equation with Dirichlet boundary conditions is therefore:

$$g_{mn} = \frac{\sinh(\beta_{mn}z_<)\sinh(\beta_{mn}(L-z_>))}{\beta_{mn}\sinh(\beta_{mn}L)}. \quad (5.22)$$

The complete expression of the Green's function for a coaxial cavity represented by common Bessel functions is:

$$G(r,\phi,z;r',\phi',z') = \frac{1}{2\pi}\sum_{m=0}^{\infty}\sum_{n=1}^{\infty}(2-\delta_{m0})\cos[m(\phi-\phi')]\frac{R_{mn}(r)R_{mn}(r')}{\bar{N}_{mn}^2}\frac{\sinh(\beta_{mn}z_<)\sinh(\beta_{mn}(L-z_>))}{\beta_{mn}\sinh(\beta_{mn}L)}, \quad (5.23)$$

wherein $R_{mn}(r)$, $\bar{N}_{mn}^2$ are given in eqs.(5.11), (5.17) respectively.

5.1.2 Green's function represented through modified Bessel functions

Case II of equation (5.4) leads to

$$\left(\frac{\partial^2}{\partial z^2}+\beta^2\right)Z=0, \tag{5.24}$$

$$\left[\frac{\partial^2}{\partial r^2}+\frac{1}{r}\frac{\partial}{\partial r}-\left(\beta^2+\frac{m^2}{r^2}\right)\right]R=0, \tag{5.25}$$

where the radial factor obeys the modified Bessel differential equation with argument βr. The general solutions are:

$$Z(z)=C_m\cos(\beta z)+D_m\sin(\beta z), \tag{5.26}$$

$$R(r)=E_mI_m(\beta r)+F_mK_m(\beta r). \tag{5.27}$$

The boundary conditions at the end of the z interval, $\Phi(r,\phi,0)=\Phi(r,\phi,L)=0$, enforce C_m to be zero and require discrete values for β, namely $\beta_n=n\pi/L$.

Using the Fourier series representations of the delta distributions for ϕ and z

$$\delta(\phi-\phi') = \frac{1}{2\pi}\sum_{m=-\infty}^{\infty}e^{im(\phi-\phi')}=\frac{1}{2\pi}\sum_{m=0}^{\infty}(2-\delta_{m0})\cos[m(\phi-\phi')], \tag{5.28}$$

$$\delta(z-z') = \sum_{n=1}^{\infty}\frac{\sin(\beta_nz)\sin(\beta_nz')}{N_{mn}^2} \quad \text{with} \quad N_{nm}^2 = \int_0^L\sin^2(\beta_nz)dz=\frac{L}{2}, \tag{5.29}$$

we assume the following series for the Green's function:

$$G(r,\phi,z;r',\phi',z')= \tag{5.30}$$

$$=\tfrac{1}{2\pi}\textstyle\sum_{m=0}^{\infty}\sum_{n=1}^{\infty}(2-\delta_{m0})\cos[m(\phi-\phi')]\ \tfrac{2}{L}\ \sin(\beta_nz)\sin(\beta_nz')\ g_{mn}(r,r').$$

This expansion and the two previous ones for the delta distributions lead to the modified Bessel differential equation, which is not self-adjoint. Multiplying it with r results in a self-adjoint equation so that the method mentioned in the previous chapter may be applied. For g_{mn} we start with:

$$g_{mn}(r,r')=A_{mn}R_{mn\,1}(r_<)R_{mn\,2}(r_>). \tag{5.31}$$

For the Dirichlet boundary conditions at the radius $r=a$ the following particular solution can be assumed:

$$R_{mn\,1}(r)=K_m(\beta_na)I_m(\beta_nr)-I_m(\beta_na)K_m(\beta_nr). \tag{5.32}$$

A similar one, which fulfills the boundary condition at $r=b$, is:

$$R_{mn\,2}(r)=K_m(\beta_nb)I_m(\beta_nr)-I_m(\beta_nb)K_m(\beta_nr). \tag{5.33}$$

The Wronskian of these two particular solutions is

$$W(r)=\frac{I_m(\beta_nb)K_m(\beta_na)-I_m(\beta_na)K_m(\beta_nb)}{r}. \tag{5.34}$$

For the constant A_{mn} we get

$$A_{mn} = -\frac{1}{p(r)W(r)} = \frac{1}{I_m(\beta_n a)K_m(\beta_n b) - I_m(\beta_n b)K_m(\beta_n a)}. \tag{5.35}$$

where $p(r) = r$. This factor renders the differential equation self-adjoint.

Inserting g_{mn} in equation (5.30) gives the representation of the Green's function for a coaxial cylindrical cavity represented through modified Bessel functions:

$$G(r, \phi, z; r', \phi', z') =$$
$$= \frac{1}{\pi L}\sum_{m=0}^{\infty}\sum_{n=1}^{\infty}(2-\delta_{m0})\cos[m(\phi-\phi')]\sin(\beta_n z)\sin(\beta_n z')\,\frac{R_{mn\,1}(r_<)R_{mn\,2}(r_>)}{I_m(\beta_n a)K_m(\beta_n b) - I_m(\beta_n b)K_m(\beta_n a)}. \tag{5.36}$$

Another method which leads to the same solution can be found in [71].

5.1.3 Green's function represented through modified Bessel functions of imaginary order and real argument

The two previous representations of the Green's function were based on particular solutions with discontinuous first derivative in z, eq.(5.23), or in r, eq.(5.36). The existence of a third kind of solution which displays this behavior in ϕ is mentioned in [75, p.34]. Since in this reference this solution is given for the free space problem only, we derive the corresponding solution for the coaxial cavity as follows.

As discussed in chapter 5.1, another kind of solution can be obtained separating the potential equation in cylindrical coordinates differently. For example, case IV in equation 5.6 leads to

$$\left(\frac{\partial^2}{\partial\phi^2} - \alpha^2\right)\bar{\Phi} = 0, \tag{5.37}$$
$$\left(\frac{\partial^2}{\partial z^2} + \beta^2\right)Z = 0, \tag{5.38}$$
$$\left[\frac{\partial^2}{\partial r^2} + \frac{1}{r}\frac{\partial}{\partial r} - \left(\beta^2 - \frac{\alpha^2}{r^2}\right)\right]R = 0. \tag{5.39}$$

With $\alpha =: i\mu$ and $\mu \in \mathrm{R}$ the general solutions are

$$\bar{\Phi}(\phi) = A\cosh(\alpha\phi) + B\sinh(\alpha\phi), \tag{5.40}$$
$$Z(z) = C\cos(\beta z) + D\sin(\beta z), \tag{5.41}$$
$$R(r) = EK_{i\mu}(\beta r) + FL_{i\mu}(\beta r). \tag{5.42}$$

The modified Bessel functions are of imaginary non-integer order but with real argument. Case III would lead in a similar way to ordinary Bessel functions of imaginary order. In contrast to case IV, the numerical evaluation of these functions are uncommon apart from the fact that the zeros of real valued linear combinations, which fulfill the boundary condition at $r = b$, are not easy to be found. This case therefore will not be discussed.

However, considering the Dirichlet boundary conditions in z we get the same solutions as found in the previous chapter as well as the discrete eigenvalues of $\beta =: \beta_n = n\pi/L$. The Fourier series representation of the delta distributions in z is then

$$\delta(z-z') = \sum_{n=1}^{\infty} \frac{\sin(\beta_n z)\sin(\beta_n z')}{N_{mn}^2} \qquad \text{with} \qquad N_{nm}^2 = \int_0^L \sin^2(\beta_n z)\; dz = \frac{L}{2}. \tag{5.43}$$

The radial solution is expressed by modified Bessel functions of imaginary order. As discussed in [76] and [77], it is better from the point of view of numerical evaluations to use $K_{i\mu}(\beta r)$ and its satisfactory companion $L_{i\mu}(\beta r)$ defined by

$$L_{i\mu}(\beta r) := \frac{1}{2}\big(I_{-i\mu}(\beta r) + I_{i\mu}(\beta r)\big), \tag{5.44}$$

as the solutions of the modified Bessel differential equation (5.39); they are real valued functions if both $r > 0$ and μ are real.

In order to fulfill the boundary conditions in r, we chose an ansatz similar to that used in subsection 5.1.1.

$$R_n(r) = L_{i\mu}(\beta_n a) K_{i\mu}(\beta_n r) - K_{i\mu}(\beta_n a) L_{i\mu}(\beta_n r). \tag{5.45}$$

By its definition this function fulfills the boundary condition at $r = a$. Since $\beta_n = n\pi/L$ is already discrete from the Dirichlet boundary conditions in z, discrete values of μ must be determined to satisfy the Dirichlet condition at $r = b$. The imaginary value $i\mu_{nk}$, which represents the order of the Bessel functions, is the k-th zero of the following real function of the real variable μ:

$$R_{nk}(\mu_{nk}; a, b) = L_{i\mu}(\beta_n a) K_{i\mu}(\beta_n b) - K_{i\mu}(\beta_n a) L_{i\mu}(\beta_n b) = 0. \tag{5.46}$$

The roots are calculated by Newton's method; approximate starting values are found from plots, as, for example, the plot of function (5.45) versus the imaginary order μ for a fixed argument with $r = b$; it is given in figure 5.2. If used in function (5.45), these zeros fulfill the boundary condition at $r = b$ as is shown in figure 5.3.

The Fourier series representations of the delta distributions for r is then

$$r\;\delta(r-r') \;=\; \sum_{k=1}^{\infty} \frac{R_{nk}(r) R_{nk}(r')}{N_{nk}^2}, \tag{5.47}$$

where the radial functions $R_{nk}(r)$ fulfill the following orthogonality condition:

$$\int_a^b R_{nk}(r)\; R_{ns}(r) \frac{dr}{r} \;=\; \delta_{ks}\; N_{nk}^2 \tag{5.48}$$

with the normalization constant N_{nk}^2. An analytic expression for this constant is derived in [66]. However, the resulting expression comprises derivatives of the Bessel functions with respect to the order, which are difficult to compute, in general; of course, this task may be accomplished with the help of *Mathematica*. But it is more convenient to compute these constants by numerical evaluation of the integral given above for k = s.

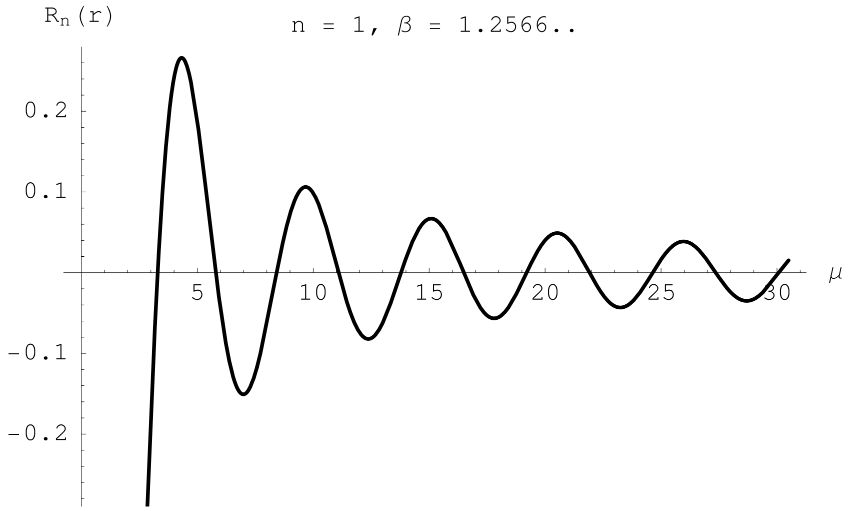

Figure 5.2: The radial function $R_n(b)$, eq.(5.45), versus imaginary order $i\mu$. n $= 1$, $\beta_n = n\pi/L = 1.25664...$ m^{-1}, $L = 2.5$ m, $a = 0.8$ m, $b = 2.53$ m. One can see the zeros $\mu_{1,1} = 3.29224,\ \mu_{1,2},\ \mu_{1,3}, ...,\ \mu_{1,10},\ \mu_{1,11}$.

At first the z-dependence of the wanted Green's function is ignored. So we have a fixed given value of β_n, whose subscript is omitted. So only the 2-dimensional Green's function is represented as

$$G(r,\phi;r',\phi') \;=\; \sum_{k=1}^{\infty} \frac{R_{nk}(r)R_{nk}(r')}{N_{nk}^2}\; g_k(\phi,\phi'). \tag{5.49}$$

This expansion and that for $r\ \delta(r-r')$ are inserted into the differential equation for the Green's function:

$$\Delta\, G \;-\; \beta^2 G \;=\; -\frac{1}{r}\ \delta(r-r')\ \delta(\phi-\phi'), \tag{5.50}$$

$$\left[\frac{\partial^2}{\partial r^2} \;+\; \frac{1}{r}\,\frac{\partial^2}{\partial r^2} \;+\; \frac{1}{r^2}\,\frac{\partial^2}{\partial \phi^2} \;-\; \beta^2\right] G \;=\; -\,\frac{1}{r^2}\ \delta(\phi-\phi')\sum_{k=1}^{\infty}\frac{R_{nk}(r)R_{nk}(r')}{N_{nk}^2}. \tag{5.51}$$

The differential equation for the radial functions gives:

$$\left[\frac{\partial^2}{\partial r^2} \;+\; \frac{1}{r}\,\frac{\partial^2}{\partial r^2}\right] R_{nk}(r) \;=\; \left[\beta^2 \;-\; \frac{\mu_k^2}{r^2}\right] R_{nk}(r). \tag{5.52}$$

So, we get the following system of differential equations for the azimuthal part of the Green's function:

$$\left(\frac{d^2}{d\phi^2} \;-\; \beta^2\right) g_k(\phi,\phi') \;=\; -\ \delta(\phi-\phi'). \tag{5.53}$$

Using the Fourier series expansion for the delta distribution $\delta(\phi-\phi')$ we find:

$$g_k(\phi,\phi') \;=\; \frac{1}{2\pi}\sum_{m=-\infty}^{\infty}\frac{1}{\mu_k^2 \;+\; m^2}\ e^{im(\phi-\phi')} \tag{5.54}$$

$$\;=\; \frac{1}{2\mu_k}\frac{\cosh[\mu_k(\pi-|\phi-\phi'|)]}{\sinh(\mu_k\ \pi)}, \qquad 0 \le |\phi-\phi'| \le 2\pi. \tag{5.55}$$

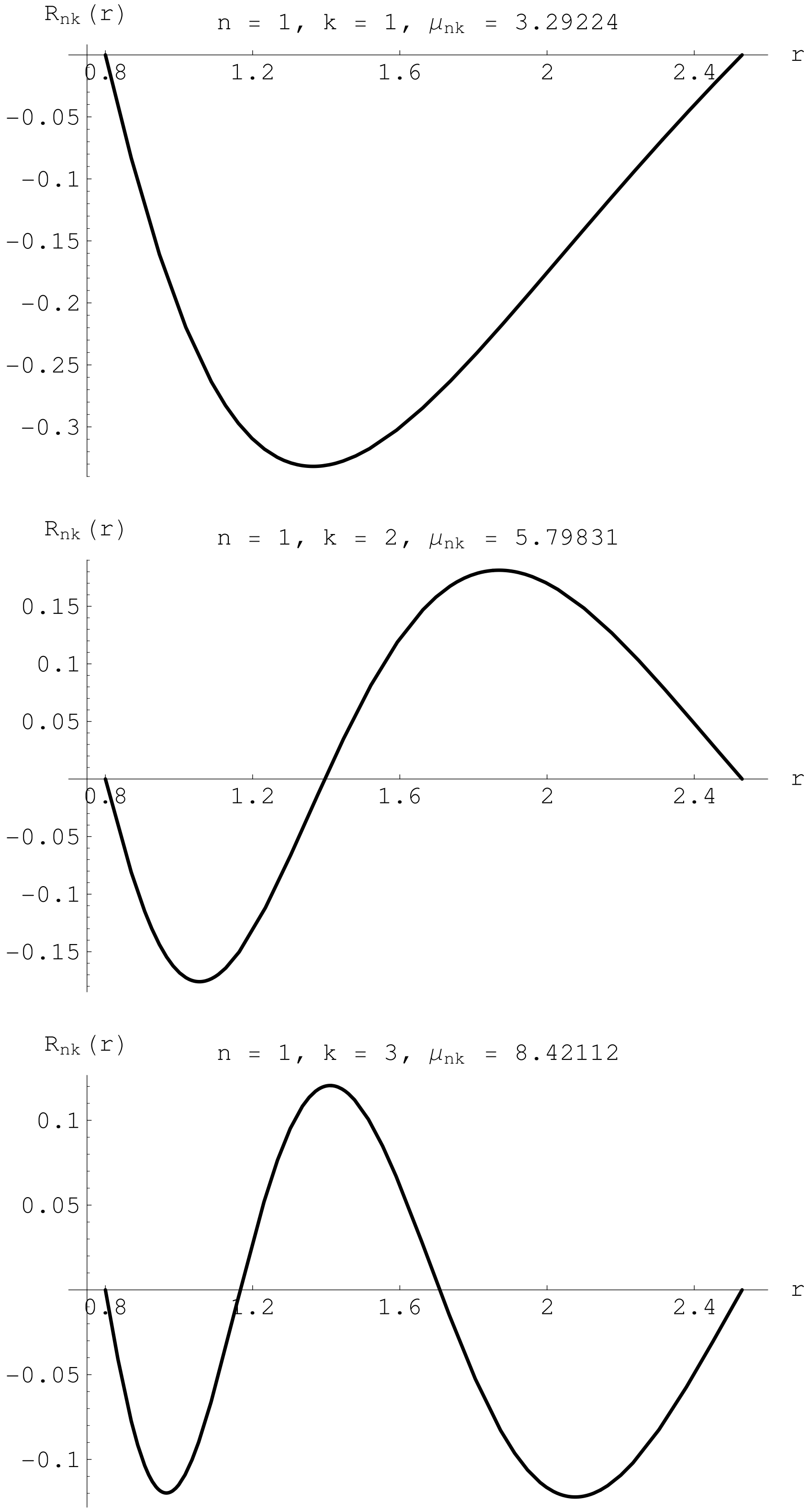

Figure 5.3: The radial functions $R_{n,k}(r)$, eq.(5.45), versus r for the three values $\mu_{1,1}$, $\mu_{1,2}$, $\mu_{1,3}$. $k-1$ gives the number of nodes in the interior of the interval [a,b]. n = 1, $\beta = n\pi/L = 1.25664..\ \mathrm{m}^{-1}$, $L = 2.5$ m, $a = 0.8$ m, $b = 2.53$ m.

The last line is obtained by summing the series occurring in the first line by residues, [78] or [70]. This leads in a straightforward way to the expression and the interval wherein it is valid. A graphical representation of how g_k fulfills the periodic boundary conditions within the interval $[0, 2\pi]$ is given in figure 5.4.

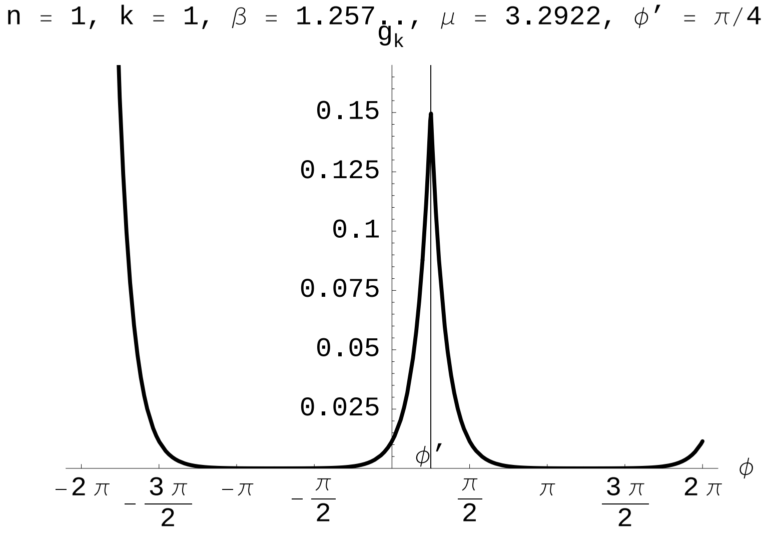

Figure 5.4: The azimuthal part $g_k(\phi, \phi')$, eq.(5.55), of the Green's function versus ϕ for $\mu = \mu_{1,1}$ and $\phi' = \pi/4$. n = 1, $\beta = n\pi/L = 1.25664...\ \mathrm{m}^{-1},\ L = 2.5$ m, $a = 0.8$ m, $b = 2.53$ m.

The final expression for the wanted two-dimensional Green's function is:

$$G(r, \phi; r', \phi') = \sum_{k=1}^{\infty} \frac{R_{nk}(r) R_{nk}(r')}{N_{nk}^2} \frac{1}{2\mu_k} \frac{\cosh[\mu_k(\pi - |\phi - \phi'|)]}{\sinh(\mu_k\ \pi)}. \tag{5.56}$$

The extension to the three-dimensional case is obvious. The knowledge of this function as well as formulas (5.43) and (5.47) allow us to write down the Green's function for a coaxial cavity represented through modified Bessel functions with imaginary order:

$$G(r, \phi, z; r', \phi', z') = \frac{1}{L} \sum_{k=1}^{\infty} \sum_{n=1}^{\infty} \frac{\cosh[\mu_{nk}(\pi - |\phi - \phi'|)]}{\mu_{nk} \sinh(\pi \mu_{nk})} \sin(\beta_n z) \sin(\beta_n z') \frac{R_{nk}(r) R_{nk}(r')}{N_{nk}^2}. \tag{5.57}$$

A representation of the Green's function equivalent to that given in eq.(5.56) may also be derived from the two-dimensional Green's function obtained from eq.(5.36) by omitting the dependence on the longitudinal coordinate z through a Watson (or Sommerfeld-Watson) transformation. This is worked out in the appendix of [66].

5.1.4 Convergence improvement close to the point charge

All three solutions derived so far are hampered by slow convergence properties close to the point charge itself. If combined, they represent a powerful tool to calculate the resulting potential anywhere but close to the point charge. Several numerical calculations showed that the thickness of the cursed volumes as shown in figure 5.6 decrease rapidly with increasing summation limit. A summation limit of 40 was found to be sufficient to calculate the Green's function with sufficient accuracy outside of a volume 0.05 m thick within the current (ALICE TPC) geometry. However, one might need a fast converging solution close to the point charge itself, therefore remedies as proposed in [72] are used to derive such a representation.

By looking at the Green function represented through ordinary Bessel functions (5.23) we find the part of the hyperbolic functions to be the decisive term for the convergence.

$$\begin{aligned} g_0(\beta) = \frac{\sinh(\beta z_<)\sinh(\beta(L-z_>))}{\sinh(\beta L)} &= \\ &= \frac{e^{-\beta(z_>-z_<)} - e^{-\beta(z_>+z_<)} - e^{-\beta(2L-z_>-z_<)} + e^{-\beta(2L-z_>+z_<)}}{2(1-e^{-2\beta L})}. \end{aligned} \tag{5.58}$$

Expressing the hyperbolic part via exponential terms the above written representation can be obtained by multiplication with a term like $e^{-\beta L}/e^{-\beta L}$. The first, second and third exponential in the numerator are responsible for the slow convergence. Directly at the point charge $z = z'$ as well as at the dangerous boundaries in z direction, $z = z' = 0$ or $z = z' = L$, this expression would, for increasing β, lead to 1/2. That means within the $z = z'$ plane it can not contribute to the global converge anymore.

As is shown in [72], the following method can be used in order to get a better behaved representation. By simply subtracting a term of exponentials this behavior can be cured:

$$\begin{aligned} g_s = g_0 - \frac{1}{2}\left[e^{-\beta(z_>-z_<)} - e^{-\beta(z_>+z_<)} - e^{-\beta(2L-z_>-z_<)}\right] &= \\ &= \frac{e^{-\beta(2L-z_>+z_<)} + e^{-\beta(2L+z_>-z_<)} - e^{-\beta(2L+z_>+z_<)} - e^{-\beta(4L-z_>-z_<)}}{2(1-e^{-2\beta L})}. \end{aligned} \tag{5.59}$$

If using g_s instead of g_0 the series is converging rather fast. The correction of these additional terms can be done by using analytical expressions for an infinite (non-closed) coaxial geometry. Such integral representations can be found in [73]. Now, every additional exponential term represents a point charge in a infinite double cylinder which can be seen through looking at the limits of the rewritten solution in z direction. For convenience, instead of the boundaries 0 and L we are using h_1 and h_2. For $h_{1,2} \to \pm\infty$ we get

$$\lim_{h_{1,2}\to\infty} \frac{\sinh(\beta(h_1-z_<))\sinh(\beta(h_2-z_>))}{\sinh(\beta(h_1-h_2))} = \frac{1}{2}e^{-\beta(z_>-z_<)} = \frac{1}{2}e^{-\beta|z-z'|},$$

$$\begin{aligned} G_C(r,\phi,r',\phi',\alpha) &= G_F(r,\phi,r',\phi',\alpha) + H_C(r,\phi,r',\phi',\alpha) \\ &= \frac{1}{4\pi}\frac{1}{\sqrt{r^2 - 2rr'\cos(\phi-\phi') + r'^2 + \alpha^2}} - \dots \\ - \frac{1}{2\pi^2}\sum_{m=0}^{\infty}\epsilon_m\cos[m(\phi-\phi')] &\int_0^\infty d\lambda\cos(\lambda\alpha)\left[I_m(\lambda r)c_m(\lambda) + K_m(\lambda r)d_m(\lambda)\right]. \end{aligned} \tag{5.60}$$

$$\begin{aligned}\text{with} \qquad \epsilon_m &= (2-\delta_{m0}) \\ c_m(\lambda) &= K_m(\lambda b) R_m(a,r')/N_m \\ d_m(\lambda) &= I_m(\lambda a) R_m(r',b)/N_m \\ R_m(s,t) &= I_m(\lambda s) K_m(\lambda t) - I_m(\lambda t) K_m(\lambda s) \\ N_m &= I_m(\lambda a) K_m(\lambda b) - I_m(\lambda b) K_m(\lambda a).\end{aligned}$$

The expression $\alpha = z_> - z_<$ is independent of its sign since within the term of the point charge in free space it is α^2 and within the correction term it appears within the cosine function, which is symmetric. For that reason we can use $\alpha = z - z'$ instead.

In equation (5.60), the first term is simply the solution of the potential equation for a unit source in free space. The second term is applying the boundary conditions on the surfaces of the double cylinder geometry. This representation converges as long as both r and r' do not coincide with either the inner or outer radius. With the help of these converging representations we can rewrite formula (5.23) with $G_C(r,\phi,r',\phi',\alpha)$ from (5.60) and $g_s(\beta)$ from (5.59).

$$\begin{aligned}&G(r,\phi,z,r',\phi',z') = \\ &\quad = G_C(r,\phi,r',\phi',z-z') - G_C(r,\phi,r',\phi',z+z') - G_C(r,\phi,r',\phi',2L-z-z') + \\ &\qquad + \frac{1}{2\pi}\sum_{m=0}^{\infty}\sum_{n=1}^{\infty}(2-\delta_{m0})\cos[m(\phi-\phi')]\frac{R_{mn}(r)R_{mn}(r')}{N_{mn}^2}\frac{g_s(\beta_{mn})}{\beta_{mn}}. \qquad (5.61)\end{aligned}$$

The analytic solution (5.61) is converging fast close to the unit source in every direction but rather slowly close to the cylinder boundaries. This means that in order to improve the convergence close to the point charge itself, the price of slow convergence at the cylinder boundaries must be accepted.

5.1.5 Results and comparison

All three representations of the Green's function which were derived in the previous chapters are converging rather fast if the point of observation is sufficiently far away from the source point. Basically, all three representations are infinite sums. Each term of such a sum comprises two eigenfunctions with eigenvalues chosen such that they fulfill the Dirichlet boundary conditions. The third factor consists of non-oscillating functions introduced by the method of particular integrals; its first derivative is discontinuous at the manifold where the coordinate of the point of observation coincides with that of the source point. A closer look reveals that just this factor is mainly responsible for the convergence of the infinite sum; but its convergence generating power diminishes as the coordinate of the point of observation approaches that of the source.

In the case of equation (5.23), the eigenfunctions, which have oscillatory character, contribute weakly to the convergence. The singular manifold is the plane $z = z'$. For equation (5.36) we find slow convergence on the cylinder $r = r'$. The third solution (5.57) shows such a behavior in the plane $\phi = \phi'$. Therefore, by choosing judiciously among the representations of the Green's function one can find a representation with converges sufficiently good for all regions of the coaxial cavity except for a neighborhood close to the point charge itself. Thus, methods as discussed in [72] were used in order to derive equation (5.61), where the region of slow convergence was projected onto the cylindrical boundary. However, the cursed region of slow convergence close to the unit source diminishes when the integration over the charge $\rho(r, \phi, z)$ is performed (see section 5.2).

In figure 5.5(a) the behavior of the three main representations is compared in the radial direction while the two other coordinates of the observation point and source point coincide, $z = z'$, $\phi = \phi'$. In this direction, just the solution (5.36) gives good convergence properties. Figure 5.5(b) reveals the same behavior for the third solution (5.57) in the azimuthal direction; whereas figure 5.5(c) shows, that the first representation (5.23) of the Green's function in a coaxial cavity does not have any problems along the longitudinal (z) axis. A schematic overview of the dangerous regions with slow convergence is shown in figure 5.6 where all four solutions are compared to each other.

Figure 5.7 contains a typical example, a contour plot demonstrating the smooth properties (within the plane $z = z'$) of the innovative representation (5.57).

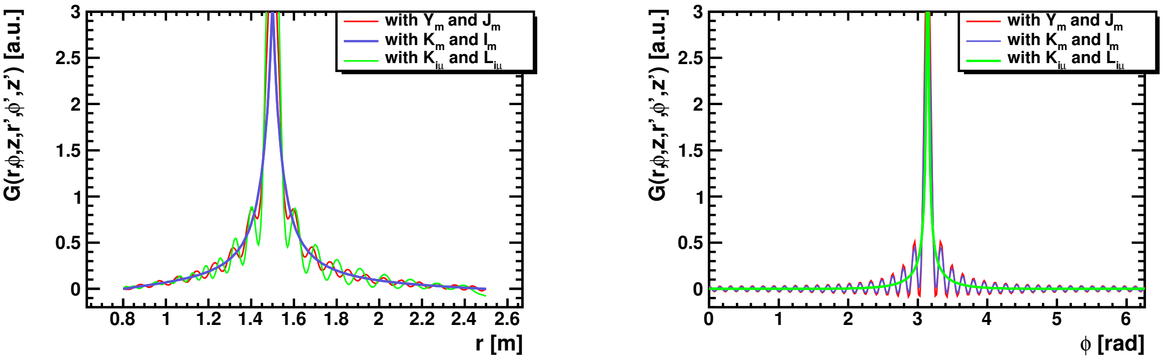

(a) r-dependence with $r' = 1.5$ m ($z = z' = 1.0$ m, $\phi = \phi' = \pi$). Solution (5.36) does not oscillate.

(b) ϕ-dependence with ϕ' at π ($r = r' = 1.5$ m, $z = z' = 1.0$ m). Solution (5.57) does not oscillate.

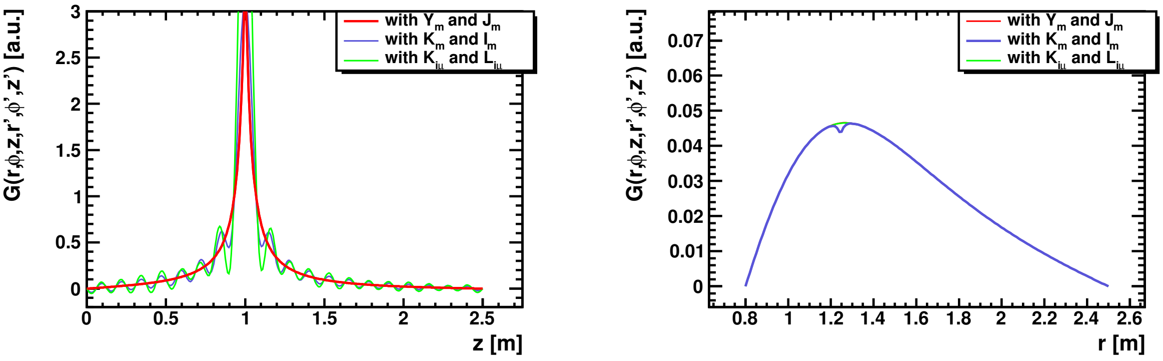

(c) z-dependence with z' at 1.0 m ($r = r' = 1.5$ m, $\phi = \phi' = \pi$). Solution (5.23) does not oscillate.

(d) r-dependence in a region of fast convergence. The solution overlap and are therefore consistent.

Figure 5.5: Solution (5.23), (5.36) and (5.57) as a function of main axis crossing the position of the unit source. The summation limits for m, n and k were set to 40.

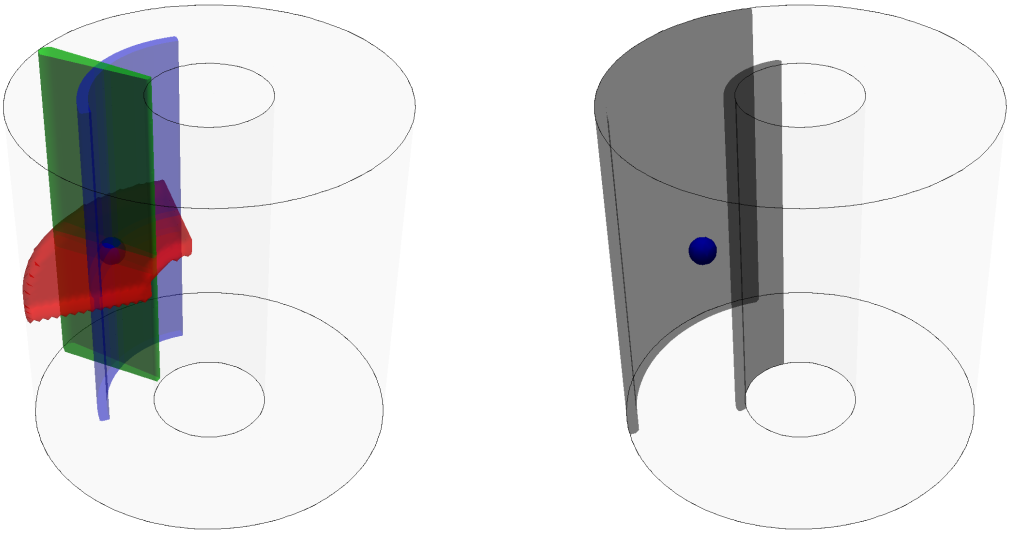

Figure 5.6: Cursed regions of the Green's functions: RED: $z = z'$, representation through ordinary Bessel functions (5.23); BLUE: $r = r'$, representation through modified Bessel functions (5.36); GREEN: $\phi = \phi'$, representation through modified Bessel function of imaginary order (5.57); GRAY: $r = a$ and $r = b$, representation with improved convergence close to the point charge (5.61).

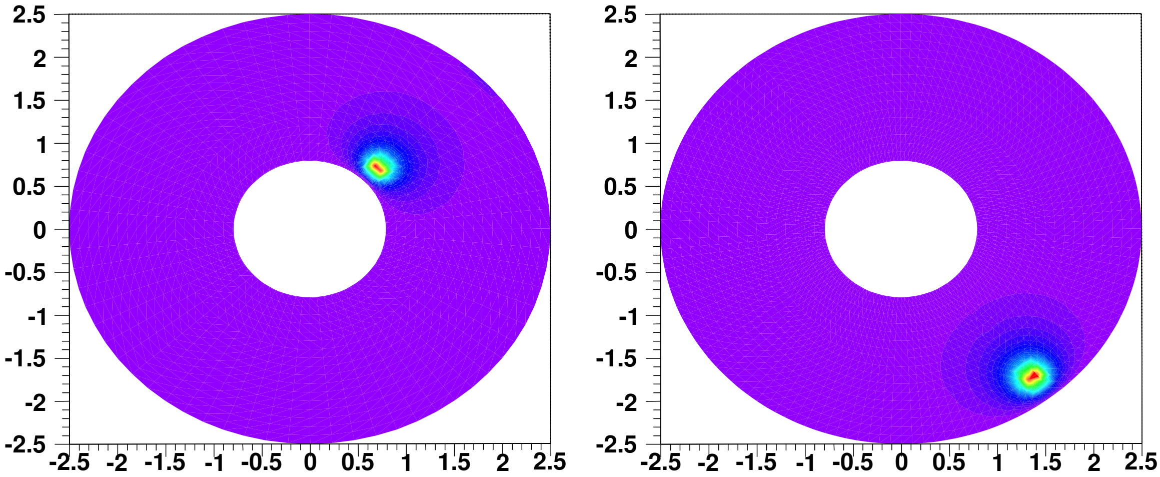

Figure 5.7: Potential due to a point charge in the $(r, \phi)-$plane plotted with Green's function (5.57) at $z = z'$; summation limits set to 40; $a = 0.8$ m, $b = 2.53$ m. Point-charges placed in arbitrary positions.

Only the Green's function (5.36) is known from the literature [71] which just allowed a convergent representation for the electrical field in the radial direction. The other representation (5.23) is rather similar as far as the derivation is concerned but it does allow only a convergent representation of the electric field in the longitudinal direction. The third representation derived in this chapter (5.23) is a completely new and innovative representation of a Green's function within a coaxial cavity. It renders a convergent infinite sum for the electrical field in the azimuthal direction.

Together, the three representations presented in here finally permit the treatment of any space charge distribution within a coaxial cavity, and not only radially symmetrical ones. Combined, they yield convergent series representations for the potential as well as for the electric field in every direction almost everywhere within a coaxial cavity. Section 5.2 contains the fast converging representations for every electrical field component as well as a fast evaluation model which is used for space charge calculations for the ALICE TPC.

Corresponding Green's functions for a rather untypical TPC geometry as that used for the PANDA experiment [79, p.115] require a modification of the boundary conditions in the azimuthal (ϕ) direction. The corresponding Green's functions, plots which display the slow convergence regions as well as certain electrical field plots at chosen representative positions, are given in appendix A

5.2 Electrical field due to an arbitrary space charge distribution

In order to calculate the potential or the electrical field components as excited by an arbitrary space charge configuration within the coaxial cavity (TPC geometry), the following principle is the most common one.

The potential due to a charge cloud (space charge) $\rho_c(r', \phi', z')$ can be evaluated via

$$\Phi(r, \phi, z) = \frac{1}{\epsilon_0} \int r'\, dr' \int d\phi' \int dz' \;\; \rho_c(r', \phi', z') \cdot G(r, \phi, z, r', \phi', z'), \tag{5.62}$$

wherein ϵ_0 is the permittivity of free space. The corresponding electrical field components are the corresponding derivatives

$$E(r, \phi, z) = -\nabla\Phi(r, \phi, z) = -\frac{1}{\epsilon_0} \int r'\, dr' \int d\phi' \int dz' \;\; \rho_c(r', \phi', z') \cdot \nabla G(r, \phi, z, r', \phi', z'). \tag{5.63}$$

5.2.1 Electric field due to a point charge

The three Green's functions derived in section 5.1 can be used to calculate the electric field components. Due to the specific convergence properties of each single representation, a fast converging formula for every electrical field component (E_r, E_ϕ, E_z) can be written as follows.

Derivative of G in longitudinal (z) direction

Calculating the derivatives of solution (5.23), which is the representation using ordinary Bessel functions, leads to a converging expression for the field in the longitudinal direction, E_z, but reveals problems in the radial (r) and the azimuthal (ϕ) direction. The converging expression for the electrical field component E_z can be written as:

$$\frac{\partial}{\partial z}G(r,\phi,z,r',\phi',z') =$$
$$\frac{1}{2\pi}\sum_{m=0}^{\infty}\sum_{n=1}^{\infty}(2-\delta_{m0})\cos[m(\phi-\phi')]\frac{R_{mn}(r)R_{mn}(r')}{N_{mn}^2}\frac{\partial}{\partial z}\left(\frac{\sinh(\beta_{mn}z_<)\sinh(\beta_{mn}(L-z_>))}{\beta_{mn}\sinh(\beta_{mn}L)}\right), \tag{5.64}$$

$$\text{with}\quad \frac{\partial}{\partial z}\left(\sinh(\beta_{mn}z_<)\sinh(\beta_{mn}(L-z_>))\right) =$$
$$= \begin{cases} \beta_{mn}\cosh(\beta_{mn}z)\sinh(\beta_{mn}(L-z')), & \text{for } 0\le z<z'\le L,\\ -\beta_{mn}\cosh(\beta_{mn}(L-z))\sinh(\beta_{mn}z'), & \text{for } 0\le z'<z\le L.\end{cases}$$

In here, the additional (increasing) factor β_{mn} in the numerator of the derivative of the longitudinal term would lead to a diverging expression. This divergence is intercepted by the factor β_{mn} within the denominator of the longitudinal term in (5.64). Unfortunately, no such compensating factors exist for the radial and azimuthal terms. For example, the additional (increasing) summation indices m in the numerator of the azimuthal cosine expression, which occurs when calculating the derivative in the ϕ direction, destroys the convergence of the sum for the E_ϕ component. For that reason, we use the other representations of the Green's function to express the electric field components in the radial and the azimuthal direction.

Derivative of G in radial (r) direction

Due to the non-oscillating behavior of the term in the radial direction within solution (5.36), which makes use of modified Bessel function, a non-diverging expression for the field in the radial direction, E_r, can be expressed as shown in equation (5.65).

$$\frac{\partial}{\partial r}G(r,\phi,z,r',\phi',z') =$$
$$\frac{1}{\pi L}\sum_{m=0}^{\infty}\sum_{n=1}^{\infty}(2-\delta_{m0})\cos[m(\phi-\phi')]\sin(\beta_n z)\sin(\beta_n z')\frac{\partial}{\partial r}\left(\frac{R_{mn\,1}(r_<)R_{mn\,2}(r_>)}{I_m(\beta_n a)K_m(\beta_n b)-I_m(\beta_n b)K_m(\beta_n a)}\right), \tag{5.65}$$

$$\text{with}\quad \frac{\partial}{\partial r}\big(R_{mn\,1}(r_<)R_{mn\,2}(r_>)\big) = \begin{cases} R'_{mn}(a,r)R_{mn\,2}(r'), & \text{for } a\le r<r'\le b,\\ R_{mn\,1}(r')R'_{mn}(b,r), & \text{for } a\le r'<r\le b,\end{cases}$$

wherein $R'_{mn}(s,t)$ is

$$R'_{mn}(s,t) = \frac{\beta_n}{2}\left(K_m(\beta_n s)\big(I_{m-1}(\beta_n t)+I_{m+1}(\beta_n t)\big)+I_m(\beta_n s)\big(K_{m-1}(\beta_n t)+K_{m+1}(\beta_n t)\big)\right).$$

The attempt to use solution (5.36) to derive a converging expression for fields in the azimuthal and longitudinal directions fails due to the increasing indices m and β_n within the arguments of the first two terms, which are not compensated by any factors in the denominators. The resulting expressions diverge with increasing summation indices.

Derivative of G in azimuthal (ϕ) direction

The third representation as shown in equation (5.57), which uses modified Bessel function of imaginary order, leads to a converging expression for the electric field in the ϕ direction, whereas the derivatives in radial or longitudinal direction do diverge due to the reasons already mentioned.

$$\frac{\partial}{\partial \phi} G(r,\phi,z,r',\phi',z') = \\ \frac{1}{L}\sum_{k=1}^{\infty}\sum_{n=1}^{\infty} \sin(\beta_n z)\sin(\beta_n z')\frac{R_{nk}(r)R_{nk}(r')}{N_{nk}^2}\frac{\partial}{\partial\phi}\left(\frac{\cosh[\mu_{nk}(\pi-|\phi-\phi'|)]}{\mu_{nk}\sinh(\pi\mu_{nk})}\right) \qquad (5.66)$$

$$\text{with} \quad \frac{\partial}{\partial\phi}\left(\cosh[\mu_{nk}(\pi-|\phi-\phi'|)]\right) = \\ = \begin{cases} -\mu_{nk}\sinh[\mu_{nk}(\pi-(\phi-\phi')), & \text{for } 0\le\phi'<\phi\le 2\pi \\ \mu_{nk}\sinh[\mu_{nk}(\pi-(\phi'-\phi)), & \text{for } 0\le\phi<\phi'\le 2\pi \end{cases}$$

In summary, each representation of the Green's function derived in section 5.1 has its specific application by providing a fast converging expression for one specific electric field component in cylindrical coordinates (E_r, E_ϕ, E_z). Thus, they finally permit the treatment of any truly three-dimensional space charge distribution $\rho(r,\phi,z)$ within a TPC field cage, and not only radially symmetric ones.

Electric field due to a radially symmetric charge

The field components E_r and E_z due to a charged ring at an arbitrary position (r', z') can simply be calculated via equation (5.64) or (5.65) by means of skipping the azimuthal summation over m. The summation indices m can be set to zero. The azimuthal field component E_ϕ is anyway zero due to the radial symmetric nature of the problem.

When applying a radial symmetric charge $\rho(r', z')$ within a certain volume $(\Delta r, \Delta z)$, the resulting field configurations can be simply calculated by integrating over dr and dz.

These solutions can be used to crosscheck the results as obtained via Finite Element methods, which are almost always limited to such two-dimensional (radially symmetric) cases due to computational reasons.

5.2.2 Electric field due to a constant charge within a POC volume

The fields due to a space charge distribution are calculated by multiplying the corresponding charge distribution ρ with the Green's function and by integrating over the volume occupied by the charge distribution. When integrating over the complete volume within the coaxial cavity one finds that all three solution, as given in section 5.1, comprise rather fast converging expressions for the electric field components. However, when smaller voxels are demanded the specific convergence properties of each solution start to manifest themselves.

In order to calculate the field components due to a constant charge Q within a defined voxel $(\Delta r, \Delta\phi, \Delta z)$ around a center at (r_0, ϕ_0, z_0) the following solutions are advisable since they comprise fast converging expressions throughout the volume of the coaxial cavity. In the following, we refer to this kind of chosen voxel as POC volume (Piece Of Cake) since it is a curved box using cylinder coordinates. The consant charge density $\rho_Q = Q/V$ is used throughout this subsection wherein V is the volume of the voxel.

However, the general expression for the potential within such a POC volume is

$$\Phi(r,\phi,z) = \frac{1}{\epsilon_0}\int_{r_0-\Delta r/2}^{r_0+\Delta r/2} r'\,dr' \int_{\phi_0-\Delta\phi/2}^{\phi_0+\Delta\phi/2} d\phi' \int_{z_0-\Delta z/2}^{z_0+\Delta z/2} dz'\ \rho_Q \cdot G(r,\phi,z,r',\phi',z'). \quad (5.67)$$

Even for small voxels, a converging expression for the electrical field in longitudinal direction can be expressed with the help of equation (5.64)

$$\begin{aligned} E_z(r,\phi,z,r',\phi',z') &= \frac{1}{\epsilon_0}\int_{r_0-\Delta r/2}^{r_0+\Delta r/2} r'\,dr' \int_{\phi_0-\Delta\phi/2}^{\phi_0+\Delta\phi/2} d\phi' \int_{z_0-\Delta z/2}^{z_0+\Delta z/2} dz'\ \rho_Q \cdot \frac{\partial}{\partial z} G(r,\phi,z,r',\phi',z') \\ &= \frac{\rho_Q}{2\pi\epsilon_0}\sum_{m=0}^{\infty}\sum_{n=1}^{\infty}\int_{\phi_0-\Delta\phi/2}^{\phi_0+\Delta\phi/2} d\phi'(2-\delta_{m0})\cos[m(\phi-\phi')] \int_{r_0-\Delta r/2}^{r_0+\Delta r/2} r'\,dr' \frac{R_{mn}(r)R_{mn}(r')}{N_{mn}^2} \\ &\qquad \int_{z_0-\Delta z/2}^{z_0+\Delta z/2} dz' \frac{\partial}{\partial z}\left(\frac{\sinh(\beta_{mn}z_<)\sinh(\beta_{mn}(L-z_>))}{\beta_{mn}\sinh(\beta_{mn}L)}\right). \quad (5.68) \end{aligned}$$

In here, the integral in the ϕ direction can easily be expressed in analytical form. An analytical expression for the integral in radial direction can be found via hyper-geometric functions ${}_1F_2$ which lead to an expression which is rather unpractical as regards numerical evaluation. Thus it is advisable to use a numerical algorithm for the integration in the radial direction. For the integration in the longitudinal direction, special precautions have to be taken due to the discontinuous properties of the derivative in z. The integration has to be divided into three different regions in z. For these regions, the following analytic expressions for the integral in z can be found. For the sake of simplicity, we write z_L and z_U for the lower and upper integration limits.

$$\int_{z_L}^{z_U} dz' \frac{\partial}{\partial z}\left(\frac{\sinh(\beta_{mn}z_<)\sinh(\beta_{mn}(L-z_>))}{\beta_{mn}\sinh(\beta_{mn}L)}\right) =$$

$$\begin{cases} = \beta_{mn}\cosh(\beta_{mn}z)\cdot(\cosh(\beta_{mn}(L-z_L)) - \cosh(\beta_{mn}(L-z_U)))\,, & \text{for } 0 \le z \le z_L \\[2ex] \begin{array}{c} = -\cosh(\beta_{mn}(L-z_U))\cosh(z\beta_{mn})\beta_{mn} + \\ \beta_{mn}(\cosh(\beta_{mn}(L-z))\cosh(z\beta_{mn}) - \\ \sinh(\beta_{mn}(L-z))\sinh(z\beta_{mn})) + \\ \beta_{mn}(-\cosh(\beta_{mn}(L-z))\cosh(z\beta_{mn}) + \\ \sinh(\beta_{mn}(L-z))\sinh(z\beta_{mn})) \\ -\cosh(\beta_{mn}z_L)\cosh(\beta_{mn}(L-z))(-\beta_{mn}) \end{array} & \text{for } z_L \le z' \le z_U \\[2ex] = -\beta_{mn}\cosh(\beta_{mn}(L-z))\cdot((\cosh(\beta_{mn}z_U) - \cosh(\beta_{mn}z_L))\,, & \text{for } z_U < z' \le L. \end{cases} \tag{5.69}$$

The solutions for the field components in the radial and the azimuthal direction (E_r and E_ϕ) can be found via equations (5.65) and (5.66). Although the non-oscillating terms which comprise the discontinuity in their derivative allow simple expressions for the integrated term in r and ϕ, special precautions have to be taken as well. When using the analytical expressions for these terms, a procedure similar to that shown in equation (5.69) has to be used.

For example, figure 5.8 shows all three electrical field components as derived from formulas (5.65), (5.66) and (5.64) with a constant charge density $\rho_Q = 1$ within a coaxial cavity (position and dimensions are given in the caption). The fields are plotted in the (r,ϕ)-plane at z=1.7 m, where their smoothness properties are displayed. The plots were performed with a summation limit of 30.

5.2.3 Fast evaluation: discretization of the space charge distribution

Although the derived expressions converge rather fast, a numerical evaluation at approximately 7650 points (equal to 10 cm slices within the TPC volume) takes about two minutes of computation time on a common 2.4 GHz stand alone PC. This estimate includes the calculation of all three field components with a summation limit of 30, which is needed to reach an accuracy of 10^{-7}.

In order to improve the calculation time a discretization model was developed which makes use of a precalculated look-up table. This look-up table contains a sequence of field values due to constant charges within a POC volume, as described in the previous subsection. For example, one row within this table holds 7650 field values (e.g. the E$_r$ component) at different positions (fulcrums) as caused by one single POC configuration. The next rows contain the field values due to POC charges at a different position. Therefore, the complete look-up table comprises the sequence of field values due to POC charges at all possible positions within the discretized volume.

Any desired space charge distribution $\rho(r, \phi, z)$ can be discretized with the corresponding sizes of the voxels as they were used to create the look-up table. By doing so, the

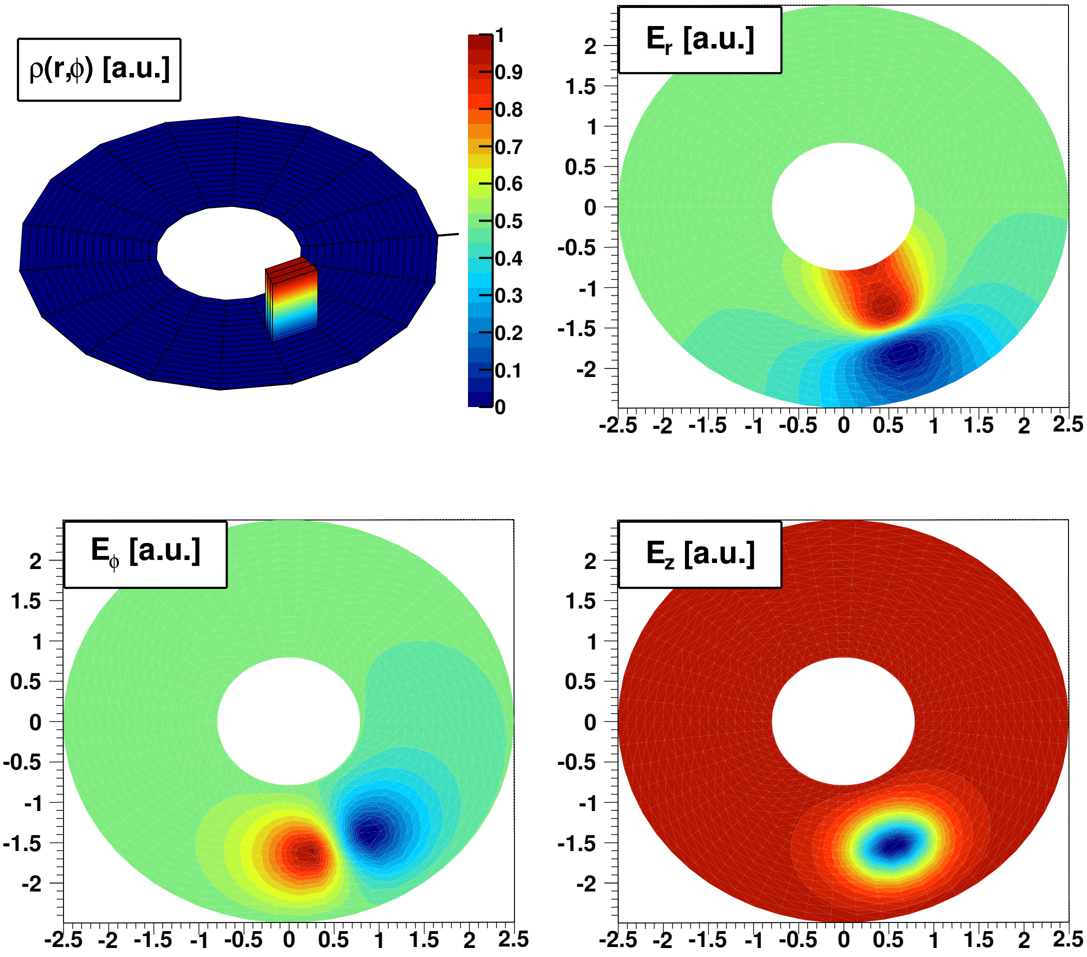

Figure 5.8: E FIELD COMPONENTS DUE TO A CONSTANT SPACE CHARGE DISTRIBUTION within the region $(1.5 \le r \le 1.8, 4.88 \le \phi \le 5.23, 1.0 \le z \le 1.5)$ in the (r, ϕ)-plane at $z = 1.7$. General geometry of the cavity: inner radius $a = 0.8$, outer radius $b = 2.5$, height $h = 2.5$.

voxels obtain a weighting parameter which scales the former charge of $\rho_Q = 1$ into the corresponding average charge density within the voxel. Then, the corresponding fields within the look-up table are scaled with the corresponding weighting parameter (charge density within the voxel) which then results in a simple summation of all weighted configurations as they are stored within the look-up table.

This results in highly accurate values for the field components at the fulcrums for a discretized space charge configuration within the TPC volume. Depending on the size of the look-up table this results in a calculation time of less than one second for all three field components when a discretization of approximately 10 cm voxels was performed. This discretization size was shown to provide sufficient accuracy for the field values at least for space charge fields with linear dependency in z and a $1/r^2$ dependency in r. When comparing the non discretized charge distribution (through integration) with the discretization model (10 cm voxels in a look-up table) relative residuals of less than 10^{-7} were observed.

The next section contains examples on field configurations calculated for simulated space charge distributions. The simulations were performed for the ALICE TPC assuming a pile up of positive ionic charges as caused by consecutive Pb–Pb collisions.

5.3 Expected deviations in high multiplicity events

Once the field distortions were calculated, the resulting distortions of the drifting electron can be obtained by means of solving the Langevin equation (1.3), which corresponds to step 2 in figure 5.1. This solving algorithms were already discussed and used in section 2.2 to simulate distortions due to the inhomogeneous magnetic field but with perfectly constant electric field. Due to the density of space charges in high multiplicity events, also these imperfections of the electric field within the TPC drift volume have to be taken into account.

Another method which equals a first order approximation to obtain the distortions due to imperfect drift fields can be performed via the simple formula (5.70) which gives the radial distortions of a drifting electron starting at (r, ϕ, z):

$$dr(r,\phi,z) = \int_z^0 dz \frac{E_r(r,\phi,z)}{E_{z\ id}}. \tag{5.70}$$

In this formula it is assumed that the distortion of the field in the longitudinal (z) directions is relatively small so that the integration along a straight path in z is valid. Therefore, imperfections in E_z, the field component which complies to the normal drift direction, are ignored. An equivalent formula can easily be found for the distortion in ϕ direction.

A more detailed but computationally more expensive approach is to solve the Langevin equation with methods as described in section 2.3. In there, essentially every effect which results in distortions of the drifting electron can be included. Even non homogeneous drift velocities due to inhomogeneous drift fields (compare chapter 4) can hereby be included. This approach was chosen to calculate the distortions as represented in subsection 5.3.2.

However, before space charge effects can be simulated, the space charge distribution itself has to be estimated, which is done in the following subsection.

5.3.1 Simulated space charge distributions

By using the state-of-the-art simulation code as implemented in the ALICE offline framework [33] it is possible to simulate Pb–Pb collisions via HIJING as well as the propagation of the resulting tracks of charged particles through the detector complex. The traversing tracks as well as their primary ionization potentials within the TPC gas volume can be simulated using the software packages GEANT3 and GEANT4 whereas single TPC hits (representing clusters) can be produced.

The so simulated clusters (positions of primary ionization) can be used to estimate the distribution of positive ions within one event as well as the variations of the ion (space charge) distribution over several events by means of pile up. In chapter 7 of [20], a first estimation regarding such space charge distributions was performed. The numbers used in there were, according to todays knowledge, slightly overestimated. Anyhow, the

Table 5.1: Parameters as used for the TPC space charge simulations.

Drift field E_z	400 V/cm
Magnetic field B_z	0.5 T
Ion mobility μ_{ion} (of Ne$^+$ in Ne)	4 cm^2/Vs
Gas gain G	6.000
Luminosity L	4×10^{26} 1/cm^{2}s
Cross section σ	7.7×10^{-24} cm^2
Center of mass energy (for Pb–Pb)	5.5 TeV
Monte Carlo data identifier	LHC08d6
Event rate	3080 Hz
Central event ratio	≈ 10 %
Ion clearing time	0.156 s
Number of min. bias events per clearing time	480

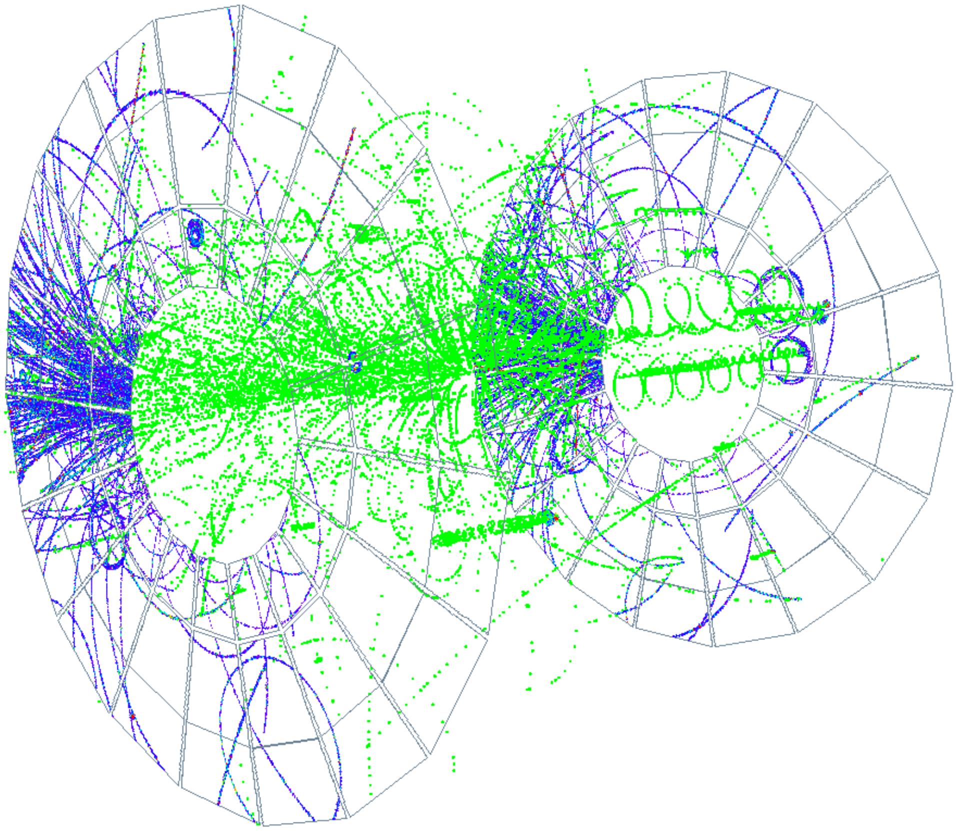

Figure 5.9: TPC SIMULATION OF A NON-CENTRAL PB–PB EVENT. Green dots represent primary ionization along the tracks of charged particles, where positive ions are produced. Blue dots represent ions which are produced in the avalanche of read out electrons within the MWPC.

parameters as they can be found in table 5.1 were used for the present simulations. An example of clusters as found within the TPC for a non-central Pb–Pb event is shown in figure 5.9.

As mentioned in table 5.1, due to the considerably slower ion mobility, approximately 480 minimum bias events (Pb–Pb collisions) contribute to the space charge pile up within the TPC gas volume (considering a ion clearing time of 0.156 s). It is believed that about 10 % of them are central events. However, every single event can contribute to the space charge pile up by means of the following aspects:

1. **PI**: *Primary Ionization* from the tracks within the gas volume.
2. **ROC-IFB**: *Ion Feedback* from tracks within the read-out chamber (from the previous events).
3. **ILK**: *Ion leakage* – typically suppressed by the gating grid.

Due to the difference in mobility (factor of ∼2000), the electrons experience a rather static space charge distribution during one read-out process of ∼100 μs. The expected scenario within the ALICE TPC (PI plus ROC-IFB) would lead to a basically radially symmetric charge distribution. Unexpected major asymmetries in the event topology or problems with the gating grid (e.g. floating gate wires) could destroy the radial symmetry due to additional ion leakage at different positions in the read-out chambers. However, the analytical solution discussed in section 5.1 can be used to handle even non-radially symmetric scenarios.

For the simulated space charge distributions, the produced ions were summed up over 480 minimum bias events whereas the ions were constantly moved towards the Central Electrode. By doing so, the influence of the ion mobility and the event topology could be estimated.

An expected scenario within the ALICE TPC would include the ion sources due to PI and ROC-IFB. This would lead to a basically radially symmetric charge distribution of $\rho(r,z) \approx (3 - 0.9 \cdot z)/r^2 \times 10^{-10}$ C/m^3 which is shown in figure 5.10. Magnitudes of the slope and the zero crossing in z heavily depend on the gain settings and the read-out geometry (by means of ROC-IFB) as well as on the multiplicity of the events. However, the same basic dependency of $1/r^2$ in the radial and a linear dependency in the longitudinal direction were observed in simulations mentioned in [65] and [20, chap.7].

Within the present simulation, a closed-gate-leakage of zero and an open-gate leakage of 20 % were assumed. These numbers correspond to the current MWPC voltage settings and were calculated with Garfield [39]. The corresponding ROC-IFB from clusters created within the read-out chambers is then 10 % when taking a maximal escape time of 180 μs into acount. Therefore, we use a mulitiplication factor of 600 ions per primary electron, which was created within the read-out chamber and follows the multiplication (gain), which drifts back into the volume. Fortunately, the number of clusters created within the ROC (0.7 cm length in z compared to 250 cm of drift length) is rather small. Therefore the effect of ions which drift back into the drift volume is about as large as the space charges produced from primary ionization within the drift volume.

The picture changes dramatically if one assumes a damaged or not effective gating grid at an arbitrary position within the read-out chambers. For example, a floating gate wire can not suppress the back-flow of ions anymore which were created during the avalanche process around the multiplication wire. A corresponding leakage rate between 6 % and

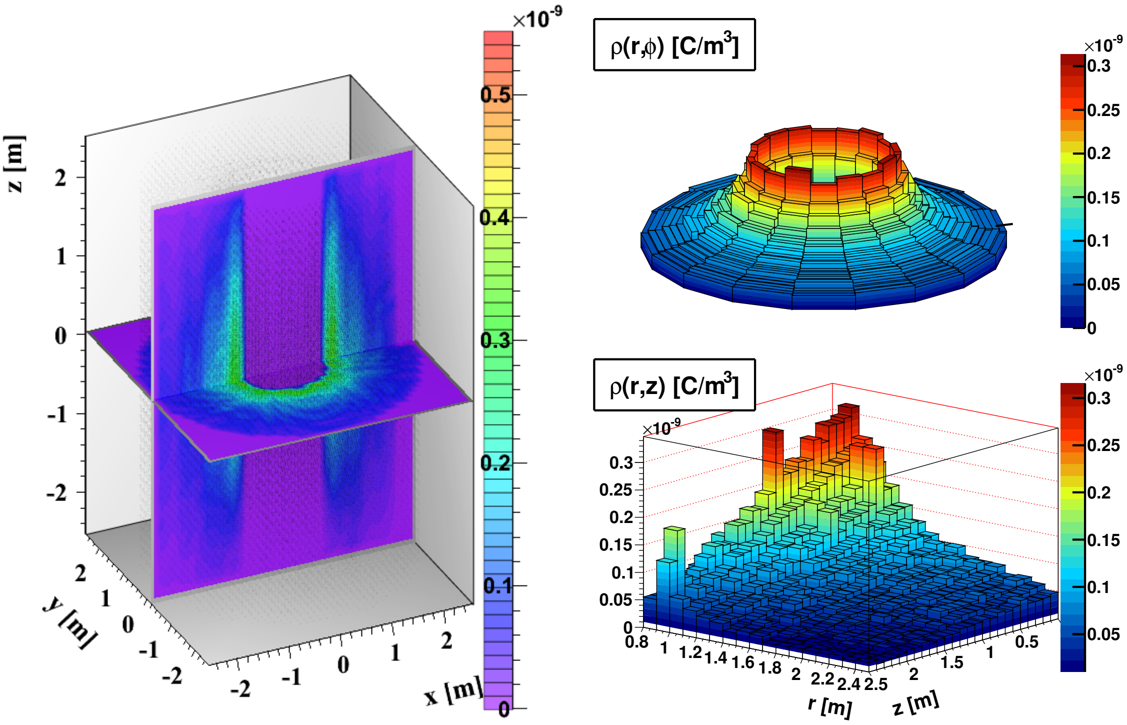

Figure 5.10: Expected space charge scenario for the ALICE TPC. Space charge distribution after a pile up of 480 minimum bias events. Primary ionization and ROC-Ion leakage due to tracks within the ROCs are considered.

20 % (compared to 0 %) was estimated via Garfield simulations. The wide spread of this numbers is due to the alternating nature of the gate voltage settings when the gate is closed. However, in such a case, all the clusters which were produced above the (x,y) position of the floating wire will produce an ion cloud of up to a factor 1200 stronger than the space charge produced due to primary ionization. This additional charge cloud is allowed to drift back into the drift volume due to the non operating gating grid. This effect manifests itself by means of charged slices (factor ∼10) of less than a few centimeters width all along the drift volume, as is shown in figure 5.11.

The corresponding field distortions are calculated via the analytic approach as discussed in section 5.2 using discretized space charge distribution as shown in figures 5.10 and 5.11.

5.3.2 Expected distortions

The calculated electrical field deviations due to the simulated space charge distributions can be used to estimate the consequent space point distortions. When using the approach of solving the Langevin equation numerically (as shortly discussed in the beginning of this section) one is able to predict the corresponding space point distortion in dependence of the initial position (r,ϕ,z) within the TPC volume.

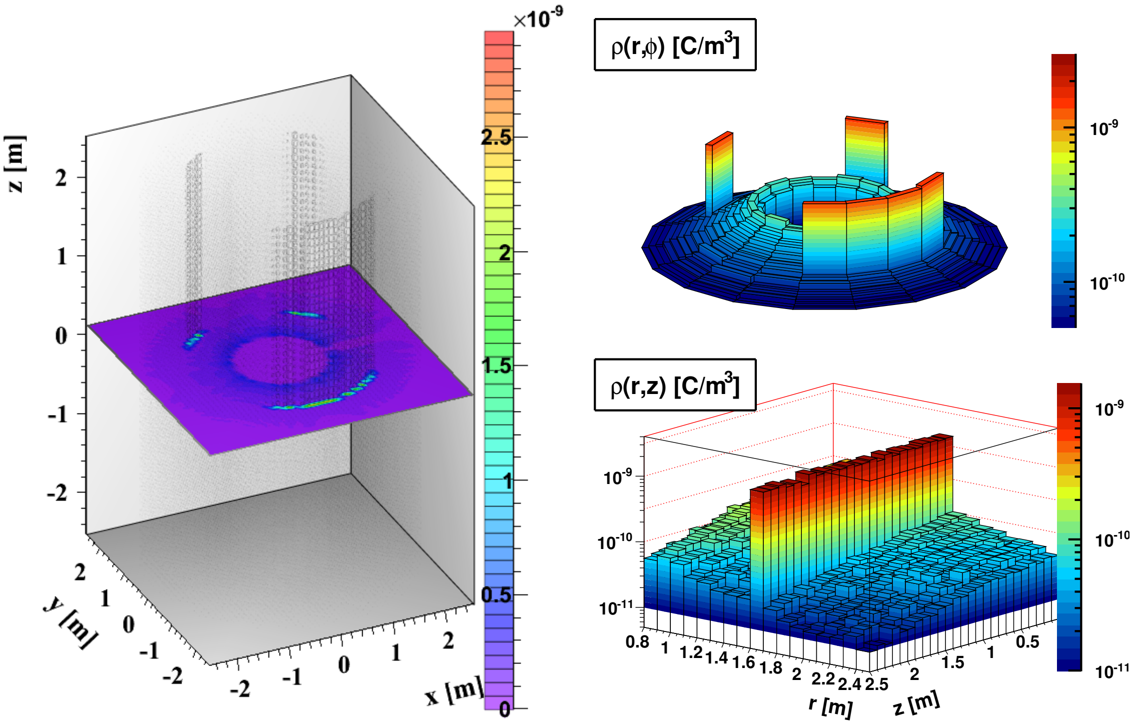

Figure 5.11: SPACE CHARGE SCENARIO WITH FLOATING GATE WIRES. Space charge distribution after a pile up of 480 minimum bias events. Considered are primary ionization, ROC-Ion leakage due to tracks within the ROCs and ion leakage due to non-closed gating grid at arbitrary positions on the TPC A side. *Note:* plots on the r.h.s use a logarithmic scale.

Figure 5.12 contains simulated distortions in radial, azimuthal and longitudinal directions (rows). The left column contains distortions due to a simulated space charge distribution as shown in figure 5.11. The gating grid on the TPC C side ($z<0$) was assumed to work as expected whereas the gating grid on the TPC A side contains floating gate wires at random positions. Without floating wires, the expected space point distortions are radially symmetric (see $z<0$ in figure 5.12(a)). The middle column represents distortions due to magnetic field imperfections (compare section 2.2). The column at right displays the combined effect of the chosen space charge scenario and the measured magnetic field deviations.

Plot 5.12(a) displays the simulated radial distortions due to space charge effects assuming a perfect magnetic field. Clusters close to the outer field cage ($r=250$ cm) are distorted negatively whereas clusters close to the inner field cage are deviated positively. Thus, the clusters are basically focused into the middle of the chambers. Due to the higher charge density at inner radii, the effect at $r=90$ cm is more dominant. The distortions due to B field inhomogeneities, as are shown in plot 5.12(b), were already discussed in section 2.2. The maximum radial deviation in this highly nonlinear structure reached values up to 4 mm. The combined effect of space charge and magnetic field imperfections is shown in figure 5.12(c). In summary, especially close to the inner field cage, the space charge distribution can introduce additional radial distortions of up to 0.8 mm if floating gate wires are not excluded.

Graph 5.12(d) contains azimuthal distortions in cm (obtained by the multiplication with the corresponding radius) due to space charges within the nominal B field. This quantity is denoted as $\Delta(r\phi)$. The distortions attain up to 150 μm for the expected space charge scenario and are therefore negligible in comparison to the azimuthal distortions due to the measured imperfections of the magnetic field which reach values up to 7 mm close to the outer field cage (see graph 5.12(e)). In summary, the azimuthal distortions are dominated by the measured magnetic field imperfections.

Longitudinal distortions are plotted in the last row of figure 5.12. Errors in the z reconstruction without noticeable space charge within the volume could reach up to 20 μm and are therefore negligible. Distortions in z manifest themselves mainly by a non-constant drift velocity due the drift field variations caused by space charges within the drift volume. However, the distortions integrated along the drift path do not exceed 120 μm for space charge scenarios as discussed in the previous subsection.

In general, space charges of noticeable magnitude do have a non-negligible influence on the radial distortions of clusters whereas their azimuthal distorting power is small in comparison to the imperfections of the measured magnetic field within the ALICE TPC. For the simulated space charges, longitudinal distortion due to variations in the drift field and therefore the drift velocity as well as the longer drift path (compared to the straight line) do not exceed 120 μm or 4.6 ps respectively. These deviations are negligible in comparison to dynamic drift velocity variations by means of gas density as discussed in chapter 4.

Therefore, when correcting for space charge effects within the ALICE TPC, mainly radial distortions have to be considered. Without such corrections a systematic error of the momentum measurement as well as systematic shifts of the vertex reconstruction can be expected; their magnitude will be subject of future research. However, the analytic approach as presented in this chapter allows detailed simulations of space charge effects for any space charge distribution one might imagine. Due to the introduced discretization, this method is sufficiently fast to be used in solving the inverse problem, namely calculation of the causing space charge distribution by means of analyzing electrical field distortions (see step 1 in figure 5.1).

But all this will be subject of the next two years, where the ALICE TPC prepares for its first heavy-ion collisions.

Space point deviations in radial (r) direction

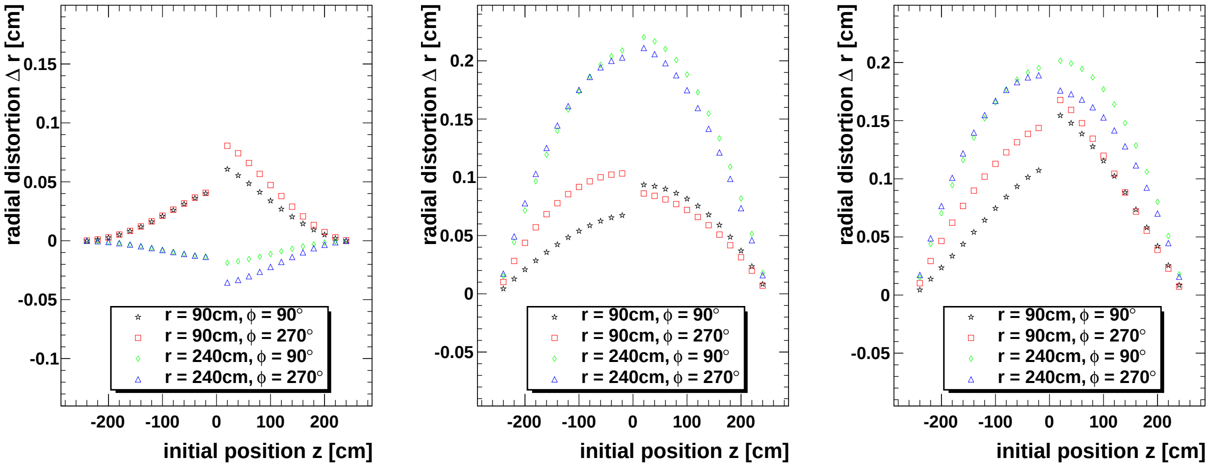

(a) due to E field deviations (space charge with nominal B)

(b) due to B field inhomogeneities (with nominal E)

(c) due to E and B field imperfections

Space point deviations in azimuthal (ϕ) direction

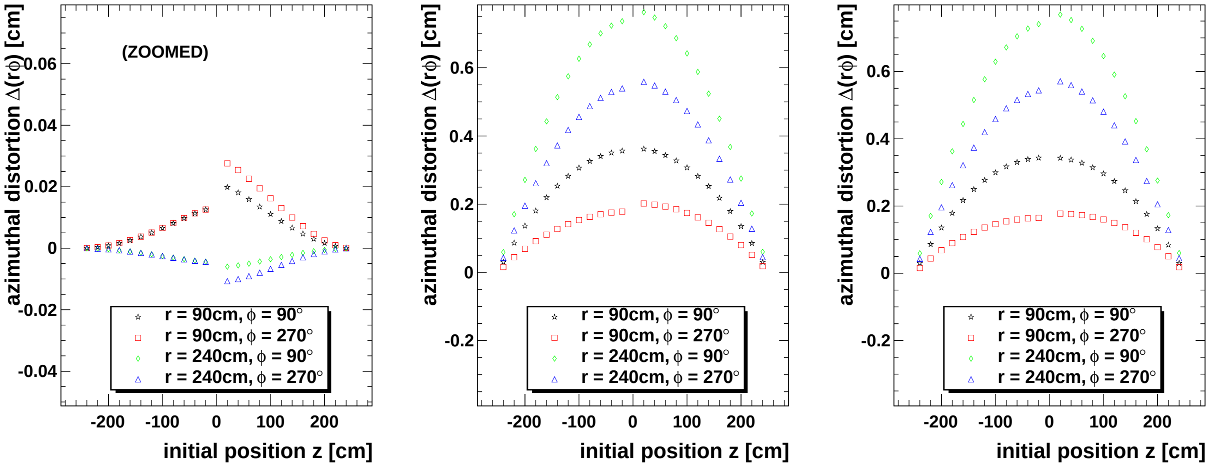

(d) due to E field deviations (space charge with nominal B)

(e) due to B field inhomogeneities (with nominal E)

(f) due to E and B field imperfections

Space point deviations in longitudinal (z) direction

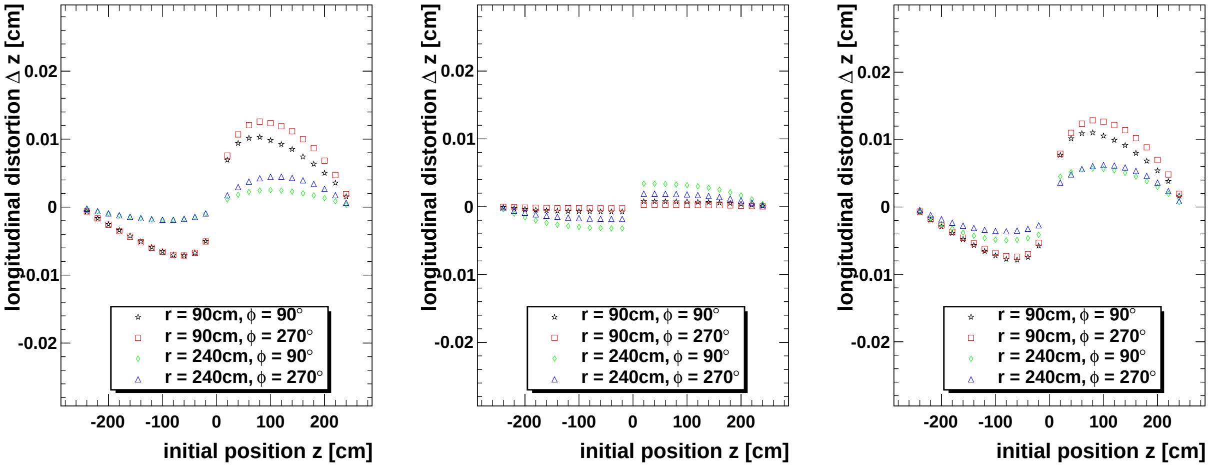

(g) due to E field deviations (space charge with nominal B)

(h) due to B field inhomogeneities (with nominal E)

(i) due to E and B field imperfections

Figure 5.12: Space point deviations due to field inhomogeneities. Calculations were performed for conditions as present in the ALICE TPC. Nominal E field: E_z=400 V/cm, nominal B field: B_z=0.5 T, mean drift velocity v_d=2.58 cm/μs.

Chapter 6

Comprehensive summary

The research presented in this thesis covers all major issues relevant for the final calibration and therefore the improvement of the space point resolution of a Time-Projection Chamber (TPC) by means of identifying systematic influences. The magnitude of influences of static as well as of dynamic imperfections, drawing on the example of the ALICE TPC, are discussed in the corresponding chapters. The subsequent paragraphs represent a comprehensive summary.

Basic gas properties and static imperfections of a TPC, as well as their influence on the electron drift velocity and trajectory, are treated in Chapter 2.

By reviewing the transport properties (drift velocity and diffusion coefficients) in dependence of gas impurities and temperature, the gas composition of Ne-CO_2-N_2 (90/10/5) was confirmed to be the best choice for high luminosity environments as expected in the ALICE TPC. The additional performance requirements, enforced by this gas choice, on the gas distribution system (gas purity and stability) as well as the temperature stability of the overall detector complex, were proven to be under control (see section 4.3 and [41]).

Furthermore, systematic distortions of the electron trajectory due to magnetic field imperfections (up to 2 % for the L3 magnet) are the topic of section 2.2. It was proven that, due to the gas choice, the Langevin approximation of the Lorenz angle is sufficient to calculate the correponding distortions. The maximum distortions in the r direction are in the range of 3 mm, whereas in the ($r\phi$) direction, they attain values up to 7 mm. The current implementation of the E×B correction uses a pre-calculated look-up table, where the corresponding distortions are listed in dependence on the measured cluster position.

Section 2.3 contains the quantification of systematic distortions due to static electric field (drift field) imperfections. The corresponding electrical field within the TPC field cage was modeled by making use of finite-element methods where details such as the field cage strip-structure, the read-out chambers, the covers and the skirt planes could be included. The achieved accuracy of the field calculation is better then 5×10^{-2} V/cm which is more than sufficient for the performed misalignment studies and the calculation of their distorting power. The voltage settings optimized in the process minimize the drift field imperfections within the whole drift volume. The presented calculations were the base of the development of the laser calibration algorithms used during the commissioning phase in August 2009.

Chapter 3 gives an overview of the signal creation and the signal shape within the ALICE TPC read-out. It contains a shape characterization with special emphasis on the ion-tail typical for Multi Wire Proportional read-out chambers as used in the ALICE TPC (section 3.1). Various simulations were performed in order to understand its shape and the underlying physical and geometric dependencies (section 3.2). The simulations showed excellent agreement with the measured mean pulses which allowed an indirect determination of the mean avalanche size around the multiplication wires. Section 3.3 contains details regarding the digital read-out optimization by means of the ALTRO chip. It comprises a prescription how the signal can be shaped and optimized in order to maximize its efficiency for high multiplicity environments.

Dynamic (short and long term) variations of the ambient conditions around the TPC pose additional demands on the calibration of a TPC which mainly influence the electron drift velocity and therefore the z resolution. These effects, their magnitude as well as their parametrization are the topic of chapter 4.

Section 4.1 distinguishes between the different drift velocity dependencies such as pressure, temperature, gas compositions and the applied drift field. The developed parametrization allows a quick estimation of the drift velocity variations as function of the field and gas property changes as found via sensor measurements. The achieved accuracy is 0.05 %, which is sufficient to be used in the first reconstruction pass.

Since temperature stability plays an important role within the ALICE TPC, section 4.2 contains key studies of performed Computational Fluid Dynamics (CFD) simulations. The outcome is that, in general, a linear model is sufficient to parametrize the temperature distribution within the sensitive area of the TPC drift volume. Thus, the temperature sensors, located within the TPC gas volume, can be used to measure the mean temperature as well as the temperature gradient. However, if the temperature sensors located on the inner and outer containment vessels would measure temperature differences of more than 3 °C (in comparison to the drift volume) the non-linear model, as described in this section, should be used in order to achieve a temperature determination of better than $\Delta T \leq 0.1$ °C.

Section 4.3 contains a direct comparison of drift velocities as found via the previously mentioned parametrization, by means of the various sensors (temperature, pressure), and the drift velocities as evaluated with the method of matching the ITS-TPC tracks. One major outcome is that, according to the performed distinction between the different influences, thanks to the achieved temperature stability, the pressure variations are the most dominant contributor to the short and long term drift velocity variations within the ALICE TPC.

Especially for heavy-ion collisions, dynamic field distortions due to space charge pile up are not negligible anymore. Thus, a method had to be developed which is capable of solving the field equations with adjustable inhomogeneous terms represented by varying space charge distributions. Chapter 5 contains the derivation and the validation of novel analytical solutions for a geometry approximating that of a TPC.

In section 5.1, the derivation of such analytical solutions is presented by using the method of Green's functions. For example, the innovative usage of modified Bessel functions of imaginary (and discrete) order allows fast and accurate (non-oscillating) representations of the electrical field component in the ϕ direction. This allows the calculation of field distortions due to any arbitrary truly three-dimensional space charge distribution within a TPC, and not only radially symmetric ones. In combination with the introduced discretization of expected space charge distributions (see section 5.2), this approach finally permits a nearly instant but still precise simulation of additional space point distortions due to field fluctuations in high multiplicity events such as Pb–Pb collisions.

By using state-of-the-art simulation codes as implemented in the ALICE offline framework it is possible to estimate the magnitude of space charge clouds within the TPC drift volume as expected from Pb–Pb collisions. Section 5.3 contains simulated scenarios of space charge distributions which include primary ionization as well as unavoidable ion leakages from the read-out chambers. Such considerations lead to a radially symmetric charge distribution of $\rho(r,z) \approx (3-0.9\cdot z)/r^2 \times 10^{-10}$ C/m^3. The same basic dependency of $1/r^2$ in the radial and an approximately linear dependency in the longitudinal direction was observed in simulations mentioned in [65] and [20, chap.7].

When using the approach of solving the Langevin equation, one is finally able to predict the resulting space point distortions as caused by a non-negligible space charge distribution within a TPC. In addition, the resulting change of the E×B effect can be taken into account quantitatively, as can be other effects such as field cage imperfections and changes of the ambient conditions.

In summary, this thesis covers all major issues relevant to the intended improvement of the space point resolution. Unavoidable and possible systematic deviations of the ideal electron trajectory within TPCs, both of static and dynamic nature, were discussed. The magnitude of their single contributions was identified and correction models were presented. During the commissioning phase of August 2009, it is planned to refine the calibration techniques with cosmic and laser data by making use of higher statistics. These calibration procedures will be fine tuned with the help of the upcoming pp collisions by the end of 2009.

The Pb–Pb collisions planned for the end of 2010 will pose an additional challenge on the calibration techniques regarding space point corrections. Thanks to the analytical approach as presented in the last chapter of this thesis, the ALICE TPC is well prepared to engage this exciting and novel task.

Appendix A

Green's functions for bisected coaxial cavity

In contrast to typical TPCs, the PANDA experiment aims for a TPC which is bisected into two semi-circles in azimuthal direction [79, p.115]. Therefore, the periodic boundary conditions in ϕ direction have to be replaced by a Dirichlet boundary condition:

$$\bar{\Phi}(0) = \bar{\Phi}(\epsilon) = 0, \tag{A.1}$$

whereas ϵ represents the opening angle of one wedge-shaped half of the TPC in the (r, ϕ)-plane. Following the naming convention of the previous chapters, the general dimensions are, inner radius $a = 0.15$ m, outer radius $b = 0.42$ m, length $L = 1.5$ m and opening angle $\epsilon = 170^\circ = 17/18 \cdot \pi$.

In contrast to the periodic boundary conditions in ϕ, as used for the previous derivations of the Green's functions of a coaxial TPC, these Dirichlet conditions do not force the separation constant α to be an integer any more. For the representations as they follow from equation (5.4), the solution of the Helmholtz equation in ϕ can be fulfilled by

$$\bar{\Phi}(\phi) = A_m \sin(\alpha_m \phi), \tag{A.2}$$

with $\alpha_m = m\pi/\epsilon$ and $m \in \mathrm{Z}$. Following the formalism of equation (5.29), we get the Fourier representation of the delta distribution in ϕ, which is

$$\delta(\phi - \phi')) \quad = \quad \sum_{m=1}^{\infty} \frac{\sin(\alpha_m \phi)\sin(\alpha_m \phi')}{N_{mn}^2} \quad \text{with} \quad N_{nm}^2 \quad = \quad \int_0^{\epsilon} \sin^2(\alpha_m \phi) d\phi = \frac{\epsilon}{2} \tag{A.3}$$

This implies two major changes in the Greens functions as presented in (5.23) and (5.36). Firstly, the order of the Bessel functions m has to be replaced by α_m and secondly, the former Fourier representations of the delta distribution in ϕ, as given in (5.15) and (5.28), have to be replaced by (A.3). The resulting Greens functions are given in (A.4) and (A.6).

For the representation by ordinary Bessel functions, which provides a fast converging representation of the electrical field in z direction, we get:

$$G(r,\phi,z;r',\phi',z') = \frac{2}{\epsilon}\sum_{m=1}^{\infty}\sum_{n=1}^{\infty}\sin(\alpha_m\phi)\sin(\alpha_m\phi')\frac{R_{mn}(r)R_{mn}(r')}{\bar{N}_{mn}^2}\frac{\sinh(\beta_{mn}z_<)\sinh(\beta_{mn}(L-z_>))}{\beta_{mn}\sinh(\beta_{mn}L)}. \tag{A.4}$$

The solution of the Bessel differential equation, which fulfills the boundaries on $r = a$ and $r = b$, is then:

$$R_{mn}(r) = Y_{\alpha_m}(\beta_{mn}a)J_{\alpha_m}(\beta_{mn}r) - J_{\alpha_m}(\beta_{mn}a)Y_{\alpha_m}(\beta_{mn}r). \tag{A.5}$$

This implies small changes in the normalization term $\bar{N}_{mn}^2$ as well as in the calculation of the corresponding zeros β_{mn}.

For the representation by modified Bessel functions, which allows a fast converging representation for the electrical field in r direction, we can write:

$$G(r,\phi,z;r',\phi',z') = = \frac{4}{\epsilon L}\sum_{m=1}^{\infty}\sum_{n=1}^{\infty}\sin(\alpha_m\phi)\sin(\alpha_m\phi')\sin(\beta_n z)\sin(\beta_n z')\,\frac{R_{mn\,1}(r_<)R_{mn\,2}(r_>)}{I_{\alpha_m}(\beta_n a)K_{\alpha_m}(\beta_n b) - I_{\alpha_m}(\beta_n b)K_{\alpha_m}(\beta_n a)}, \tag{A.6}$$

implying the corresponding changes of the order, now $\alpha_m = m\pi/\epsilon$, in $R_{mn\,1}(r_<)$ and $R_{mn\,2}(r_>)$, (5.32) and (5.33) respectively.

For the modification of the third representation (5.57), we follow the hint starting from equation (5.19), where we had to solve the one-dimensional time-independent diffusion equation. For the ϕ direction, we now find that

$$g_{mn} = \frac{\sinh(\mu_{nk}\phi_<)\sinh(\mu_{nk}(\epsilon-\phi_>))}{\mu_{nk}\sinh(\mu_{nk}\epsilon)}, \tag{A.7}$$

fulfils the Dirichlet boundary condition in ϕ with $\phi_<$ for $0 \le \phi' < \phi \le \epsilon$ and $\phi_>$ for $0 \le \phi < \phi' \le \epsilon$.

Therefore, the Greens functions represented by modified Bessel functions of imaginary order, which allows a fast converging expression for the electrical field in ϕ direction, is

$$G(r,\phi,z;r',\phi',z') = \frac{2}{L}\sum_{k=1}^{\infty}\sum_{n=1}^{\infty}\frac{\sinh(\mu_{nk}\phi_<)\sinh(\mu_{nk}(\epsilon-\phi_>))}{\mu_{nk}\sinh(\mu_{nk}\epsilon)}\sin(\beta_n z)\sin(\beta_n z')\frac{R_{nk}(r)R_{nk}(r')}{N_{nk}^2}. \tag{A.8}$$

The consistency of the three novel Greens functions for a half-circled coaxial cavity, which fulfill the additional Dirichlet boundary conditions in ϕ, is demonstrated in figure (A.1). Furthermore, figures (A.2) to (A.4) display the non-oscillating behavior of the specially designed representations in their dependence of the different variables when crossing the source point. The salient feature is: as regards precision, a non-oscillating behavior of the function is more favorable than an oscillating one.

Figure A.5 shows the potential in the (r,ϕ)-plane for different positions of the point charge. The electric field components, due to a constant charge distribution within a volume of $(0.2 \le r \le 0.3, 0.5 \le \phi \le 1.0, 0.5 \le z \le 1.0)$, are plotted in figure A.6.

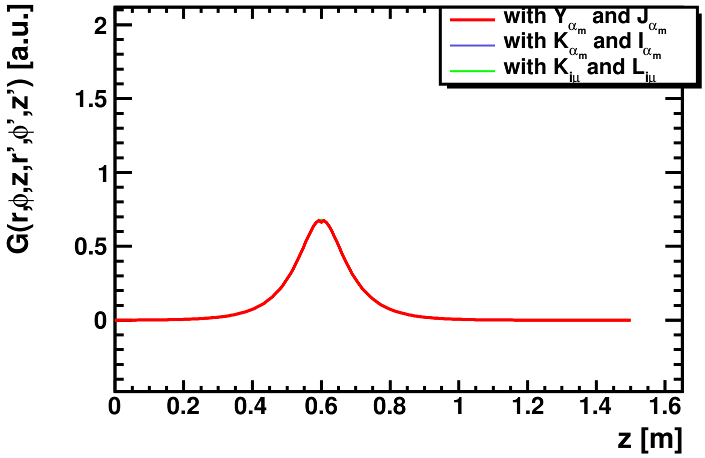

Figure A.1: Representations (A.4), (A.6) and (A.8) as a function of z with $(r', \phi', z') = (0.3, 1.2, 0.6)$ and $(r, \phi) = (0.25, 1)$. The summation limits for m and n were set to 40. All three representations coincide since the domain of the plot is chosen outside the region of slow convergence.

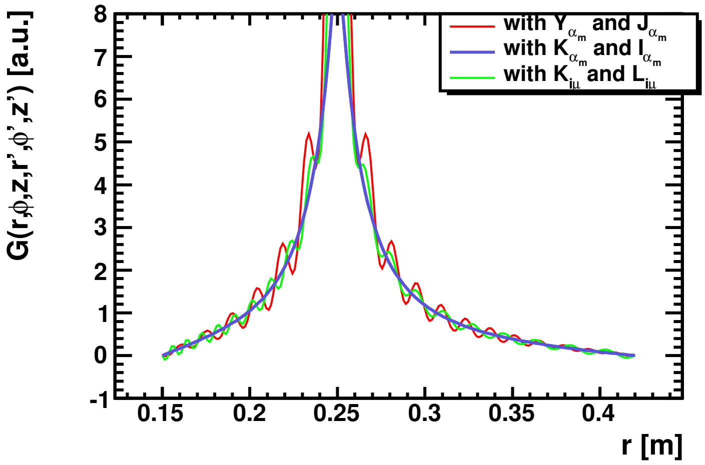

Figure A.2: Representations (A.4), (A.6) and (A.8) as functions of the radius r with $r' = 0.25$ m ($z = z' = 0.5$ m, $\phi = \phi' = 1.0$ rad). The summation limits for m and n were set to 40. Solution (A.6) does not oscillate.

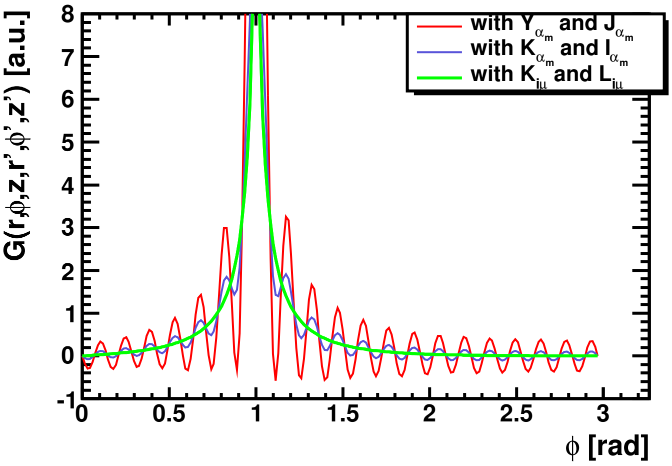

Figure A.3: Solution (A.4), (A.6) and (A.8) as a function of ϕ with ϕ' at 1.0 rad ($r = r' = 0.25$ m, $z = z' = 0.5$ m). The summation limits for m and n were set to 40. Solution (A.8) does not oscillate.

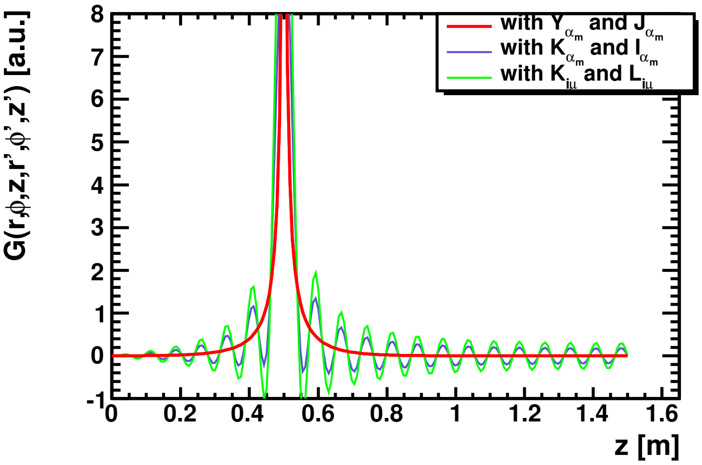

Figure A.4: Solution (A.4), (A.6) and (A.8) as a function of the z axis with z' at 0.5 m ($r = r' = 0.25$ m, $\phi = \phi' = 1.0$ rad). The summation limits for k and n were set to 40. Solution (A.4) does not oscillate.

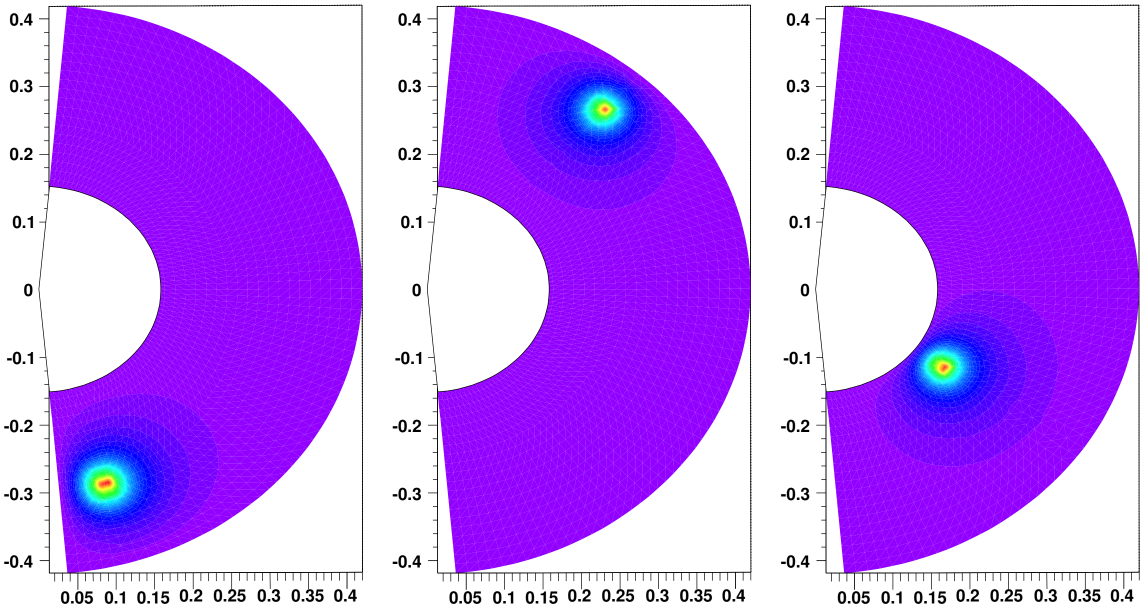

Figure A.5: $(r, \phi)-$contour plots of the Green's function (A.8) at $z = z'$; Summation limits set to 40; $a = 0.15$ m, $b = 0.42$ m, $L = 1.5$ m.

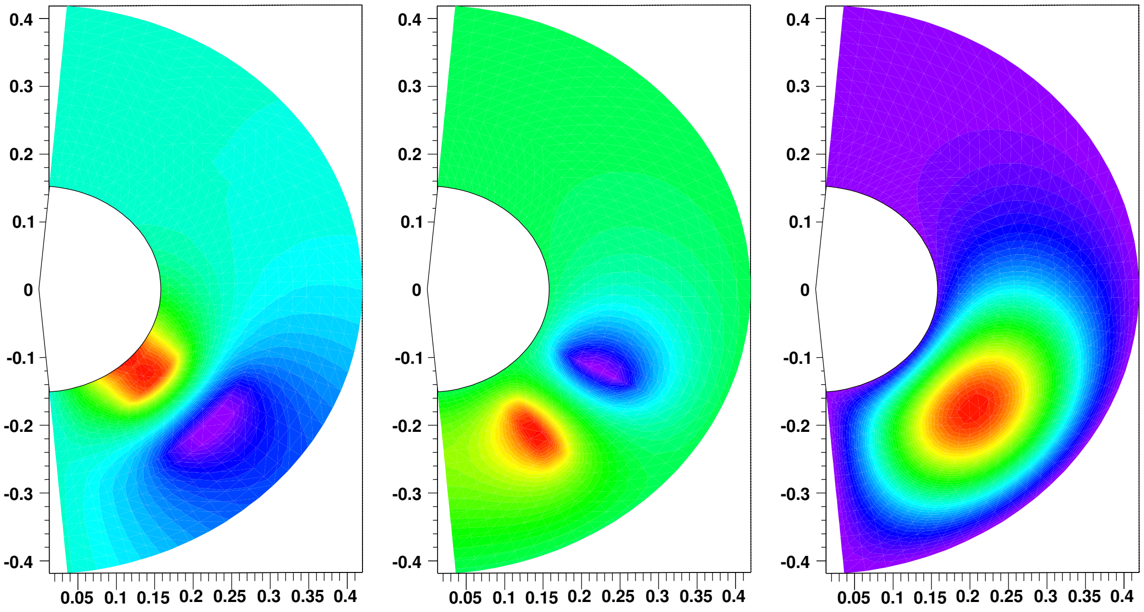

Figure A.6: Electrical fields in (r, ϕ) plane at $z = 0.7$ m for a constant space charge distribution within the region $(0.2 \le r \le 0.3, 0.5 \le \phi \le 1.0, 0.5 \le z \le 1.0)$. *Left:* E field in radial direction (E_r) *Middle:* E field in azimuthal direction (E_ϕ) *Right:* E field in longitudinal direction (E_z). Summation limits set to 40; $a = 0.15$ m, $b = 0.42$ m, $L = 1.5$ m

List of Figures

1.1 Sketch of the QCD phase diagram 3
1.2 Layout of the ALICE detector 5
1.3 Working principle of a drift chamber 7
1.4 Overview of the ALICE Time-Projection Chamber 11
1.5 Laser Calibration system 13
1.6 Charge spectrum from ^{83}Kr decays 14

2.1 Electron transport and ionization in Ne-CO_2-N_2 17
2.2 Transport properties for varying CO_2 fractions 18
2.3 Transport properties varying N2 fractions 19
2.4 Effect of adding O_2 or SF_6. 20
2.5 Effect of adding water to a Ne-CO_2-N_2 mixture. 21
2.6 Sensitivity to temperature variations 22
2.7 Magnetic field within the TPC 23
2.8 Velocity-components of a drifting electron in different gases 24
2.9 Differences of the velocity-component-angles 24
2.10 Simulated distortions due to E×B effects 26
2.11 Field distortions at the FC strips 27
2.12 Electron drift lines in the imperfect Field Cage regions 28
2.13 ANSYS model plots 31
2.14 ANSYS field accuracy 31
2.15 Radial distortion versus drift length due to mispositioned ROCs 33
2.16 Distortion versus radial position due to mispositioned ROCs 33
2.17 Distortion versus radial position due to rotated ROCs 34
2.18 Distortion due to a broken resistor 35

3.1 Wire geometry of the TPC read-out 37
3.2 Tracks, clusters and electron drift 38
3.3 Typical pad-signal including the ion-tail 39
3.4 Variation of pulses within one sector 40
3.5 Measured average signals 40

3.6 Ion tracks and induced signals 41
3.7 Shape dependence on geometrical parameters 43
3.8 Shape dependency on voltage settings 43
3.9 Shape dependency on multiplication avalanche 44
3.10 Block scheme of the ALTRO chip 45
3.11 Fitted O-ROC signal 51
3.12 Tail-Cancellation stages 51
3.13 Basic block diagram for shaping parameter extraction 52
3.14 Superposition of cosmic tracks and cluster positions 53
3.15 Number of collected pulses 53
3.16 TCF parameter τ_1 54
3.17 TCF parameter τ_b 54
3.18 Width reduction versus baseline reconstruction 56
3.19 Mean pulses at high gain and ultra-high gain 57

4.1 Fit residuals of drift velocity parametrization 62
4.2 CFD model - basic overview 63
4.3 Gas velocity within the drift volume 65
4.4 Temperature distribution within the gas volumes 66
4.5 Fit residual plots for heat flux from ITS 67
4.6 Mean temperature due to heat flux from the surroundings 68
4.7 Fit residual plots for heat flux from outer detectors 68
4.8 Fit residual plots for varying gas temperature 69
4.9 Fit residual plots for heat flux from the ROCs 70
4.10 Temperature maps from sensor readings 72
4.11 Pressure variations over one week 73
4.12 Mean drift velocities during the run-period LHC08d 75
4.13 Pressure readings during the run-period LHC08d 75
4.14 Mean temperature during the run-period LHC08d 76
4.15 Relative drift velocity change during the run-period LHC08d 76

5.1 Basic concept of simulating space charge deviations 80
5.2 The radial function $R_n(b)$ versus imaginary order 87
5.3 The radial functions $R_{n,k}(r)$ versus r 88
5.4 The azimuthal part $g_k(\phi, \phi')$ versus ϕ 89
5.5 Solutions as a function of the main axis 92
5.6 Cursed regions of the Green's functions 93
5.7 Potential due to a point charge in the $(r, \phi)-$plane 93
5.8 E field components due to a constant space charge distribution 99
5.9 TPC simulation of a non-central Pb–Pb event 101

5.10 Expected space charge scenario for the ALICE TPC 103
5.11 Space charge scenario with floating gate wires 104
5.12 Space point deviations due to field inhomogeneities 106

A.1 Representations (A.4), (A.6) and (A.8) as a function of z at a position, where the solutions converge fast 113
A.2 Solution (A.4), (A.6) and (A.8) as functions of the r 113
A.3 Solution (A.4), (A.6) and (A.8) as a function of ϕ 114
A.4 Solution (A.4), (A.6) and (A.8) as a function of the z 114
A.5 $(r, \phi)-$contour plots of the Green's function (A.8) 115
A.6 Electrical fields in (r, ϕ) plane due to a constant charge within a arbitrary voxel 115

List of Tables

2.1 Optimized gate, skirt and cover voltage settings 30

4.1 Parameter range of simulated drift velocities 60
4.2 Thermo physical properties of the used gases (from StarCD database). . . 64
4.3 Temperature gradients within the TPC drift volume, when assuming a heat flux from the ITS. 65
4.4 Peak parametrization, when assuming a heat flux from the ITS. 67
4.5 Temperature gradients within the TPC drift volume, when assuming a non-thermalized gas temperature. 69
4.6 Temperature gradients within the TPC drift volume, when assuming heat flux from the read-out chambers. 69

5.1 Parameters as used for the TPC space charge simulations. 101

Bibliography

[1] B. Greene, *ELEGANT UNIVERSE, THE S.S.* (Vintage/Ebury, a division of random house group, 2000).

[2] M. Kaku, *Quantum Field Theory : A Modern Introduction* (Oxford University Press, USA, 1993).

[3] R. Ellis, W. Stirling and B. Webber, *QCD and Collider Physics.* Cambridge monographs on particle physics, nuclear physics and cosmology (Cambridge University Press, 2003).

[4] P. Braun-Munzinger and J. Stachel, *On Charm Production near the Phase Boundary*, arXiv:nucl-th/0012064, 2001.

[5] J. Letessier and J. Rafelski, *Hadrons and quark gluon plasma.* Cambridge monographs on particle physics, nuclear physics, and cosmology (Cambridge University Press, 2002).

[6] The ALICE Collaboration, *ALICE Physics Performance Report, Volume I*, Journal of Physics G: Nuclear and Particle Physics **30**, 1517 (2004).

[7] The ALICE Collaboration, *ALICE Physics Performance Report, Volume II*, Journal of Physics G: Nuclear and Particle Physics **32**, 1295 (2006).

[8] The ATLAS Collaboration, *Expected Performance of the ATLAS Experiment - Detector, Trigger and Physics*, 2008.

[9] The CMS Collaboration, *CMS Physics Technical Design Report, Volume II: Physics Performance*, Journal of Physics G: Nuclear and Particle Physics **34**, 995 (2007).

[10] The LHCb Collaboration, *LHCb Technical Design Report, Reoptimized detector design and performance.*, CERN-LHCC/2003-030, (2003).

[11] ALICE Collaboration, *Technical Proposal for A Large Ion Collider Experiment at the CERN LHC*, CERN/LHCC 95-71, 1995.

[12] The ALICE Collaboration and T. Virgili, *Measuring charged particle multiplicity in ALICE*, Journal of Physics: Conference Series **5**, 105 (2005).

[13] K. Aamodt, *The ALICE experiment at the CERN LHC*, J. Instrum. **3**, S08002. 259 p (2008).

[14] P. Billoir, *Track fitting with multiple scattering: A new method*, Nuclear Instruments and Methods in Physics Research **225**, 352 (1984).

[15] The NA49 collaboration and S. Afanasiev, *The NA49 large acceptance hadron detector*, Nuclear Instruments and Methods in Physics Research Section A: Accelerators, Spectrometers, Detectors and Associated Equipment **430**, 210 (1999).

[16] M. A. et.al, *The STAR time projection chamber: a unique tool for studying high multiplicity events at RHIC*, Nuclear Instruments and Methods in Physics Research Section A: Accelerators, Spectrometers, Detectors and Associated Equipment **499**, 659 (2003), The Relativistic Heavy Ion Collider Project: RHIC and its Detectors.

[17] W. Blum, W. Riegler and L. Rolandi, *Particle Detection with Drift Chambers*, 2nd ed. (Springer, 2008).

[18] J. Wiechula, *Commissioning and Calibration of the ALICE-TPC*, Johann-Wolfang-Goethe Universität, Frankfurt, 2008.

[19] W. T. Coffey, Y. P. Kalmykov and J. T. Waldron, *The Langevin equation: with applications in physics, chemistry and electrical engineering.*World Sci. Ser. Contemp. Chem. Phys. (World Scientific, Singapore, 1996).

[20] The ALICE Collaboration, *TPC Technical Design Report*, CERN-LHCC-2000-001, 2000.

[21] H. R. Schmidt, *The ALICE Time Projection Chamber*, CERN-ALICE-PUB-2002-027, 2002.

[22] V. Danilo, *Private Communication.*

[23] C. Garabatos, *The ALICE TPC*, Nuclear Instruments and Methods in Physics Research A **535**, 197 (2004), Proceedings of the 10th International Vienna Conference on Instrumentation.

[24] G. Renault, B. S. Nielsen and J. Westergaard, *The Laser of the ALICE Time Projection Chamber*, Int. J. Mod. Phys. E **16**, 2413 (2007).

[25] G. Renault, J. J. Gaardhoje, B. S. Nielsen and J. Westergaard, *The Laser Calibration System of the ALICE Time Projection Chamber*, Czechoslov. J. Phys. **55**, 1671 (2005).

[26] S. Biagi, *Magboltz Version 7.07*, 2008.

[27] R. Veenhof, *Choosing a gas mixture for the Alice TPC*, ALICE-INT-2003-29, 2003.

[28] R. Veenhof, *Calculations for the Alice TPC read-out*, http://rjd.home.cern.ch/rjd/Alice/.

[29] J. Wiechula *et al.*, *High-precision measurement of the electron drift velocity in Ne-CO2*, Nuclear Instruments and Methods in Physics Research Section A: Accelerators, Spectrometers, Detectors and Associated Equipment **548**, 582 (2005).

[30] D. Antończyk, *A drift velocity monitor for the ALICE TPC*, GSI Scientific Report 2004, 2005.

[31] R. Shahoyan, *Summary of the L3 magnet field analysis*, ALICE-INT-2007-012, 2007.

[32] R. Shahoyan, *Summary of the ALICE dipole magnet field analysis*, ALICE-INT-2008-019, 2008.

[33] *AliRoot: ALICE Off-line framework for simulation, reconstruction and analysis*, http://aliceinfo.cern.ch/Offline.

[34] M. Mager, *Spatial Calibration of the ALICE TPC Field cage and First Physics*, Technische Universität Darmstadt, 2008.

[35] J. Wiechula *et al.*, *High-precision measurement of the electron drift velocity in Ne-CO2*, Nucl. Instr. Meth. **A548**, 582 (2005).

[36] O. Busch, *Position resolution with prototypes of ALICE Transition Radiation Detector*, Gesellschaft für Schwerionenforschung (Darmstadt), 2002.

[37] D. Vranić, *Drift Distortions in Alice TPC Field Cage*, CERN-ALICE-INT-1997-22, 1997.

[38] ANSYS, Inc., *Version 11*, http://www.ansys.com/, 2008.

[39] R. Veenhof, *Garfield Version 9*, 2009.

[40] M. Ivanov, *Private Communication.*

[41] ALICE TPC Collaboration, *The ALICE TPC, a rapid 3-dimensional tracking device for ultra-high multiplicity events*, (to be published) (2009).

[42] R. E. Bosch, A. Jimenez de Parga, B. Mota and L. Musa, *The ALTRO chip: a 16-channel A/D converter and digital processor for gas detectors*, IEEE Transactions on Nuclear Science **50**, 2460 (2003).

[43] R. Bramm, *Characterization of the ALice Tpc Read Out chip*, Johann-Wolfang-Goethe Universität, Frankfurt, 2005.

[44] J. Baechler *et al.*, *Performance studies with an ALICE TPC prototype*, Nuclear Instruments and Methods in Physics Research A **565**, 551 (2006).

[45] G. Alkhazov, *Statistics of electron avalanches and ultimate resolution of proportional counters*, Nuclear Instruments and Methods **89**, 155 (1970).

[46] J. Fischer, H. Okuno and A. Walenta, *Spatial distribution of the avalanche in proportional counters*, Nuclear Instruments and Methods **151**, 451 (1978).

[47] J. Groh, E. Schenuit and H. Spitzer, *Computer simulation of the electron avalanche in cylindrically symmetric electric fields*, Nuclear Instruments and Methods in Physics Research A **283**, 730 (1989).

[48] B. Mota *et al.*, *Performance of the ALTRO chip on data acquired on an ALICE TPC prototype*, Nuclear Instruments and Methods in Physics Research A **535**, 500 (2004).

[49] S. Rossegger and W. Riegler, *Signal Shapes in a TPC Wire Chamber*, (to be published) (2009).

[50] E. C. Beaty and P. L. Patterson, *Mobilities and Reaction Rates of Neon Ions in Neon*, Phys. Rev. **170**, 116 (1968).

[51] J. A. Hornbeck, *The Drift Velocities of Molecular and Atomic Ions in Helium, Neon, and Argon*, Phys. Rev. **84**, 615 (1951).

[52] E. Basurto, J. de Urquijo, I. Alvarez and C. Cisneros, *Mobility of* $He+$, $Ne+$, $Ar+$, $N2+$, $O2+$, *and* $CO2+$ *in their parent gas*, Phys. Rev. E **61**, 3053 (2000).

[53] B. Mota, *Time-Domain Signal Processing Algorithms and their Implementation in the ALTRO chip for the Alice TPC*, Ecole Polytechnique Federale de Lausanne, 2003.

[54] CERN-EP/ED, *ALICE TPC Readout Chip User Manual.*

[55] R. Boie, A. Hrisoho and P. Rehak, *Signal shaping and tail cancellation for gas proportional detectors at high counting rates*, Nuclear Instruments and Methods in Physics Research **192**, 365 (1982).

[56] *ROOT: An Object-Oriented Data Analysis Framework*, http://root.cern.ch.

[57] M. Pimenta dos Santos, *ALICE TPC Read Out Chambers Cooling System*, CERN-ST/CV-2003-490540, 2003.

[58] U. Frankenfeld, S. Popescu and H. Schmidt, *Experimental Evaluation of the ALICE TPC Front-End Electronics Cooling Strategy*, ALICE-INT-2005-001, 2005.

[59] S. Eicher, A. Romanazzi, S. Rossegger and W. Riegler, *CFD Calculation of the Temperature Gradient of the Drift Gas inside the ALICE Time Projection Chamber*, EDMS No.839971 (in work), 2007.

[60] R. Antonio, *Private Communication.*

[61] E. A. Mason and S. C. Saxena, *Approximate Formula for the Thermal Conductivity of Gas Mixtures*, Physics of Fluids **1**, 361 (1958).

[62] HEXCEL, Inc., *HexWeb, Honeycomb Attributes and Properties*, http://www.hexcel.com/NR/rdonlyres/599A3453-316D-46D6-9AEE-C337D8B547CA/0/HexwebAttributesandProperties.pdf, 2008.

[63] U. Frankenfeld, S. Popescu and H. Schmidt, *Temperature Monitoring System for the ALICE TPC*, ALICE-EN-2005-001, 2005.

[64] M. Krzewicki, *Private Communication.*

[65] G. V. Buren *et al.*, *Correcting for distortions due to ionization in the STAR TPC*, Nuclear Instruments and Methods in Physics Research Section A: Accelerators, Spectrometers, Detectors and Associated Equipment **566**, 22 (2006), TIME 2005 - Proceedings of the 1st Workshop on Tracking in High Multiplicity Environments.

[66] S. Rossegger, *Static Green's functions for a coaxial cavity including an innovative representation.*, CERN-OPEN-2009-003 (2009).

[67] S. Rossegger, *Static Green's functions for a bisected coaxial cavity*, CERN-OPEN-2009-009 (2009).

[68] E. A. Kraut, *Fundamentals of mathematical physics* (McGraw-Hill, New York, NY, 1967).

[69] P. M. Morse and H. Feshbach, *Methods of theoretical physics*International series in pure and applied physics (McGraw-Hill, New York, NY, 1953).

[70] B. Schnizer, *Analytical methods in applied theoretical physics. Lecture notes (in german). Chaps.12 and 13.*, http://itp.tugraz.at/∼schnizer/AnalyticalMethods, 2008.

[71] W. R. Smythe, *Static and dynamic electricity; 2nd ed.* (McGraw-Hill, New York, NY, 1950).

[72] T. Heubrandtner, B. Schnizer, C. Lippmann and W. Riegler, *Static electric fields in an infinite plane condensor with one or three homogeneous layers*, Nucl. Instrum. Methods Phys. Res., A : 489 no.1-3 (2002).

[73] R. V. Th. Heubrandtner, B. Schnizer, *Analytic representations for numeric field computations in the vicinity of a thin wire*, (to be published) (2004).

[74] G. N. Watson, *A treatise on the theory of Bessel functions; 2nd ed.* (Cambridge Univ. Press, Cambridge, 1966).

[75] H. Buchholz, *Elektrische und magnetische Potentialfelder.* (Springer, Berlin, 1957).

[76] F. W. J. Olver, *Asymptotics and special functions.*Computer science and applied mathematics (Academic Press, New York, NY, 1974).

[77] N. T. A. Gil, J. Segura, *Evaluation of the modified Bessel function of the third kind of imaginary orders.*, J. Comput. Phys. **175** ((2002)).

[78] P. Henrici, *Applied and computational complex analysis.*Pure and applied mathematics (Wiley, New York, NY, 1974).

[79] The PANDA Collaboration, *Technical Progress Report for PANDA*, http://www-panda.gsi.de/, 2009.

Curriculum Vitae

Personal Data

Name: Stefan Rossegger
Date of birth: 07.Dec.1980
Place of birth: Hartberg/Stmk
Citizenship: Austria
Address: Wieden 170
A-8225 Pöllau b.H.
E-mail Address: stefan.rossegger@cern.ch

Education / Career

Since March 2007	Doctoral student at CERN - ALICE
Oct. 2001 to Dec. 2006	Study of Technical Physics at Graz, University of Technology Diploma Thesis: “Thermal Studies of the LHCb Vertex Locator using Non-Destructive IR Thermography” Diploma examination: 14th December 2006 (with distinction)
Oct. 2000 - May 2001	Military Service
1995 - 2000	Technical school for Mechanical Engineering (HTL für Maschinenbau-Umwelttechnik) in Weiz, Austria Leaving examination (Matura) with distinction
1991-1995	Elementary school (Hauptschule) in Pöllau, Stmk, Austria
1987-1991	Primary school (Volksschule) in Pöllau, Stmk, Austria

Works and scientific experiences

	Supervision of CERN summer students
Summer 2009	Project title: Variations of the TPC drift velocity
Summer 2008	Project title: Validation of the ALTRO-TCF calibration
Mar 2006 - Jul 2006	Invitation from the LHCb VELO group for thermal research on the VELO modules
Oct. 2005 - Jan. 2006	Teaching Assistant for “Numerical methods in physics” *(Institute of Theoretical and Computational Physics)*
Jul. to Sept. 2005	Summer student at CERN - LHCb Experiment
Feb. 2005 - Jun. 2005	Teaching Assistant for “Mathematics 2E” *(Department of Mathematics C)*
Oct. 2004 - Jan 2005	Teaching Assistant for “Numerical methods in physics” *(Institute of Theoretical and Computational Physics)*

Feb. 2004 - Jun. 2004	Teaching Assistant for “Mathematics 2E” *(Department of Mathematics C)*
Oct. 2003 - Jan. 2004	Teaching Assistant for “Mathematics 1E” *(Department of Mathematics C)*
Feb. 2003 - Jun. 2003	Teaching Assistant at the Department of Mathematics C *(Mathematical Structure Theory)*

RELEVANT PUBLICATIONS

[1] S. Rossegger, N. Neufeld: *The CreditCard PC python module 'ccpc'*, CERN-LHCb-2005-104

[2] S. Eicher, A. Romanazzi, S. Rossegger and W. Riegler: *CFD Calculation of the Temperature Gradient of the Drift Gas inside the ALICE Time Projection Chamber*, EDMS No.839971, 2007.

[3] S. Rossegger: *Static Green's function for a coaxial cavity including an innovative representation*, CERN-OPEN-2009-003

[4] S. Rossegger, B. Schnizer, W. Riegler: *An analytical approach to space charge distortions for time projection chambers*, DOI:10.1016/j.nima.2009.06.056

[5] S, Rossegger: *Static Green's function for a bisected coaxial cavity*, CERN-OPEN-2009-009

[6] S. Rossegger, W. Riegler: *Signal Shapes in a TPC Wire Chamber* (to be published)

[7] ALICE TPC Collaboration: *A rapid 3-dimensional tracking device for ultra-high multiplicity events* (to be published)

GRANTS, PRIZES AND SCHOLARSHIPS

May 2009	*NIM-A Young Scientist Award* for the best contribution on the “11th Pisa Meeting on Advanced Detectors”
2006	*University grant for research work* from TU Graz
2003/04	*University grant for excellent success* from TU Graz

STATUTORY DECLARATION

I declare that I have authored this thesis independently, that I have not used other than the declared sources / resources, and that I have explicitly marked all material which has been quoted either literally or by content from the used sources.

EIDESSTATTLICHE ERKLÄRUNG

Ich erkläre an Eides statt, dass ich die vorliegende Arbeit selbstständig verfasst, andere als die angegebenen Quellen/Hilfsmittel nicht benutzt, und die den benutzten Quellen wörtlich und inhaltlich entnommene Stellen als solche kenntlich gemacht habe.

....
date

....
(signature)

„So eine Arbeit wird eigentlich nie fertig,
man muss sie für fertig erklären, wenn man
nach Zeit und Umständen das Möglichste getan hat.“

Johann Wolfgang von Goethe